2005

Flow and temperature measurements in a linear turbine blade passage with leading edge and endwall contouring and with and without film cooling

Ross James Gustafson
Louisiana State University and Agricultural and Mechanical College, rgusta1@lsu.edu

FLOW AND TEMPERATURE MEASUREMENTS IN A LINEAR TURBINE BLADE PASSAGE WITH LEADING EDGE AND ENDWALL CONTOURING WITH AND WITHOUT FILM COOLING

A Thesis

Submitted to the Graduate Faculty of the
Louisiana State University and
Agricultural and Mechanical College
in partial fulfillment of the
requirements for the degree of
Masters of Science in Mechanical Engineering

in

The Department of Mechanical Engineering

By
Ross James Gustafson
B.S., Louisiana State University, 2002
May 2005

Acknowledgements

I would like to thank Dr. Sumanta Acharya for all the help and motivation. He was always patient and willing to work out problems. Gazi Mahmood's role was one of necessity. He designed almost every aspect of the facility and experiments. His computer programming skills and knowledge of other's work saved valuable time. Also thanks to Arty Ross for help in manufacturing many experimental components. He was very helpful in designing and building the pressure tap manifold and five hole probe. Barry, Jim, and Ed were always willing to help with many aspects in the LSU machine shop. Charlie also helped in several areas and Glen was always willing to let me borrow his camera and pressure transducer. Finally thanks to my parents, Jim and Anna, for supporting me through out my college career.

Table of Contents

List of Tables

List of Figures

Abstract

Gas turbine efficiency can be improved by increasing the turbine inlet temperature. Secondary flows created in the turbine blade passage cause pressure losses and increase the thermal blade loading on the endwall, thus limiting the combustion temperature. Pressure losses, or aerodynamic losses, extract energy from the fluid, leaving less for torque or thrust production. Secondary flows also cause greater non-uniformity in the exit flow from each blade stage, which decreases the stage efficiency. Weakening secondary flows will lower pressure losses and endwall heat transfer. The following research will explore concepts for weakening the secondary flows through the use of (a) leading edge fillets, and (b) non-axisymmetric endwall contouring for both uncooled and film cooled endwalls in a low speed linear turbine blade cascade. Leading edge fillets are surface shape modifications at the blade's leading edge and endwall junction. It is designed to reduce the strength of the horseshoe vortex which is the first element of secondary flows. Non-axisymmetric endwall contouring changes the normally flat endwall between each blade to a three dimensional shape. It is designed to reduce the cross passage pressure gradient that drives the crossflow, another part of the secondary flows. Film cooling injects cooler fluid on the endwall through small holes. Its goal is to keep the endwall cool, but the secondary flow vortex structures interact with these coolant jets and adversely affect their performance. Therefore their strategic locations are important for optimal performance of the coolant jets. In this thesis, the effect of leading edge fillets and endwall contouring on the secondary flow is examined with smoke flow visualization, hot wire anemometry, five-hole pressure probe, surface static pressures, and air temperature measurements. Overall, the non-axisymmetric endwall contour

reduces the mass averaged pressure losses across the blade passage the most, by 53%. Endwall contouring also produces a much more uniform exit flow field. Film cooling slightly increases pressure losses on the contoured endwall, but losses remain below that of the baseline case. The type of leading edge fillets tested had little effect on overall losses and in some cases actually had a negative effect.

Chapter 1. Introduction

Variations of the gas turbine engine have been in development for a long time. Simple steam powered turbines were first used in the 1600's to power machinery. Aegidius Elling of Norway built the first self powered gas turbine engine with a rotary compressor and turbine in 1903. The turbine produced slightly more power than the compressor required. Simultaneously Sir Frank Whittle in England and Hans von Ohian with Max Hahn in Germany developed the first gas turbine engines for jet propulsion in the 1930's. Although these engines have been around for a long time their remains much room for improvement. The best electricity producing gas turbines have a thermodynamic efficiency in the 30% to 40% range. If an additional steam turbine is added to the system efficiencies can improve to the 60% range.

Gas turbines and other types of turbomachinery are used in many different applications ranging from power plants to ship engines to jet engines and even heart assist devices. This wide range of usage makes it very desirable to achieve maximum efficiency. A small increase in efficiency amounts to a large savings in energy the world over. The question arises of how to effectively increase the efficiency of these engines. To do this one must first know how a gas turbine engine works. There are three basic components of a gas turbine. The first is a compressor. It compresses the incoming fluid thereby increasing the total energy of the fluid. The second stage is a combustor. Fuel is added to the compressed fluid and then ignited, further increasing the energy of the fluid. The last stage is the turbine. The high-energy fluid is expanded out, releasing energy back to the engine. As long as the turbine produces more energy than the compressor, the engine works. Some turbomachines consist of only one of these stages like pumps, air

conditioning compressors, and hydropower plants. All are continuous flow devices. The fluid never stops like in a piston engine. Thus there are fewer mechanical losses. The performance of the compressors and turbines are evaluated in much the same way. Both consist of airfoil shaped blades protruding out in a radial pattern. These blades create lift and force the fluid through the system in a compressor. In the turbine, the blades catch the fluid and are forced to move. This whole process takes place three-dimensionally, spinning the fluid around the axis of rotation and moving the fluid through the engine. The problem is that three-dimensional flows are extremely hard to model, measure, and understand. The most common way to test compressor and turbine blades is in a cascade. A cascade is simply a compressor or turbine that is cut in half along the axis and made to lay down flat. The blades are then parallel and the aerodynamics and other properties can be tested more easily. A wind tunnel is used to model the effects of fluid flow over the blades.

The need for improving gas turbine efficiency is well established. More efficient engines will require less fuel leading to less expensive plane tickets and electricity. One area that can be improved in a gas turbine engine is the turbine section. Extremely hot gases enter and expand through the turbine's blades, causing it to rotate. This rotation powers the compressor and in power generation cases an additional generator. For propulsion purposes high pressure gasses exit the turbine at a high velocity, creating thrust. Pressure drops across each blade cause the rotation. Additional pressure losses, aerodynamic losses, are created by secondary flows. These secondary flows, created at the endwall blade junction, extract energy from the gas which would otherwise be used to rotate the blades or produce thrust. If these secondary flows can be weakened, more

energy would be available for torque and thrust production. Additional aerodynamic losses arise because secondary flows create a less uniform exit flow field. A non-uniform exit flow field will be the inlet flow field for successive blade stages. This decreases the efficiency of each downstream stage. Secondary flows also cause heat transfer problems by bringing hot fluid from the center of the channel to the endwall. Due to the thermodynamics of a gas turbine engine, the higher the combustion temperature is, the more efficient the engine. Thus it is desired to increase the combustion temperature as much as possible, but there is a limiting factor. The materials that make up the turbine section cannot be allowed to heat to the point of failure or melting. Secondary flows heat the turbine walls in certain areas, more so than others, thereby limiting the combustion temperature. Again, if the secondary flows can be weakened, higher combustion temperatures can be achieved and efficiency will improve.

Secondary flows are a complex phenomena. They are a series of vortex structures created at the blade endwall junction. The first vortex is called the horseshoe vortex and is created at the blade's leading edge and endwall junction. This horseshoe vortex wraps around the leading edge and two legs are formed. The one that moves towards the pressure side of the blade is called the pressure side leg, and the other that moves toward the suction side is called the suction side leg. The pressure side leg moves quickly towards the adjacent blade's suction surface and meets with that blade's suction side leg. The two form the passage vortex. This passage vortex is strengthened by the flow on the endwall called the crossflow. Crossflow is created by a pressure gradient on the endwall from pressure side to suction side. The passage vortex travels along the blade's suction

surface and through the passage. Secondary flow structures will be explained in more detail later.

The following research will examine two possible methods of weakening secondary flows or reducing their harmful effects. They include leading edge fillets, non-axisymmetric endwall contouring, and film cooling. Leading edge fillets are geometrical modifications at the blade's leading edge and endwall junction. They are usually protrusions from this corner that smoothen the transition from the endwall to the blade leading edge. Leading edge fillets are designed to weaken or stop the formation of the horseshoe vortex. Non-axisymmetric endwall contouring changes the normally flat endwall between each blade to a three dimensional contour. The objective of non-axisymmetric endwall contouring is to reduce the cross passage pressure gradient which drives the crossflow. This is achieved by convex and concave curvature in certain regions. Reducing the crossflow will create a weaker passage vortex. This research will look at both uncooled and film cooled endwalls. Film cooling is the injection of cold fluid through small holes on the endwall. This is done to keep the endwall cool and reduce the harmful heat transfer effects caused by secondary flows. It can also reduce the strength of secondary flows if certain conditions are met.

Several experiments will be performed to determine how each of the methods described above affect the secondary flows. The measurements taken will include smoke flow visualization, hot wire anemometry, five-hole pressure probe, surface static pressures, and air temperature measurements.

The second chapter of this paper will review published literature on secondary flows, leading edge fillets, endwall contouring, and film cooling. The third chapter will

go over all experimental design aspects of the project. This will include the layout of the wind tunnel and cascade. All instrumentation development and processes will be explained. Finally the design and manufacturing process of the leading edge fillets, non-axisymmetric endwall contouring, and film cooling will be examined. Chapter four will present all results. First channel balancing and boundary layer measurements will be shown. Next, fillet results will be compared to that of the baseline. Endwall pressure distributions will be looked at first, then instantaneous flow structures from smoke flow visualization, and finally time averaged flow structures from hot wire anemometry, and five-hole probe measurements. The non-axisymmetric endwall contouring will next be examined. It will be compared to the baseline case in the same manner as with the fillets. Endwall pressure distributions will be looked at first, instantaneous flow structures, and finally time averaged flow structures. The final section of the results will compare the film cooled non-axisymmetric endwall contour to the uncooled non-axisymmetric endwall contour. Only time averaged flow structures will be examined for this case. It was not possible to perform flow visualization on the film cooled endwall. Chapter five will summarize the conclusions of all tested cases and explain which is the most beneficial for today's gas turbine manufacture. Refrences will be next and then the various appendices with instrumentation will be after. Finally a short vita will be given on the author.

Chapter 2. Literature Review

The flow through turbine blades is complicated by the secondary flows caused by the blade / endwall junction. It is important to be able to measure the size, shape, and position of these structures because they influence aerodynamic losses and heat transfer properties. The following sections will first examine what secondary flows are. Next, research others have done on leading edge fillets will be reviewed. Several different types of endwall contouring will then be examined. Finally, many researchers have studied film cooling and some of the more relevant research will be reviewed.

2.1 Secondary Flows

Secondary flows are a major contributor to efficiency losses in modern gas turbine engines. The secondary flow system, in the form of horse-shoe and passage vortices, originates at the stagnation region near the endwall of each blade. These vortical structures travel through the blade passage along the endwall, and grow in size due to the pressure gradients in the passage. Sieverding (1985) has given a comprehensive review of these secondary flow structures. They produce losses in several ways. First these flows extract energy from the main flow and create aerodynamic losses. Secondly, their rotation can bring the hotter gas from the main passage to the endwall, creating high heat transfer regions. These high heat transfer regions limit the maximum combustion temperatures because of material failure properties. When film cooling is incorporated, the secondary flow rotation can also move the coolant away from the endwall and blade where it is needed most. Secondary flows also create a less uniform exit flow. Exit flow angles can vary greatly near the endwall region. The following blade row encounters a more

sporadic flow field than designed for so losses increase for each succeeding row. Secondary flows cause negative effects and in several ways, leaving much room for improvement.

Secondary flows in the blade passage are quite complex, and are composed of several vortical structures. Sieverding (1985) has shown how they form and interact in a cascade. The horseshoe vortex begins at the leading edge within the boundary layer and splits into a pressure side and suction side leg. The pressure-side leg develops into a passage vortex due to the strong endwall pressure gradient.

Gregory-Smith et al. (1992) has made secondary flow measurements by use of hot wire anemometry and a five hole probe. He introduced high upstream turbulence which proved to have little effect on the secondary flows. It mainly decreased the inlet boundary layer thickness which has little effect on net secondary losses. Both measurement methods were able to accurately quantify the secondary flows. A well defined passage vortex was measured and tracked near the endwall and suction surface. A counter vortex from the shed vorticity in the blade wake was also observed downstream of the trailing edge. From the mid chord downstream, the passage vortex moves slightly up and away from the suction surface. The highest turbulence intensity levels remain near the passage vortex. Pressure loss coefficients were calculated and indicate the regions of highest aerodynamic losses.

Wang et al. (1997) performed flow visualization with smoke wires in a turbine cascade. He was able to track the development of the secondary flows through the blade passage. The development of the horseshoe vortex and subsequent change to the passage vortex was observed. His overall interpretation of the vortex flow pattern is shown in

figure 1. The pressure leg of the horseshoe vortex quickly travels to the suction side to form a single passage vortex. The suction side leg of the horseshoe vortex moves above the passage vortex and becomes entrapped in the passage vortex. It rotates away for the suction side wall and eventually exits the passage below the passage vortex. A wall vortex is formed where the pressure leg of the horseshoe vortex meets the suction side. It stays above the passage vortex and increases in size and strength. The remaining small corner vortices were too small for the smoke to pick up.

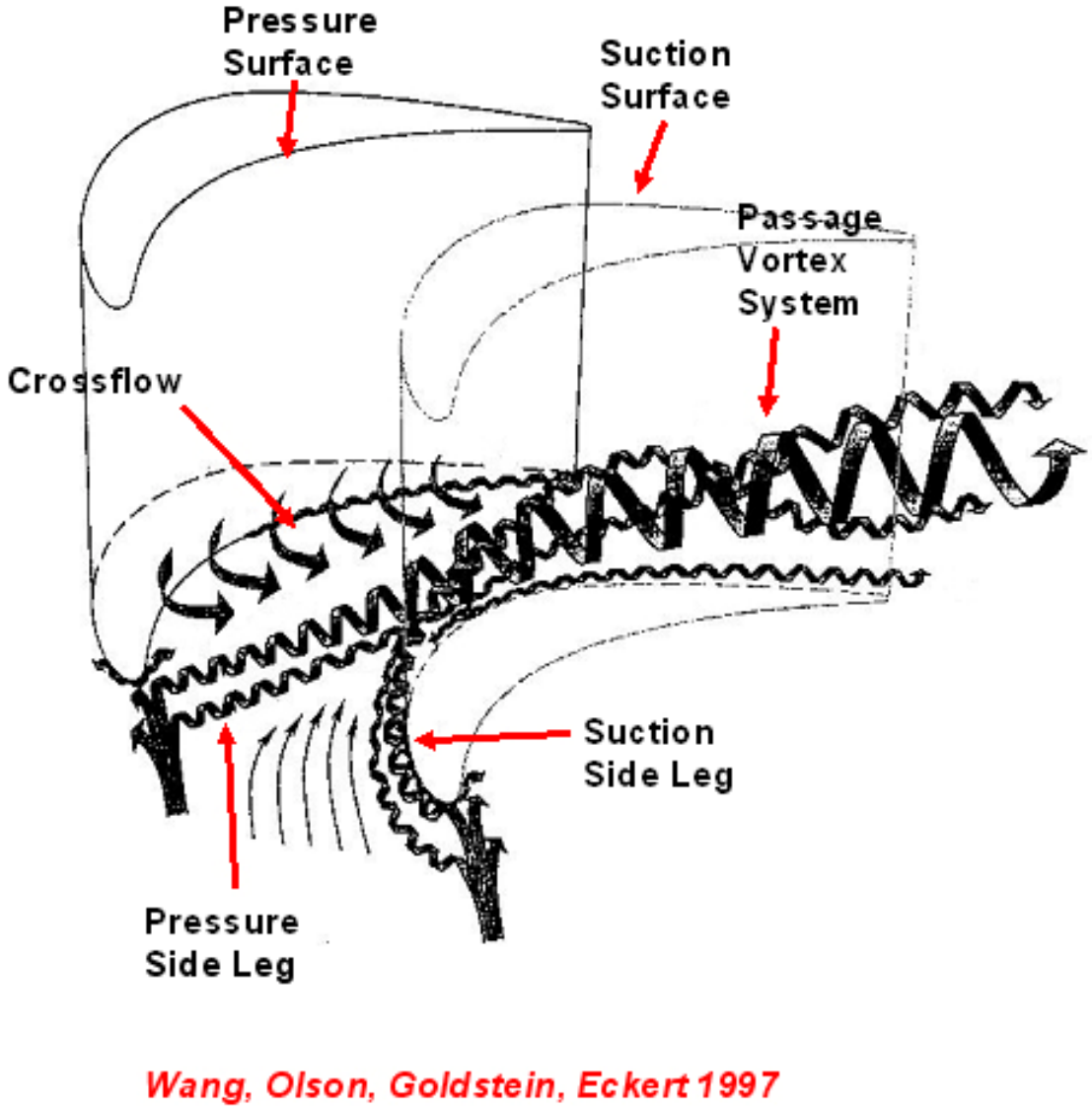

Figure 1: Secondary Flow Structures (Wang et al. 8)

2.2 Leading Edge Fillets

One way to possibly reduce the size, strength, and negative effects of secondary flows is with leading edge fillets. These fillets are characterized by some shaped addition to the endwall / leading edge region of the blade. It is believed that they can reduce the adverse pressure gradient at the leading edge which creates the horseshoe vortex. A smaller horseshoe vortex would hopefully reduce the aerodynamic losses and detrimental heat transfer effects on the endwall. The only question is what would be the size and shape of the fillet to best affect the horseshoe vortex? Several researchers have tried various sizes and shapes to do this and various results have been reported.

Davenport et al. (1990) experimented with a constant radius fillet that went around the entire blade and was tangent to both the blade wall and endwall. He used oil flow visualization, hot-wire anemometry, surface pressure measurements, and laser Doppler velocimetry to determine the effects of the fillet. This fillet did not prevent leading edge separation or the formation of the horseshoe vortex. It did push the horseshoe vortex further away from the blade surface, enlarging the effective radius of the nose of the blade. The size and shape of the vortex was actually increased. Davenport recommended that this type of fillet not be used to eliminate the horseshoe vortex.

Saucer et al. (2000) developed a few different sizes and shapes of leading edge endwall bulbs. The blade thickness was increased around the leading edge / endwall junction to achieve the bulb effect. It was believed this modification would increase the strength of the suction side leg of the horseshoe vortex and, in turn, weaken the passage vortex. Both numerical analysis and experiments were performed. Pitot probes and a five hole probe were used to determine pressure losses and flow angles. A bulb profile

extruding further on the suction side than the pressure side proved to reduce the endwall losses by approximately 50%. The stronger suction side leg of the horseshoe vortex moved the passage vortex further away from the suction side and also deformed it. The numerical simulations also reproduced these effects.

Shih et al. (2002) performed CFD analysis on two different fillets. They were both rounded fillets located at the leadine edge / endwall junction. The first ones thickness faded into the airfoil and the other faded into the endwall. From previous studies it was found that rounded fillets actually increase the size and intensity of the horseshoe vortex. But here, the fillets decreased the stagnation pressure loss across the stage by approximately 40%. The heat transfer was reduced by more than 10% on the airfoil surface and 30% on the endwall. Even though the size and intensity of the horseshoe vortex may have increased, it was believed that lower pressure losses were due to a larger stagnation region. In this region lower flow speeds decrease turbulence production, and thus the pressure losses are lower. The stagnation zone also shifts further downstream on the airfoil surface. Shifting it to a flatter part of the airfoil creates a thicker boundary layer. With different boundary layer development and smaller gradients, the aerodynamic losses would probably decrease. Shih concluded that the size and strength of secondary flows aren't the only factors that influence aerodynamic losses and heat transfer.

Thole (2001) tested several different fillet shapes with CFD analysis and found that one with an asymmetric profile and linear slope with one boundary layer thickness high and two boundary layer thicknesses long was the most effective at eliminating the horseshoe vortex. It also had a pointed leading edge at the stagnation plane. A symmetric

profile was also tested but did not eliminate the suction side leg of the horseshoe vortex. The suction side of the fillet was then enlarged, and the horseshoe vortex was eliminated. Next, measurements were performed on this fillet with a laser Doppler velocimeter. These measurements also showed that the horseshoe vortex was not present. Further downstream, the passage vortex formation was delayed and crossflow remained. No pressure loss measurements were made, but turbulent kinetic energy levels did reduce.

Lethander et al. (2003) performed a CFD optimization to reduce adiabatic wall temperatures in a turbine vane cascade with a fillet. An optimization program changed the size and shape of the fillet and then ran the CFD program. The optimization program tried to minimize the area weighted average of the square of the surface temperature. This was chosen to minimize both the average and maximum surface temperatures. The optimized fillet turned out to be very large. It was over twice as tall as the fillet from Thole (2001) and extended further downstream on both the pressure and suction sides. There was a 1.6% increase in total pressure loss with the fillet, which is very small. The horseshoe vortex never formed and the passage vortex hadn't formed yet in a plane half way through the passage. Crossflow remained strong further downstream. Surface temperatures were significantly reduced, varying from 3% to 10% on the fillet, endwall, and vane surfaces. The maximum temperature was also reduced by 7.5% on the endwall. Without the horseshoe vortex, the hotter fluid never traveled down to the endwall.

2.3 Endwall Contouring

As explained previously, secondary flows contribute largely to aerodynamic losses and areas of increased heat transfer. It is believed if these secondary flows can be decreased in size and strength then their associated losses will also decrease. Another

method that may be able to affect secondary flows is endwall contouring. Here the endwall no longer remains flat but has a changing profile. Secondary flows form in the endwall boundary layer, so contouring the endwall will likely have an effect on these flows. Because of the design of a gas turbine engine the first stage nozzle guide vane is readily available for endwall contouring. The first stage nozzle guide vane also encounters the highest temperatures from the combustor. Questions of where the contouring should begin and end and what profile it should have to reduce the secondary flows the most remains. Also, can contouring be used in stages downstream of the first stage nozzle guide vane? Researchers have explored several different contouring methods but much work remains before the concept is perfected.

Boletis (1985) experimented with endwall contouring in an annular turbine nozzle guide vane test rig. Only the outer endwall was contoured. This is referred to as meridional tip contouring. Previous experiments had been performed with cylindrical endwalls and are used for comparison. Measurements were taken with blade surface pressure taps and a double-head, four-hole pressure probe. The contouring was defined by a cubic function and started just upstream of mid-chord and continued through to the trailing edge, making the inlet area larger than the exit area. The contouring significantly reduced the transverse pressure gradient in the front part of the passage. A low static pressure region is created in the contoured endwall / suction side corner. Low momentum fluid would be less likely to travel from the endwall down the suction surface. Overall pressure losses at the exit plane were reduced significantly when compared to the cylindrical endwall case. The exit flow angle changed little so inlet conditions to a following blade row would also change little.

Hartland et al. (1998) modified a non-axisymmetric endwall profile previously designed by Rose (1994). The purpose of non-axisymmetric endwall contouring is to reduce the endwall pressure non-uniformities downstream of the trailing edge. This would reduce coolant leakage. Also, the driving force for the secondary flow field can be modified. To make the contour an axial and tangential profile are multiplied to give the endwall height. The axial profile is higher toward the trailing edge, and the tangential profile is sinusoidal. CFD was used to predict and change the profiles until pressure non-uniformity was achieved. One hundred endwall pressure taps were used to measure the endwall pressure distribution. Velocities and pressures were measured with a 5-holed cobra type probe downstream of the trailing edge. The contour was successful in reducing pressure non-uniformity at the trailing edge. Both the passage vortex and loss core moved about 10 mm closer to the endwall. This is because the passage vortex forms at the same height above the trough as for the flat endwall case but does not rise up with the rising endwall. Pressure losses are slightly higher for the contoured endwall but the secondary flow structures change little. Even though the cross passage pressure gradient at the trailing edge is reduced, the secondary flow strength has increased slightly. Endwall curvature is directly linked to the endwall pressure gradient. It was suggested that by adding endwall curvature further upstream the driving force of secondary flows could be modified.

Dossena et al. (1999) performed simulations and experiments with a two-dimensional contoured endwall on a turbine vane linear cascade. First, a flat endwall was tested as a basis of comparison. The contouring starts at the leading edge while the span decreases smoothly and ends at the trailing edge. The exit area at the trailing edge is the

same for both the flat endwall and the contoured endwall. The span wise contraction ratio, h2/h1, was 0.70. Measurements were made downstream of the trailing edge with a miniaturized five-hole pressure probe. CFD was used to determine flow structure within the passage. Stronger acceleration within the contoured endwall inhibits vortex generation and development. Secondary effects were confined in the endwall region for both the contoured endwall side and flat endwall side. Secondary effects near the flat endwall side showed lower vortex intensity but were similar to the planar cascade. Outlet angles varied linearly along the span. Secondary losses and profile losses were reduced. This is believed to be caused by the lower velocities in the passage.

Yan et al. (1999) optimized a non-axisymmetric endwall profile using CFD in order to reduce the secondary flows. High pressure steam turbine nozzle guide vanes were used in a linear cascade. It was thought that having convex curvature near the pressure side would reduce the high static pressure levels and a concave curvature near the suction side would increase the low static pressure levels. The cross passage pressure gradient, which drives secondary flows, would then be reduced. Profiling began 15% upstream of the leading edge and ended at the trailing edge. The contour was made by combining an axial curve and a pitchwise curve. The axial curve was defined by its maximum height and location of the peak. The pitchwise curve is two sine waves with a trough near the suction side and a peak near the pressure side. Endwall pressure measurements were made with several pressure taps on a flat endwall and the contoured endwall. A turbulence grid was placed upstream of the cascade to create approximately a 5% turbulence intensity level. Two cobra type 5-hole probes were used to make measurements within the passage. It the first part of the passage the flow appears to be

very much like the flat endwall case because the contouring has had little effect. Near the middle of the passage the secondary flow seems to be stronger but is probably due to a blockage effect. Near the trailing edge a reduced cross passage pressure gradient causes signifigantly reduced secondary velocities, and the loss core formation is inhibited. Yaw angles show less overturning near the endwall, and the pressure curves also show less convection of losses near the trailing edge. Downstream of the trailing edge the vortex center has moved much closer to the endwall. The wake is less distorted and the losses are reduced near the endwall. Over and under turning of the exit flow angle have been reduced, improving the inlet conditions for the following blade row. Secondary kinetic energy and secondary losses were reduced by 20%. CFD predicted a larger reduction in secondary losses of 40% but very closely predicted the reduction in secondary kinetic energy. Overall, the non-axisymmetric endwall was successful in reducing the secondary flows.

Harvey et al. (2000) designed and optimized a nonaxisymmetric endwall for a turbine rotor blade in a linear cascade. The first part of the study used a linear design system to optimize the endwall curvature. The basic idea was to use convex curvature to accelerate the flow, reducing the static pressure, and concave curvature to cause diffusion which raises the static pressure. Their goal was to control the surface static pressure distribution and reduce the exit whirl angle distribution. The maximum radial amplitude was set to 25% of the axial chord. For the first study they tried to reduce the cross passage pressure gradient. This resulted in increasing exit angle overturning so a second profile was simulated. Here, the goal was to reduce the extra overturning. Overturning was reduced while improved underturning was retained. Crossflow was enhanced near

the trailing edge which opposed the overturned boundary layer. A corner vortex was created in the acute corner on the suction surface side. This corner vortex rotates the opposite direction of the passage vortex and opposes overturning. There is a reduction in losses in the passage vortex region and near the endwall. Secondary kinetic energy was reduced by 40%, which may further reduce losses. Streaklines showed the passage vortex to be reduced in size but also showed the counterrotating corner vortex. Overall losses were predicted to be small but exit angle deviations and secondary kinetic energy were reduced significantly.

Hartland et al. (2000) performed the experimental part of the nonaxisymmetric endwall study which Harvey et al. (2000) designed and optimized. Experiments were carried out on a planar cascade with a planar endwall and a profiled endwall. Again the goal was to reduce the passage vortex strength and create a more uniform exit flow angle. Endwall pressure taps were used to measure the endwall pressure distribution, and a five-holed cobra type probe was used to measure total pressure and velocities. Flow visualization was also performed with diesel oil and fluorescent dye. The profiled endwall's highest peak was at 20mm to 25mm and the lowest dip was at -10mm to -15mm. Pressures were raised significantly near the suction surface and lowered slightly near the pressure surface. Near the throat area the profiled endwall produced a weaker passage vortex which was centered approximately midpitch. The cross passage pressure gradient was reduced so overturning was significantly less. Secondary kinetic energy was reduced by 10%. A smaller high loss region was observed near the suction surface. Just upstream of the leading edge shows a significantly weaker vortex divided into to parts. The smaller more intense part is nearer the suction surface and further away from the

endwall. The larger weaker part is near the pressure surface and close to the endwall. CFD predicted a strong counter rotating vortex developing from the re-entrant corner at the suction surface, but the five hole probe was too large to capture it. Overall losses are slightly reduced. Downstream of the trailing edge the passage vortex is less intense but the crossflow seems stronger. A hump coming from the suction side produces a strong countervortex close to the endwall. The double peak loss core is not observed with the profiled endwall. Underturning is reduced by about 2 degrees and overturning is slightly less. Secondary kinetic energy showed a large reduction. The pitch averaged loss peak is also reduced and moved closer to the endwall. Overall total losses were reduced by 20 percent and secondary losses by 30 percent. The strong countervortex created extra losses so the hump at the exit near the suction surface may not be desirable.

Oke et al. (2000) performed a CFD study on a two-dimensional endwall contour with film cooling. Contouring was placed in two different positions. The first configuration, C1, placed the contouring upstream of the nozzle guide vane and the second, C2, continued through the vane passage. The opposite endwall was flat. Slot film cooling was placed upstream of the airfoils on both endwalls. The injection angle of the slot was 35 degrees relative to a tangent plane to the endwall. A density ratio of 2 was used and each film cooling slot had a mass flow rate of 1.5% of the nozzle inlet. The flat endwalls and C1 endwall experienced flow reversal at the leading edge while the C2 configuration did not. Cross flow was also reduced for the C2 configuration because of the decreased pressure difference between the suction and pressure surfaces. When film cooling was incorporated flow reversal was again observer in all cases. Film cooling effectiveness was the greatest for the C2 endwall. Only a small strip near the pressure

surface and the wake region after the trailing edge was not protected. Overall the C2 contour had less aerodynamic losses. The secondary flows are believed to be reduced by the pressure gradient induced the area contracting of the contouring.

2.3 Film Cooling

Gas turbine engines become more efficient at higher combustion temperatures. Thus, it is desired to increase the gas temperature as much as possible. But, there is a limiting factor that determines the maximum temperature. The temperature cannot go beyond the failure temperature of the materials that make up the turbine. Some cooling mechanism must be employed if higher combustor temperatures are desired. One method used to keep the turbine parts cool is film cooling. In film cooling, coolant is injected at the blade walls and endwall and hopefully stays in between the hot gas and the wall. The turbine parts stay cooler and their life is extended. This does not always happen so perfectly. Sometimes the coolant leaves the surface, and the wall comes in contact with the hot gas. Also, this coolant comes from the compressor. The more coolant used, the less efficient the gas turbine becomes. Thus it is desired to minimize the amount of coolant used and maximize its effectiveness. A large amount of research has been performed on film cooling, with many different methods and arrangements.

Bario et al. (1990) investigated how single jets and rows of jets perform in various locations of a turbine cascade. One jet was located in the center of the channel at the leading edge. The next two were located about half way through the passage, one closer to the suction side and the other closer to the pressure side. The single jets were mounted in cylinders so they could be rotated to achieve different yaw angles but were fixed to inject at 60 degrees away from the endwall. Two rows of holes were placed just

downstream of the leading edge. These 55 holes were fixed and injected at 30 degrees away from the endwall. Measurements were made with a five-hole probe, a hot wire anemometer, and a laser smoke visualization technique. For the single jets with a high velocity ratio, the jet lifted away from the endwall. The jet remained close to the endwall with a velocity ratio less than one. Changing the yaw angles of the single jets did little to affect the jet trajectories. The section thickness of a single jet is twice as large as the same jet in a multiple hole configuration. Their lateral diffusion is decreased because the neighboring jets prevent the external flow from reaching the endwall. Secondary flows make the multiple jet layer thickness more pronounced on the suction side of the passage. Barrio also concluded that the multiple row of holes may have counteracted the secondary flow.

Harasgama (1992) experimented with turbine nozzle guide vanes in an annular cascade. Actual engine conditions were met with realistic Reynolds numbers, Mash numbers, gas-to-wall temperature ratios, and gas-to-coolant density ratios. 19 coolant holes were placed along one iso-mach line. The holes were aimed 30 degrees away from the endwall and perpendicular to the iso-mach line, creating a uniform blowing rate and momentum flux ratio across the passage. Measurements were made with 68 thin film heat transfer gages and pressure taps on the endwall. This proved to be very effective in cooling the endwall. Nusselt numbers were reduced by 75% near the coolant injection area and by 50% in most other areas. The secondary flows did convect the coolant toward the suction side. Thus, the pressure side trailing edge received less coolant and Nusselt numbers were reduced by only 20%.

Jabbari et al. (1996) tested a film cool pattern on a turbine blade cascade. Fourteen film cooling holes were placed on several different lines throughout the passage. They were aimed 25 degrees away from the endwall and most were alined with the inline passage direction. Those nearer to the suction surface were pointed in the transverse direction, away from the suction side. Sixty taps were drilled in the endwall for flow sampling and pressure readings. A mass transfer technique was used to measure film effectiveness by injecting a foreign gas tracer into the mainstream flow. Visualization of the jets on the endwall was performed with an ammonia gas and diazo paper. The sixty taps proved to be insufficient for measuring the film cooling effectiveness. Higher blowing rates and higher density ratios made the coolant penetrate less into the mainstream flow, which led to higher effectiveness values. Reynolds numbers has little effect on the endwall mass transfer distribution. The large hole spacing, variation in the velocity field, and displacement of the jet trajectory created a wide variation in film cooling effectiveness.

Friedrichs et al. (1996) measured film cooling effectiveness on a low speed turbine cascade. Measurements were made with an ammonia and diazo technique. This is usually used for surface flow visualization, but Friedrichs developed a new method of calibration which related it to the film cooling effectiveness. The film cooling arrangement consisted of 43 holes in four tangential rows and four individual holes. All holes were ejected at 30 degrees away from the endwall. The first row of holes ejected in the inlet flow direction and was just upstream of the leading edge. The next two rows were in the middle of the passage and ejected in the approximate inviscid streamline direction. The fourth row was near the trailing edge and ejected at an angle to the inviscid

streamline direction, more toward the pressure surface. The four individual holes were placed in the endwall / pressure surface trailing edge corner. Three dimensional separation lines created by the secondary flows were identified. Coolant ejected underneath these separation lines proved ineffective, because it was lifted away from the surface. Coolant ejected away from these lines covered a larger area. Near the pressure surface the crossflow increased the lateral spreading of the coolant. Film cooling caused the separation lines to move slightly downstream, and the crossflow was turned closer to the inviscid streamlines. The fourth row especially, ejecting more toward the pressure surface, was found to reduce the crossflow. Complete coolant coverage was not achieved because of the secondary flows.

Friedrichs et al. (1997) also performed aerodynamic loss measurements on the same film cooling configuration as in 1996. A five hole probe was used to take measurements downstream of the trailing edge. Losses were broken up into three different groups. The losses generated within the hole, losses resulting from coolant mixing with the mainstream, and changes in the secondary flow losses were calculated. They were defined by different stagnation pressures. It was found that overall, film cooling increases losses. When the streamwise velocity components of the coolant are similar to the free stream velocity, an optimum coolant supply pressure is reached. The greatest losses come from those generated within the coolant holes. If these are excluded, the overall losses are small and can be negative depending on inlet blowing ratio. Losses per unit massflow are increased when coolant is ejected into regions of low static pressure. The secondary losses can be reduced by ejecting coolant upstream of the

separation lines. The spanwise location of the secondary loss core is brought closer to the endwall, resulting in a more uniform flow for the next blade row.

Friedrichs et al. (1999) improved his endwall film cooling configuration to obtain a more uniform effectiveness. In the same facility as Friedrichs (1996, 1997), it was desired to improve the film cooling effectiveness without increasing coolant consumption or aerodynamic penalties in the region downstream of the three dimensional separation lines. To determine the best coolant hole locations, the surface flow field without film cooling predicted by CFD was used. The CFD prediction proved to be very similar to the oil and dye surface flow visualization. Coolant trajectory estimates were made by superimposing the proposed coolant hole locations on the endwall surface flow field without film cooling. Hand drawing an estimated coolant trajectory helped to optimize the coolant hole locations. The area downstream of the separation lines was broken into three separate regions. The first was in between the separation line and the leading edge region. The second region was between the pressure surface and an imaginary line half way between the pressure surface and the separation line. This area is characterized mostly by inviscid streamline flow. The third region is in between the imaginary line and the separation line. Strong crossflow exists here. The first and second regions used classical cooling configurations. The third region was cooled by one row of holes on the imaginary line. Here, the secondary flow would sweep the coolant towards the suction side. Improved coolant coverage was achieved when comparing the new configuration to the holes located downstream of the separation line in the old configuration. Also, the aerodynamic losses were reduced. The pressure loss contours changed little when compared to the uncooled configuration, showing that ejecting coolant downstream of the

three dimensional separation lines does not affect the secondary flow structures. Reduction in aerodynamic lose was achieved by ejecting coolant in high static pressure regions. Endwall film cooling configurations can be improved by considering the secondary flow structures.

Burd et al. (2000) experimented with slot bleed injection upstream of a nozzle guide vane cascade. This slot is used to simulate combustor bleed cooling. It was inclined at 45 degrees away from the endwall and injected just upstream of the leading edge on a two dimensional contoured endwall. The slots covered most of the upstream span. Triple sensor hot wire anemometry was used to measure three dimensional velocity and turbulence components. Pressure losses were measured with a pitot-static probe and wall pressure taps. The secondary flow structures on the contoured endwall were more concentrated in size but stronger while the flat endwall produced larger but weaker structures. Low bleed flow rates had little effect on the secondary flow structures. Greater bleed flow rates suppressed the secondary flows and moved them closer to the suction surface/contoured endwall corner. The total pressure loss at the exit of the passage proved to be fairly independent of the bleed flow rate.

Oke et al. (2000) using the same facility as in Burd and Simon (2000) tested discrete hole injection instead of slot injection. Two rows of staggered holes were placed just upstream of the leading edge in the contoured endwall. The holes were again oriented at 45 degrees away from the endwall surface. The bleed flow was heated for temperature field measurements. Hot wire anemometry and a temperature probe were used to observe the flow field. Coolant was carried to the suction side by the crossflow when low coolant blow rates were tested. There was no suction side coolant migration when higher blow

rates were used because the coolant had sufficient momentum. Discrete holes produced greater mixing than the slot injection which resulted in about a 20-30% drop in performance. Temperature contours changed little for varying bleed flow rates except near the pressure surface. There, higher bleed flow rates produced greater temperatures. Overall, for this configuration the best bleed flow rate was about 3.0% of the main passage flow.

Oke et al. (2001) next tried two upstream slots located near where the two rows of discrete holes previously were. Again, the slots were angled at 45 degrees away from the endwall. Tests were performed with both slots ejecting coolant or with one covered and the other ejecting. Three component hot wire anemometry was used near the exit plane for velocity and turbulence measurements. A thermocouple probe was used for temperature distributions. Due to the endwall contour, the secondary flows were relatively week when compared to the flat endwall. Coolant ejection had little influence on the secondary flows. Cross-flow made the coolant migrate towards the suction side when lower momentum flux ratios were tested. Higher momentum flux ratios caused more coolant to accumulate near the pressure side. Using a single slot for cooling produced more uniform coolant coverage because higher momentum flux ratios were produced. Temperature distributions for both cases were very similar.

Oke et al. (2002) partially covered the two upstream slots from 2001 in four different configurations. This was done to re-distribute mass and momentum injection rates. The first configuration left only the pressure side half of the upstream slot open. The pressure side cooling was significant but a vortex was formed on one edge of the slot. This vortex later impacts the pressure side, reducing the temperatures there.

Increased mass flux ratios strengthen the edge-generated vortex, while lower mass flux ratios convect more coolant to the suction surface. The second configuration not only left the pressure side half of the upstream slot open, but also the downstream slot was left completely open. This configuration would hopefully provide more uniform coolant coverage across the pitch. More coolant convects toward the suction side at low mass flux ratios while at high mass flux ratios; more coolant is present on the pressure side. An average mass flux ratio provides the most uniform coverage for this configuration. The third configuration uses only the upstream slot but allows more coolant to be injected directly in front of the leading and less on either side. This configuration was supposed to provide more coolant to the leading edge region. The coolant rises above the leading edge vortex and continues cooling the pressure side far downstream. A weaker edge-generated vortex forms and helps lift the coolant further up the pressure surface. More mixing occurs with the main flow and causes greater losses. The fourth configuration is the same as the first but allows some coolant to be injected on the suction side. Hopefully more coolant would stay near the pressure side. The pressure side is cooled better than the single and double slot injection cases but the suction side cooling is lower. Overall, lower mass flux ratios produce more uniform cooling.

Pasinato et al. (2002) performed film cooling experiments on a turbine vane cascade. Three discrete angled slots injected coolant upstream of the leading edge at an angle of 25 degrees to the main flow. The endwall is axially profiled and the injection slots are located in a wall perpendicular to the flat endwall just upstream of the profile. Flow measurements were made with a pitot probe, a Kiel probe, and a single hot wire probe. Heat transfer measurements were made with the transient thermochromic liquid

crystal technique. An effective thermal shield was created by the film cooling but a vortical structure still formed upstream of the coolant injection. Pressure loss coefficients near the exit proved to change little with film cooling and changes in blowing ratio. Higher Stanton numbers were observed near the injection location but film cooling effectiveness levels were also higher in these locations. Cooling effectiveness was also measured to be significant on the endwall near the pressure surface and in the downstream half of the passage away from the vane surfaces.

Knost et al. (2004) experimented with two different endwall film cooling patterns in a turbine vane cascade. Both configurations had an upstream slot which injected coolant at 45 degrees with respect to the endwall. All film cooling holes injected at an angle of 30 degrees. The second pattern had fewer holes than the first because provisions for a gutter, the joint between two matching platforms, were made. The first pattern placed holes along iso-velocity contours. This would ensure uniform blowing rates and momentum flux ratios across one line, which would help prevent jet lift off. The second pattern placed holes along axial lines near the same areas where the holes for the iso-velocity pattern were placed. Fourteen more cooling holes were used in the first pattern than the second because of the provision for the gutter in the second pattern. Endwall temperature measurements were made with an infrared camera and several thermocouples. CFD simulations were used to predict streamlines near the endwall. Coolant flow paths could be estimated with these streamlines. When both slot and hole film cooling were used a large region in the center of the beginning of the passage was over cooled. Some of this coolant could be used elsewhere. Streamlines near the endwall and at midspan were considerably different and should be taken into account when

designing a film cooling pattern. The iso-velocity contour hole pattern proved to be more effective in achieving uniform film cooling effectiveness. Higher momentum flux ratios allowed coolant to penetrate further into the leading edge and downstream pressure side regions. In the upstream pressure side region, the higher momentum flux ratios tended to make the jets separate from the endwall. This was opposite for the downstream pressure side where the jets were less likely to separate.

Chapter 3. Experimental Design

Measurements are difficult to make in actual gas turbine engines. Thus, models must be made in order to determine the flow characteristics inside the engines. Implementations for various measurements must be allowed for without compromising the model. Producing a model with the same operating conditions as a real gas turbine engine is very difficult. Available facilities, budget, and time constraints will determine how closely operating conditions will be met. The objective of this study is to reduce the negative effects of secondary flows by the use of leading edge fillets, endwall contouring and film cooling. This chapter will discuss the design of the experimental facility.

3.1 Wind Tunnel and Linear Cascade

For these studies the GE-E^3 (Timko) turbine blade of known characteristics was scaled up 10 times. This high pressure blade is taken from the hub side section of the annular E^3 engine. Its parameters are given in table 1.

Table 1 Cascade test section parameters:

Actual chord length, *C* (cm)	35.86
Axial chord length, C_{ax} (cm)	30.36
Aspect ratio (true chord length to blade span), *C/S*	0.78
Solidity ratio (true chord length to blade pitch), *C/P*	1.23
Stagnation temperature, $T_{o,in}$ (K)	302
Stagnation pressure, $P_{o,in}$ (Pa)	1.013×10^3
Flow inlet angle (degrees)	0
Average streamwise velocity upstream, U_{ref} (m/s)	10.26
Inlet Reynolds number, Re_{in}	233,000
Upstream streamwise turbulence intensity	4.0%

A span of 18 inches, 457.2 mm, was selected to ensure the secondary flows created from the top and bottom walls did not interfere with each other. At mid-span there exists a region of two-dimensional flow. Three blades were manufactured out of wood with spanwise groves for pressure tap tubes. Tape was used to cover the grooves, then the blades were coated with polyurethane to create a smooth surface.

A drawing of the wind tunnel and cascade is shown in figure 2.

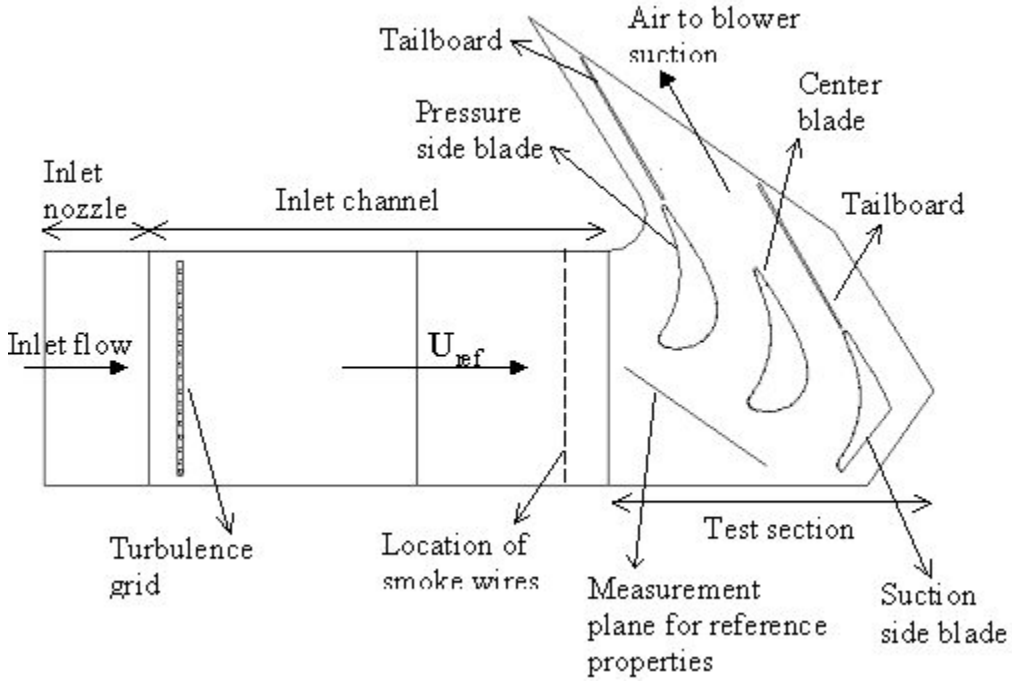

Figure 2: Schematic of the experimental test facility

The entire facility is contained in an indoor lab, which maintains ambient air conditions. This is a suction type facility powered by a New York Blower Company 5 horsepower, 3.73 kW, axial duct fan. A variable frequency inverter made by Omron controls the fan speed. At the inlet of the wind tunnel is a fine screen followed a 4-inch thick layer of honeycomb and finally another fine screen. The flow is then accelerated through a two-dimensional nozzle with a contraction ratio of 3.4:1. The main channel has an aspect ratio

of 1.36:1 with the height the same as the blade span. The remainder of the tunnel and test section is made of 0.5-inch thick clear acrylic. Four boundary layer bleeds next reduce the boundary layer thickness. These bleeds are simply angled slots with small plenums attached to the outside of the walls. An auxiliary inlet at the main blower inlet provides suction, and globe valves control the amount of bleed flow. A passive turbulence grid made of 0.48 inch, 12.2 mm, diameter wood rods spaced 2.25 inches in both the horizontal and vertical directions provides freestream turbulence to cascade. This grid is located 4.2 times the axial chord, 4.2 Cax, upstream of the center blade. A changeable top wall upstream of the test section, 2.2Cax to 2.7Cax, has slots for boundary layer measurements.

The test section is made of three blades, giving two channels. The two side walls outside of the outer blades have additional bleed slots to help control the stagnation point at the leading edge. Part of one of the outer blades is cut off to minimize blockage in that outer passage. The bottom endwall has small holes for thermocouples. The top endwall has eight quarter inch tangential slots, which allow for probe traverses. These slots are covered with tape when not in use to prevent flow leakage. When a slot is being traversed, two pieces of tape would be folded over the slot to minimize flow leakage. Slot locations can be seen in figure 3. Two tailboards pivoted at the trailing edge of both outer blades are used to ensure equal mass flow rates in both channels. The tailboard angles can be adjusted from outside the tunnel with a locking screw adjustment mechanism.

The coordinate system used for all measurements is defined in figure 4. The global coordinate system, (X_G, Z_G), originates at the most upstream position on the center blade. Parallel to the global coordinates are the local coordinates, (X, Y, Z), which

originate on the pressure side of the center blade. Local velocity components, (U, V, W), are parallel to the local coordinates.

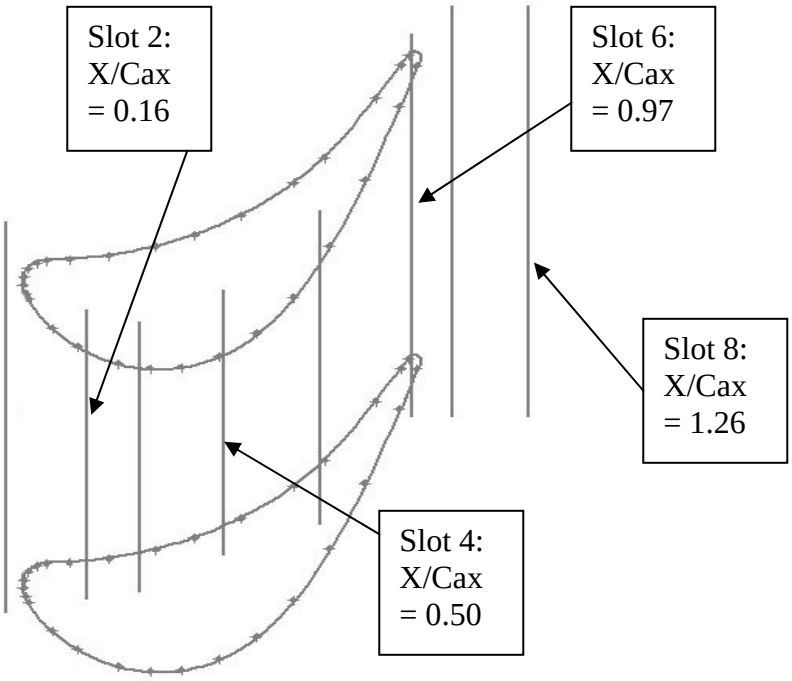

Figure 3: Traverse Slot Positions

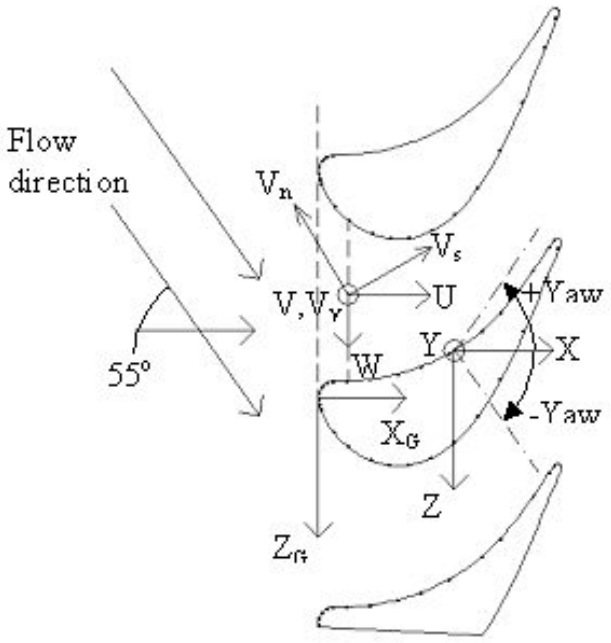

Figure 4: Coordinate Systems

3.2 Instrumentation

Several different pressure, velocity, and temperature measurements were required to determine how the secondary flows were affected by the leading edge fillets, endwall contouring, and film cooling. Various pressure taps, probes, traverses, data acquisition systems, power supplies, and computer programs were used to make measurements. This chapter will discuss the setup and implementation of each type of instrumentation system used in this facility. Every time measurements were made the various conditions were recorded in a logbook for later reference.

3.2.1 Blade Pressure Taps

The first measurements made were with pressure taps on the blade surface. As mentioned before each blade was manufactured with span wise groves around the parameter, which would accommodate 1.65 mm diameter stainless steel tubing. 29 groves around the center blade, 15 on the pressure side of one outside blade, and 19 on suction side of the other outside blade were cut in the same positions on each blade. The tubes are 20 inches long and a pressure tap hole 0.30 mm diameter was drilled in the side at a location of 6 inches from one end. Thus, our pressure measurements were made at 33.3% of the span. Thin wires were used to ensure the pressure tap holes were not blocked. The pressure tap holes were oriented to point perpendicularly away from the surface. The end 6 inches away from the pressure tap is sealed off and rests on the endwall. The other open end of the tube protrudes through holes in the top endwall. A rubber tube is fitted snugly over the open end of the stainless steel tube and then connects, with every other pressure tap tube, to a rotating pressure manifold. This rotating and sealing pressure tap manifold could accommodate 72 pressure taps, and was made because only one pressure

transducer was available. Figure 5 shows the manifold. It greatly sped up data acquisition time for the 63 pressure taps. One rubber tube went from the pressure manifold to the Validyne DP45-18 differential pressure transducer.

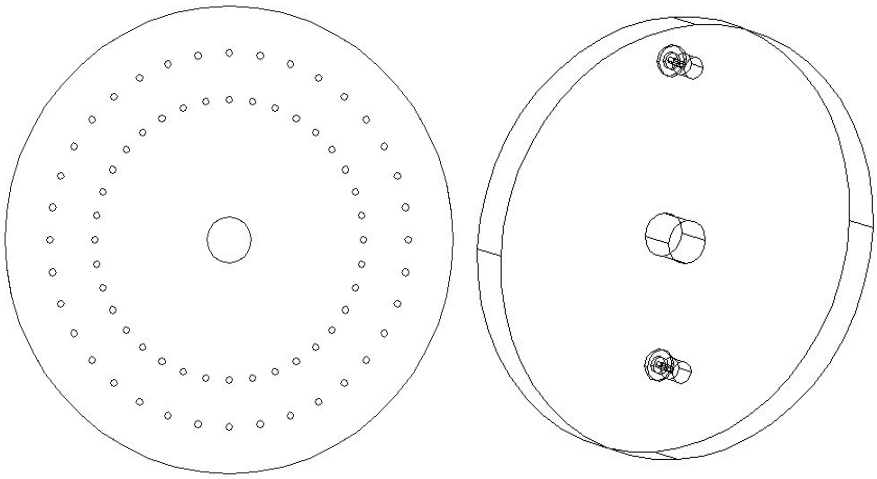

Figure 5: Two pieces of Pressure Tap Manifold

This pressure transducer had an additional signal conditioner with zero and span adjustments and a voltage signal output. The voltage output was read through a HP3497A data acquisition unit, which was controlled by a Dell desktop PC. The Validyne pressure transducer was calibrated with another factory calibrated pressure transducer. Its calibration curve can be seen in appendix #. An in house written controlling program would take voltage samples at 20 HZ for 60 seconds and then calculate the pressures and coefficients from the calibration. C_p, the static pressure coefficient, is defined below.

Static pressure Coefficient: $$C_P = \frac{P_{stat} - P_{sata,ref}}{\frac{1}{2} * \rho * U_{ref}^2}$$

P_{stat} is the measured static pressure, $P_{ststst,ref}$ is the upstream reference static pressure, ρ is the air density, and U_{ref} is the upstream channel velocity of 10.26 m/s. Additional 0.30 mm diameter pressure tap holes were drilled at location of 20 mm from the sealed end of

the stainless steel tubing. The hole at the 6 inch height was sealed off with glue, and several 20 mm spacers were made. This enabled us to make pressure measurements at 4.4% of the span. With the addition of the spacers, measurements were also made at 40 mm, 8.7% of the span, and 60 mm, 13.1% of the span. Uncertainties in pressure measurements are 0.7% and the corresponding calculated static pressure coefficient uncertainty is 6.0%.

3.2.2 Endwall Pressure Taps

The endwall pressure distribution was measured with several pressure taps in the bottom endwall. 77 taps in total were located throughout the bottom flat endwall in the center passage. Holes were drilled in the endwall to fit the 0.062 inch outside diameter hard plastic PEEK (Polyetheretherketone) tubing. The inner diameter of the tubing is 0.020 inch, which makes the pressure tap. Small lengths of the tube, 2-3 inches, were positioned in the holes and glued in place, leaving a small portion of the tubing protruding above the endwall. After the glue dried the small portion of the tube protruding into the main channel was cut flush with the endwall with a razor blade. This ensured any glue did not block the hole. Thin wire was then passed through the hole to ensure there was no blockage. Rubber tubing connected the hard plastic pressure taps to another rotating pressure manifold. This second rotating sealing pressure manifold was made to accommodate up to 135 pressure taps. The rest of the measurement system and calculations are the same as for the Blade Pressure Tap measurements. The pressure coefficient, C_p, is also defined in the same manner.

Static pressure Coefficient: $$C_P = \frac{P_{stat} - P_{sata,ref}}{\frac{1}{2} * \rho * U_{ref}^2}$$

For the contoured endwall 135 pressure taps were arranged in an one inch by one inch array throughout the main passage. The hard plastic tubing was installed in the same way as for the flat endwall, and the tap was made flush with the curved surface. Uncertainties in pressure measurements are 0.7% and the corresponding calculated static pressure coefficient uncertainty is 6.0%.

3.2.3 Hot Wire Anemometry

Velocity and turbulence measurements were made with a Constant Temperature Anemometer. This system is an IFA 300 with two channels made by TSI. Two different probes were used to make measurements in this facility. Both probes are pointed perpendicular to the probe holder. The first, probe model number 1245, measures components in the axial direction and the plane perpendicular to the probe holder. The second, model number 1246, measures components in the axial direction and the plane parallel to the probe holder. Both probes were calibrated with a model number 1128B TSI calibrator. This calibrator allows yaw and pitch angles to be adjusted from +/- 30 degrees. A MKS pressure transducer supplied with the calibrator measures the air velocity. Compressed air is supplied to the calibrator from the building. The supplied IFA 300 software is used to calibrate probes, acquire data, control the traverse, and post-process data. During calibration, velocity verses voltage is plotted. Different gains and offsets are used to maximize the voltage range for the desired velocity range. A fourth order polynomial curve fit, which closely approximates the measured velocity verses voltage, is calculated by the program. Next the velocity is held constant and measurements are taken at 11 different yaw or pitch angles ranging from -30 degrees to +30 degrees. For this calibration, the yaw or pitch portion was performed with three

different velocities but more or less can be used. The calibration curves and equations can be seen in the appendix.

The IFA program can not only acquire data but also control a traverse on which the probe is mounted. A two axis stepper motor traverse which could travel 240 mm on its first axis, the horizontal or pitch wise direction, and 190 mm on its second axis, the vertical or span wise direction, was used to take data in each slot. A Velmex VXM stepper motor controller controlled the traverse. Its drivers were loaded into the IFA software and the program could control the traverse. All that was needed was an input traverse file of X and Y coordinates. A second larger traverse which could travel 315 mm in the pitch wise direction and 265 mm in the span wise direction and an additional VXM stepper motor controller was purchased and used in conjunction with the first traverse. Both traverses took 400 steps to rotate the lead screws by one revolution and move the traverse by one millimeter. Very accurate resolution and repeatability was attainable.

When taking data an extra long 36 inch probe holder was used to reach the bottom of the test section. The fragile nature of hot wire probes requires special care when attaching and positioning the probes. To acquire data the correct traverse file and calibration file are chosen. The sample rate used was 5 kHz with 64 thousand points per channel, which lasted just over 13 seconds. After the traverse moved to a new position the system was set to wait 5 seconds before taking data. When taking hot wire data the temperature field must be constant. A thermocouple is placed in the upstream section of wind tunnel to monitor the air temperature at each position. This temperature is later used in a temperature correction equation to calculate the velocities. Once the data acquisition process is initiated it is self-automated and requires no outside input. Data acquisition

time would take anywhere from 6 to 16 hours depending on how many positions were in the traverse file.

Once data acquisition was finished post processing could begin. First, the IFA program was set to write velocity text files for each position data was taken at. These files simply listed the time, the first component of velocity, and the second component of velocity. A second in house written program was used to compute the various desired quantities. Most important are the average velocities and turbulence intensities. These quantities are defined as follows:

Average Velocity: $\overline{U} = \frac{1}{n}\sum_{n} u$

Variance: $\mu_2 = \frac{1}{n}\sum_{n}\left(u - \overline{U}\right)^2$

Turbulence Intensity: $TI = \frac{\sqrt{\mu_2}}{U_{inlet}} * 100\%$

The Turbulence Intensity was normalized by the upstream velocity in order to eliminate high turbulence intensities where the second component of velocity was near zero. Maximum uncertinities in hot wire velocity measurements is 2.3% while the turbulence intensity measurements have an uncertinity of 3.5%.

3.2.4 Five-Hole Probe

Three components of velocity and pressure losses were measured with a miniature five-hole probe. The probe's construction and data analysis was based on Ligrani et al. (1989). Five stainless steel hypodermic tubes were arranged in a lowercase t pattern. Each tube has an outside diameter on 0.032 inches, 0.8128 mm, and an inside diameter of 0.020 inches, 0.508 mm. One tube is in the center with two others on each side in the

horizontal plane, and two more are placed on top and bottom of the center in the vertical direction. The overall probe tip diameter is 0.096 inches, 2.4384 mm. The five tubes are soldered together and a curved 90 degree bend is made perpendicular to the horizontal plane about 1.5 inches from the probe tip. The probe tip is paid very special attention to. The center tube is cut flat while the four outer tubes are cut at 45 degree angles away from the center tube. A drawing of the five-hole probe can be seen in figure 6.

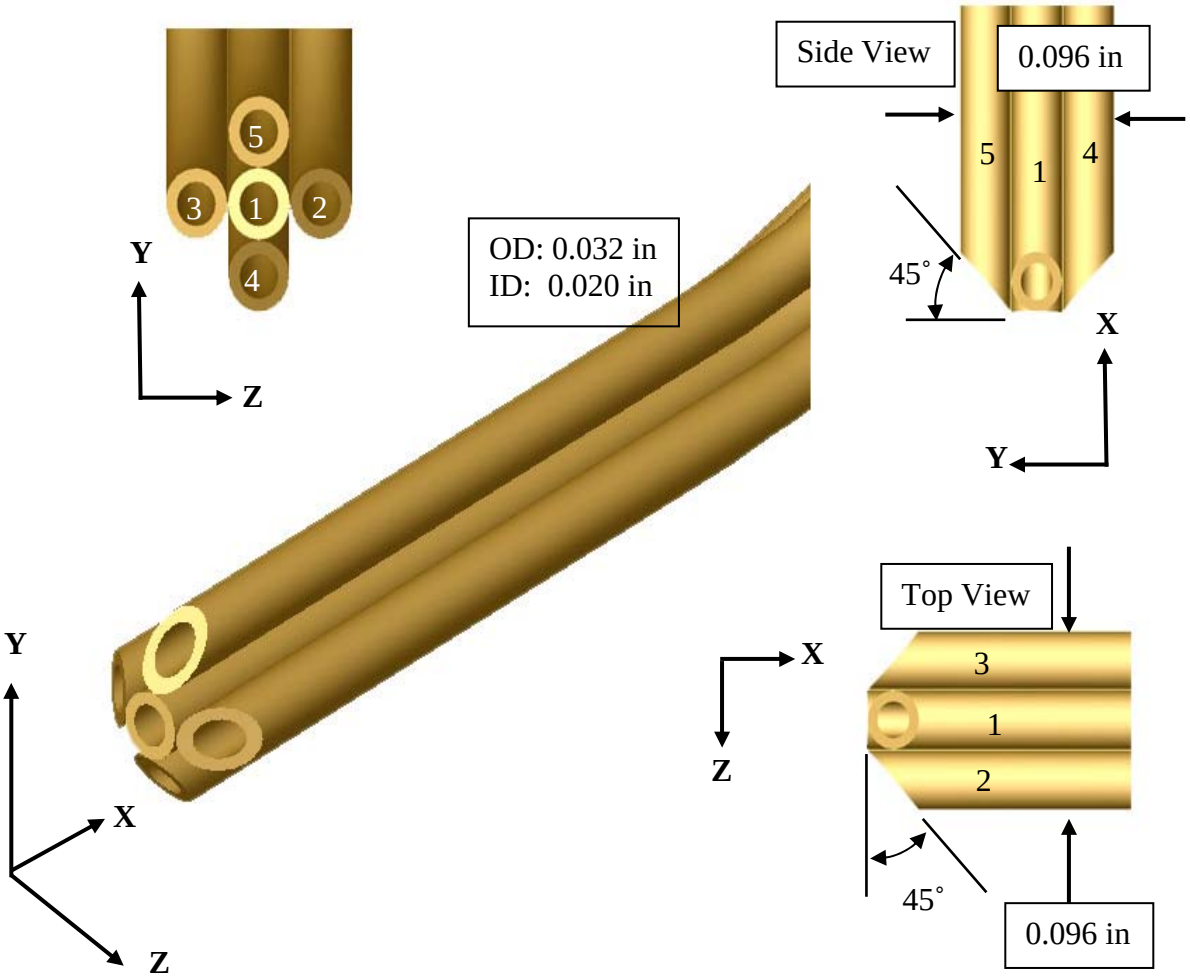

Figure 6: Five-Hole Probe Alignment

The probe shaft is approximately 25 inches long. At the top of the shaft is a small tube manifold made of five 0.25 inch diameter protruding metal tubes. This allows for rubber tubing to be connected to the five-hole probe. The probe is mounted and controlled by the

same traverse and motor controller as used by the hot wire anemometry system. Each of the five rubber tubes is then connected to its individual pressure transducer. Five Omega PX653-02D5V differential pressure transducers, manufactured to measure a pressure of up to 2 inches of water column, were used to take the measurements. These pressure transducers required an input voltage of 12 – 36 dc volts, which was supplied by one Protek power supply. They had an output of 1 – 5 dc volts, which represented the full scale pressure range. An Agilent 34970A data acquisition unit took voltage measurements. An in house written program controlled both the acquisition unit and the traverse from a Dell desktop PC.

The five-hole probe was calibrated in the upstream section of the wind tunnel with a constant velocity of 10.26 m/s. The yaw and pitch adjustment mechanism from the hot wire calibrator was mounted to the top wall of the tunnel. This allowed for 11 yaw angles and 11 pitch angles ranging from –30 to 30 degrees giving 121 calibration points. During calibration the total pressure and static pressure are also measured for coefficient calculation. All the various coefficients for each known yaw and pitch angle are then calculated according to Ligrani et al. (1989). Calibration curves can be seen in the appendix. The yaw and pitch coefficients are given as follows:

Yaw Coefficient: $$C_{py} = \frac{P_2 - P_3}{P_1 - \overline{P}}$$

Pitch Coefficient: $$C_{pp} = \frac{P_4 - P_5}{P_1 - \overline{P}}$$

Average Pressure: $$\overline{P} = \frac{P_2 + P_3 + P_4 + P_5}{4}$$

The numbered subscripts indicate which tube the pressure is measured at. During data acquisition 200 samples are taken at 20 Hz for each transducer. After the probe moves to a new position it waits for 25 seconds before taking data to allow for the pressure lag in the small tubes. Once data acquisition is complete post processing begins. First a pressure correction is applied which adjusts pressures based on spatial differences between hole locations. Then the pitch and yaw coefficients are calculated. An interpolation scheme is next used to determine the yaw and pitch angles. Pressure coefficients, velocities, and relative pressures are then calculated using various interpolation schemes from the calibration points. Finally a downwash correction is applied which corrects for perpendicular velocities. The pressure loss coefficients are defined as follows:

Total Pressure Loss Coefficient: $$C_{pt} = \frac{P_t - P_{t,ref}}{0.5 * \rho * U_{ref}^2}$$

Static Pressure Loss Coefficient: $$C_{ps} = \frac{P_s - P_{s,ref}}{0.5 * \rho * U_{ref}^2}$$

P_t is the total pressure, P_s is the static pressure, $P_{t,ref}$ is the upstream total reference pressure, and $P_{s,ref}$ is the upstream stagnation reference pressure. When taking data, it was insured that the probe tip never came closer than 4 mm to either the endwall or blade surface. This is because the probe tip can influence the flow structure in this small gap and give false readings. When traversing along one pitchwise slot the probe was oriented in the average inviscid streamwise direction in order to minimize yaw and pitch angle corrections.

Originally a smaller five-hole probe of tip diameter 0.048 inches, 1.22 mm, was made. The hole diameter was 0.008 inches, 0.203 mm. This probe proved to have a very long time lag. It took 80 seconds for the pressure signal to stabilize. Taking data in one

slot would take too long for a reasonable resolution and was impractical. Thus the larger 0.096 inch probe was made and had a much faster response time.

Uncertainty in total pressure calculations are 1.1% in the invscid region and 2.0% near the endwall. Uncertainty in static pressure calculations are 0.8% in the invscid region and 1.1% near the endwall. Corresponding total pressure and static pressure coefficient uncertainties are 7.2% and 6.5%, respectively. Pitch and yaw angle uncertainties are higher in the secondary flow region. They are 2.5% in the inviscid region and 12.0% in the secondary flow region. Velocity and vorticity calculations have a maximum uncertainty of 3.0% and 7.0%, respectively.

3.2.5 Thermocouple Probe

Air temperature profiles in the planes of the pitchwise slots were measured with a thermocouple probe. An E-type thermocouple with a bead size of less than 0.010 inches was inserted and sealed to a 0.034 inch diameter stainless steel tube. The thermocouple calibration curve can be seen in the appendix. This tube was then connected and sealed to a 0.134 inch diameter steel tube and finally connected and sealed to 3/16 inch diameter tube. The largest tube, which was used for added strength and rigidity, made up most of the length of the 28 inch long probe. The probe was moved and controlled by the same traverse and motor controller as used with the hot wire and five-hole probes. The Agilent 34970A data acquisition unit read the thermocouple voltage. An in house written program controlled the traverse and acquisition unit. At each location the probe would wait for five seconds and then take 240 voltage samples at 20 Hz. A non-dimensional temperature, theta, was then calculated and is defined as follows:

Theta: $$\Theta = \frac{T - T_{in}}{0.5 * U_{ref}^2 / C_p}$$

T is the local temperature and T_{in} is the upstream inlet temperature.

A constant heat flux of 1600 W/m^2 was provided on the endwall by flat kapton heaters. The heating begins approximately 1.73*C_{ax} upstream of the center blade's leading edge. Heating continued through the passage and just past the blade's trailing edge. Most of the heaters were rectangular in shape and either DC power supplies or AC variac supplied the power. For the contoured endwall a customized in house heater was made. Kapton layers and strips of copper tap were used to make a heater that followed the curved surface. The inlet temperature remained constant, and the thermocouple probe could effectively measure air temperature profiles created by the endwall heaters and secondary flows. Thermocouple temperature measurements have a very low uncertainty level of 0.2%.

3.2.6 Flow Visualization

Smoke flow visualization was performed in order to get qualitative flow structure information. A toy train liquid smoke called Supersmoke made by Bart's Pneumatics Corp provided the smoke. Nickel chromium wires heated the liquid smoke. These 0.02 inch diameters wires were straitened by stretching. Nine wires in total were used and were arranged parallel to the endwall, spanning across the width of the inlet channel. Their heights ranged from ¼ inch to 2.25 inches above the endwall, creating smoke inside and outside of the boundary layer. They were located about 1.5*Cax upstream of the center blade's leading edge and can be seen in Figure 2. DC power supplies applied sufficient current to the wires to heat them and create smoke. During heating the wires

would stretch and sag causing them to no longer be parallel to the endwall. To keep the wires taught, non-conductive heavy bricks were tied to one end and allowed to hang. The wires were routed through wood so each was electrically separated from one another. The liquid smoke was simply coated on each wire before a test was run. When air was flowing through the tunnel white sheets of smoke parallel to the endwall were created. The smoke sheets would then be twisted and contorted into the secondary flow shapes and structures.

A light plane was used to capture the secondary flow structures in various planes, which are illustrated in Figure 5.

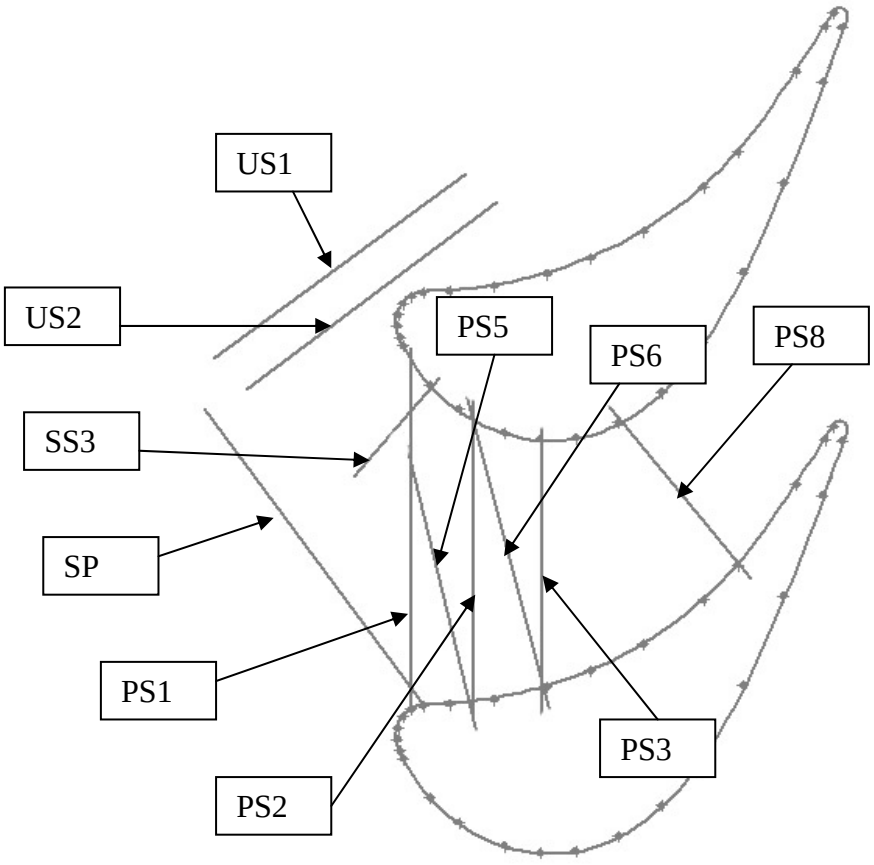

Figure 7: Flow Visualization Planes

The light plane was created with a 1000 watt theatrical lamp. The lamp was placed atop a 30 inch tall wooden box, which was coated with reflective aluminum tape on the interior surfaces. Half way down the wooden box was a thin flat metal sheet with a 1/16 inch wide slot across its length. This helped concentrate the light in the center of the box. At the bottom of the box was another flat sheet of metal with a 0.063 inch wide slot across its length. This slot focused the light into a bright thin sheet. The two slots were aligned in the same plane. A tall box was used because it seemed to make the light plane thinner and brighter. When experiments were run all the other lights in the lab were turned off, and only the smoke in the light plane could be seen. A trip wire, 1.30 mm diameter, was placed approximately 4.7 * Cax upstream of the center blade on the bottom wall in order to create a thicker boundary layer.

As mentioned before, the side walls of the wind tunnel are made of transparent acrylic. A Sony DFW-V500 digital video camera was used to capture videos of the smoke flow patterns. Video was captured with a resolution of 640 x 480 at 33 Hz with software provided by camera manufacture. The camera was connected to a Dell desktop PC by a firewire cable, and the video was stored on the PC. Still frames from the videos were captured with Ulead Video Studio 4.0 SE Basic. Images were further enhanced by brightness and contrast changes in Adobe Photoshop v8.10. The camera was positioned perpendicular to each light plane and remained in the same position for the baseline, filleted cases, and contoured endwall. In order to produce smooth sheets of smoke the upstream velocity had to be turned down to approximately 0.80 m/s. This resulted in a Reynolds number of 18,200.

3.3 Fillet Design and Fabrication

Leading edge fillets were the first secondary flow control method employed. Several researchers had published information on various shapes and sizes of fillets. The current fillet designs were based on the work of Saucer et al. (2000), Zess et al. (2001), and Shih et al. (2002). In all, four different fillets were designed. The four fillet shapes and dimensions can be seen in figure 8 and table 2.

Table 2: Fillet parameters

Fillet Name	Description	$(Y/S)_{max}$	$(X/C_{ax})_{max}$	s_{ss}/C_{ax}	s_{ps}/C_{ax}
Fillet 1 (EW&B)	Blends into the end-wall and blade wall with a linear profile	0.10	0.299	0.566	0.322
Fillet 2 (EW)	Blends into the end-wall only with a linear profile	0.10	0.299	0.566	0.322
Fillet 3 (B)	Blends into the blade wall with linear profile	0.10	0.299	0.566	0.322
Fillet 4 (Curved EW&B)	Blends into the end-wall and blade wall with a curved profile	0.10	0.299	0.566	0.322

Each fillet had a maximum height, Y/S, at the blade's stagnation line. of one boundary layer thickness and a maximum length in the oncoming flow direction, X/Cax, of two boundary layer thickness. One fillet was located at each blade leading edge and endwall junction on the bottom endwall. No fillets were located at the top endwall. Fillet #1, Endwall and Blade Blend (EW&B), fillet #3, Blade Blend (B), and fillet #4, Curved Endwall and Blade Blend (curved EW&B), all had the same outer periphery on the endwall surface. This periphery was created with two different ellipses on either side of the stagnation plane. The ellipse on the suction side is larger and extends further downstream then on the pressure side. A circular arc was added to the end of the pressure side to make the fillet blend smoothly into the pressure surface.

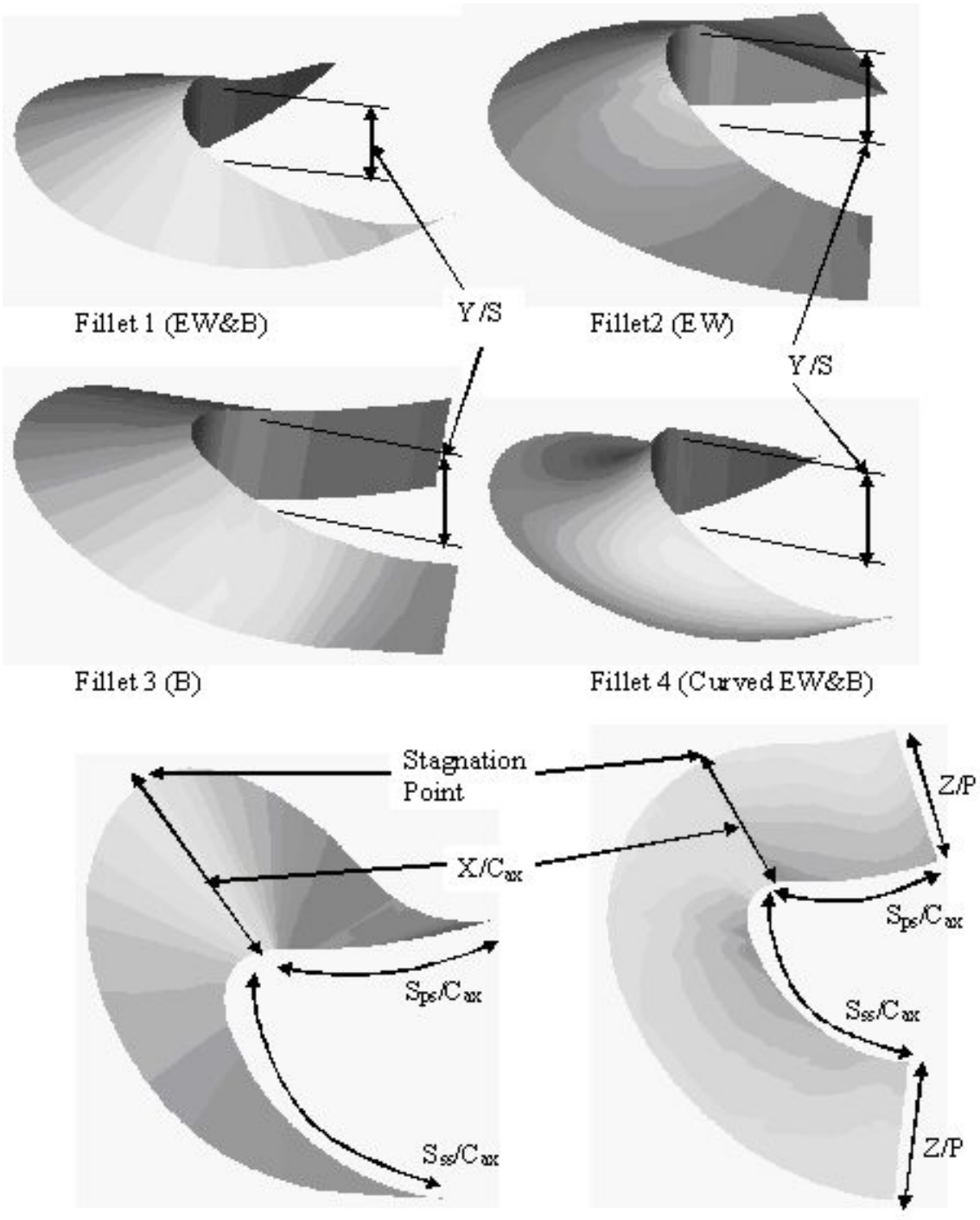

Figure 8: Fillet Shapes and defining dimensions

The periphery of fillet #2, Endwall Blend (EW), was created with a constant thickness perpendicular to the blade surface. The height at the blade surface of fillet #1 (EW&B), fillet #2 (EW), and fillet #4 (curved EW&B) decreases from the maximum at the

stagnation line to zero at each edge. Fillet #3 (B) has a constant height along the blade surface. Fillet #1 (EW&B), fillet #2 (EW), and fillet#3 (B) have a linear surface profile from the blade surface to the outer edge. Fillet #4 (curved EW&B) has a concave circular arc surface profile, which is tangent to the endwall at the outer edge. A 3-D model of each fillet was created in the CAD program Solidworks™. Three fillets of each were then built with an in house Dimension rapid prototype 3-D printer. The printer uses ABS plastic and builds one layer at a time. It can build any solid object that can fit in an 8 in x 8 in x 12 in box with a layer resolution of 0.01 inches. Manufacturing costs were minimal because only material cartridges had to be purchased.

3.4 Non Axis-Symmetric Contour Endwall Design

The second secondary flow control device employed was a non axis-symmetric contoured endwall. Most contoured endwalls have only a two dimensional curvature in the axial direction. A non axis-symmetric contour also has curvature in the tangential or pitchwise direction, making the endwall fully three dimensional. A few researchers have explored this topic including Gregory-Smith, Harvey, and Hartland. The main objective of their work was to create a more uniform exit flow field and exit endwall pressure distribution. Gregory-Smith suggested that making the endwall pressure distribution more uniform in the main passage would reduce crossflow and in turn reduce the secondary flow. The objective for this contoured endwall was to reduce the cross passage pressure gradient, creating weaker crossflows and secondary flows. The basic idea for doing this is to raise the endwall near the pressure side of the blade with convex curvature and lower the endwall near the suction side with concave curvature. The raised region, or hill, would accelerate the flow and create lower pressures on the endwall near the pressure

side of the blade. The lower region, or trough, would decrease the flow speed and create higher pressures near the suction side of the blade. This should reduce the cross passage pressure gradient.

The endwall contour was created with two continuous curves, one in the axial direction and another in the tangential direction. The two curves were then multiplied by each other to create the surface. Several combinations of different curves were first evaluated using a computational fluid dynamics (CFD) program called FLUENT^{TM}. The contour, which showed the better overall heat transfer reduction and lower pressure drop, was chosen for experimental evaluation. The tangential, pitchwise, curve starts high and flat near the pressure side of the blade then continues with a sine curve down to a trough. Another sine curve increases up to the suction side of the blade to the same height as on the pressure side. The trough is located very near to the suction surface. The axial, streamwise, curve starts upstream of the leading edge at X/Cax = -0.13 with a sine curve and increases to a maximum the height at X/Cax = 0.33. Another sine curve decreases the height to zero after the trailing edge at X/Cax = 1.45. The maximum height of the contour is 39 mm, 8.5% of the span, near the pressure surface. The lowest point of –46 mm, -10.1% of the span, is in the trough near the suction surface. The baseline flat endwall gives the reference height of zero. Figures of the two curves can be seen in figure 9. Figure 10 shows a contour of the endwall height.

A three dimensional model of the contoured endwall was made in Solidworks. A uniform thickness of 19 mm was given for the entire endwall to ensure conduction loses would be equal everywhere during heat transfer experiments. 145 spanwise holes with a

0.062 inch diameter were arranged in an one inch by one inch array, covering the entire endwall. These holes would allow for thermocouples and pressure taps.

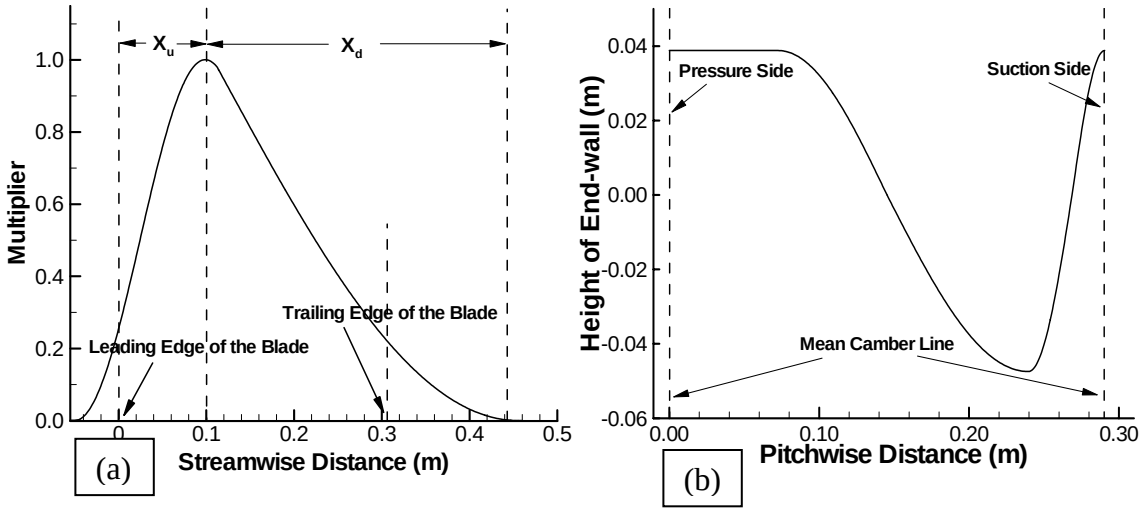

Figure 9: Contour Endwall Generation Curves (a) streamwise, (b) pitchwise

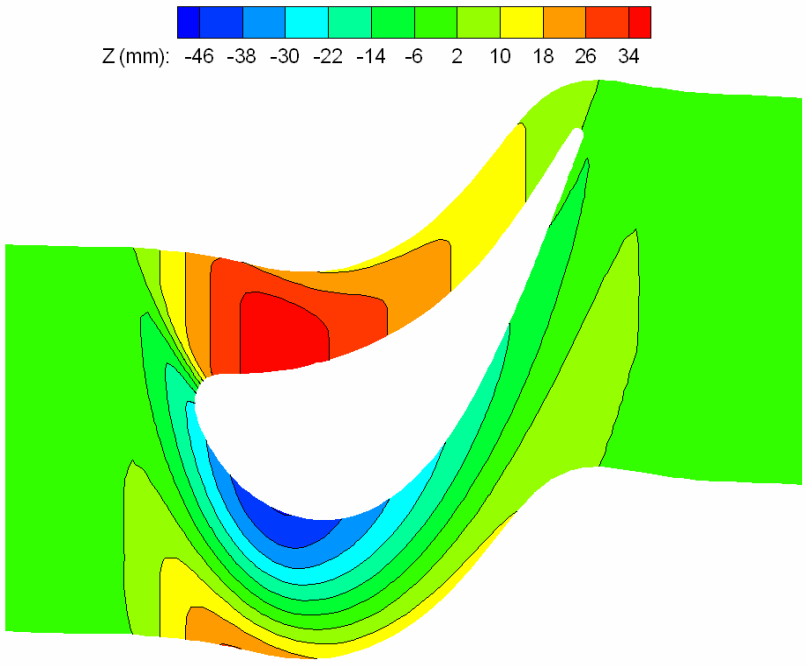

Figure 10: Contour Endwall height in meters

Figure 11 shows the relative hole and blade locations. Manufacturing was performed with the same Dimension 3-D printer as used with the fillets. Because the contoured endwall

was too large to print in one piece, it was broken into several smaller pieces and later assembled with wood pins and epoxy. Since parts of the contoured endwall's height decreased below that of the baseline flat endwall, extensions were added to the blades. Wood putty was used to seal the blade to the contoured endwall.

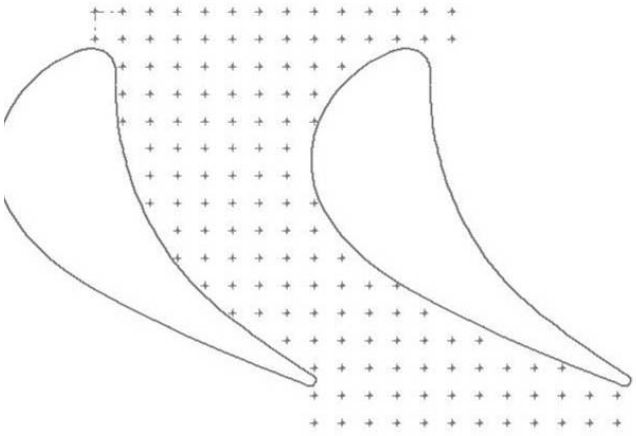

Figure 11: Contoured Endwall Pressure Tap and Thermocouple Locations

3.5 Film Cooling Design

Film cooling was next employed to counter the ill effects of heat transfer on the endwall created by secondary flows. Knost et al. (2004) suggested placing cooling holes along iso-mach lines and performed experiments with holes along iso-velocity lines. For the current study holes were placed along logical lines, which formed perpendiculars to streamlines near the endwall. It has been shown that the local flow field and not the coolant ejection angle largely dominate the coolant flow path. With perpendiculars to streamlines, it was believed that coolant from one hole would not interfere or mix with that of another and be wasted. As suggested by industry contacts more holes were located near the pressure side of the blade, and few holes were placed in or downstream of the throat area. The film cooling hole pattern can be seen in figure 12.

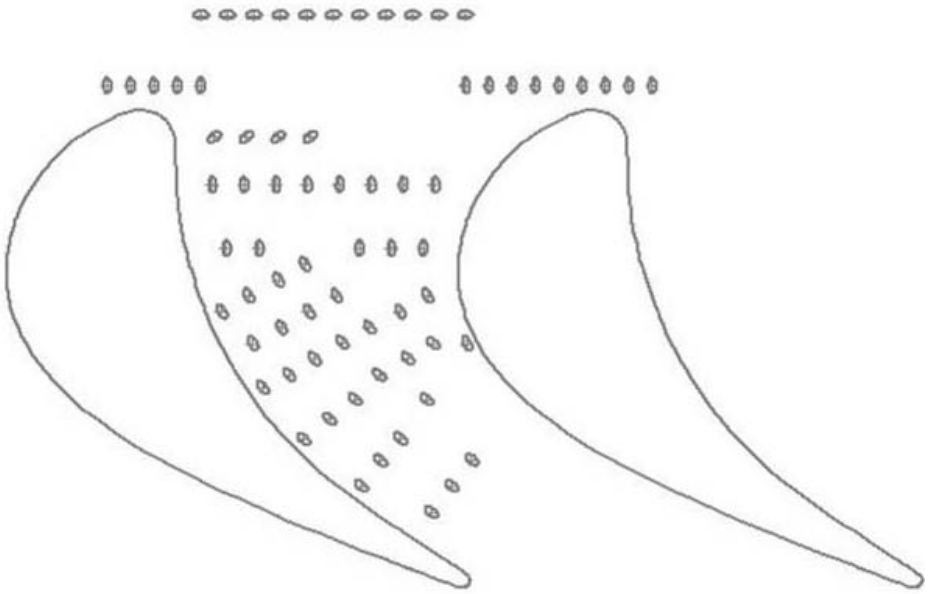

Figure 12: Film Cooling Hole exit locations

A row of holes along a pitchwise line was placed just upstream of the leading edge to cool this high heat transfer region. Another row of upstream holes was located at an X/Cax location of –0.2, and ejected coolant in the pitchwise direction from pressure side to suction side. All holes are 5.0 mm in diameter and have an ejection angle of 30 degrees away from the surface. The ejection angles for the contoured endwall were made to be 30 degrees relative to the surface angle at the hole exit. Holes located in the center of the passage are arranged in the approximate local inviscid streamwise direction. The L/D, length over diameter, ratio for the flat endwall is 7.6, but the ratio could not be maintained consistently on the contoured endwall. Special provisions had to be made to ensure the holes were not too long or interfere with each other on the contoured endwall. Small groves were made vertically up from the bottom surface to shorten the length of some of the longer holes. Only the center passage was cooled. A three dimensional model of the film cooled contoured endwall was made in Solidworks and manufacture in the Dimension 3-D printer.

It was desired to create a 25 C temperature difference between the main passage flow and the injected coolant. The coolant air would have to be cooled to near 0 C with an additional coolant loop. A schematic of the coolant loop can be seen in figure 13. Air enters a 2in diameter pipe and the mass flow is measured with an orifice plate of beta ratio 0.50. An in house written program iteratively calculates the mass flow rate based on the measured pressure drop. The flow rate can be controlled with a gate valve downstream of the orifice plate. A small vacuum blower, Ametek model number 115334, then pumped air through the system. Air was next cooled in a heat exchanger box with two heat exchangers. The first heat exchanger is an accumulator from a car air conditioning system. The second is a Lytron aluminum heat exchanger model number ES0505G23. An antifreeze water mixture was supplied to these heat exchangers in a crossflow arrangement by a Teel water pump model number 1P579E. The antifreeze is first cooled in a freezer by pumping it over small bags of ice. The ice is brine saltwater mixture, which freezes at approximately –21 C. The latent heat of fusion of the brine was measured to be approximately 220 kJ/kg. This would produce a constant temperature bath for the required time to take measurements, and thus the air coolant temperature would also remain constant. The cooled air would then go into a large plenum underneath the test section. The plenum supported this portion of the test section, the blades, and the contoured endwall. One baffle was used in the plenum to even out the pressure distribution. A few thermocouples and pressure taps were mounted inside the plenum to monitor the temperature and pressure.

Film cooling experiments are performed at different blowing ratios. Two blowing ratios are defined, an inlet blowing ratio (M_{inlet}) and a local blowing ratio (M).

Inlet Blowing Ratio: $$M_{inlet} = \sqrt{\frac{Po_{plenum} - p_{inlet}}{Po_{inlet} - p_{inlet}}}$$

Local Blowing Ratio: $$M_{inlet} = \frac{\rho_{coolant} * V_{coolant}}{\rho_{inlet} * V_{inlet}}$$

Po_{inlet} is the stagnation pressure in the inlet reference plane, Po_{plenum} is the stagnation pressure in the plenum, and p_{inlet} is the total pressure in the inlet reference plane. $V_{coolant}$ is the coolant velocity at the exit of a film cooling hole, and V_{inlet} is the upstream reference velocity.

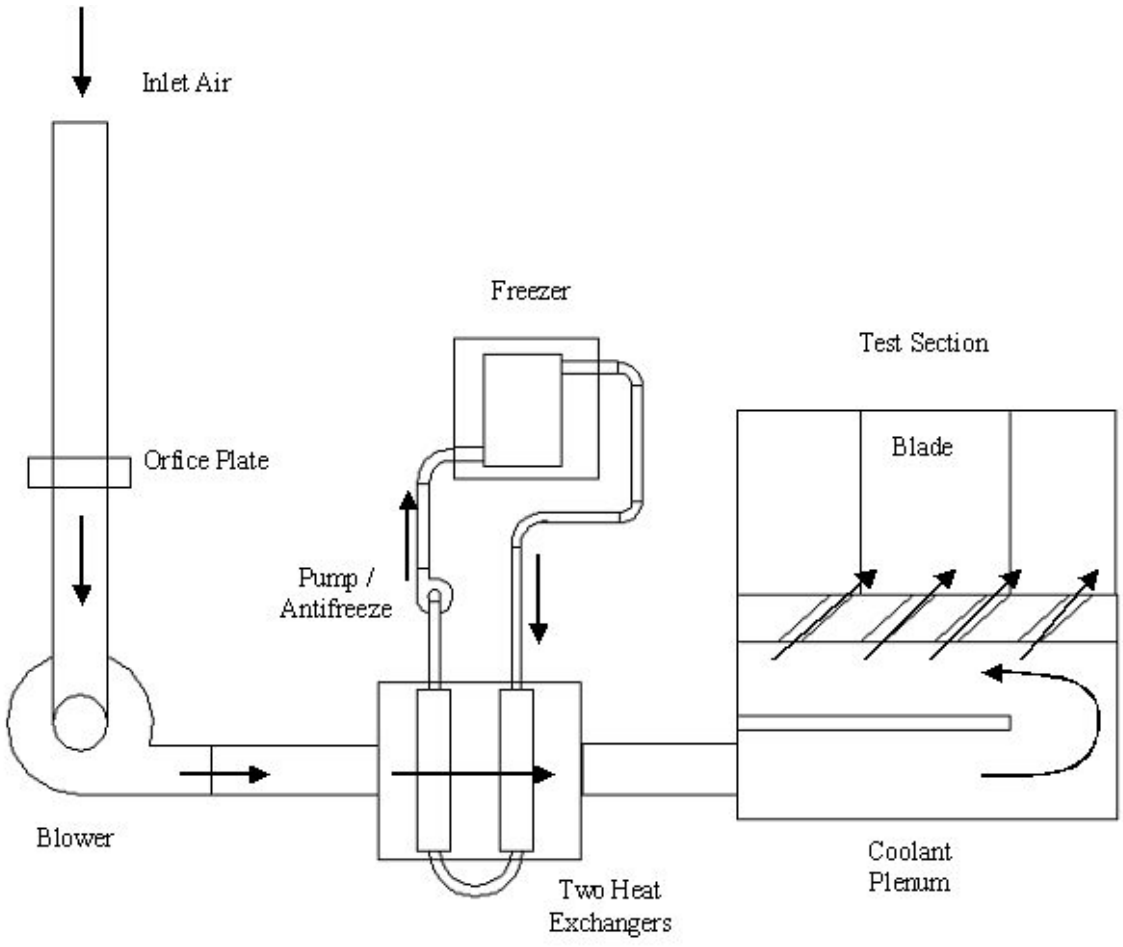

Figure 13: Cooling Loop Setup

Chapter 4. Results

This section will present the results and conclusions on the baseline, fillets, contoured endwall, and film cooled contoured endwall. Each particular case's reference velocities and pressures were used to normalize all the presented data. Table 3 shows all the geometrical configurations tested and what measurements were taken.

4.1 Channel Balancing

Channel balancing was first carried out to ensure equal mass flow through both channels. Figure 14 shows the static pressure coefficient distributions along the blade surface for baseline, fillets, and the contoured endwall at a spanwise location of *Y/S*=0.33. The C_p coefficients are determined from the difference of measured reference static pressure and surface static pressure normalized by the reference dynamic head. The blade surface coordinate s/C=0.0 is located at the suction side trailing edge. As shown, the C_p distributions are the same with and without the fillets. This illustrates the fact that the pressure distribution on the blade surface in the inviscid region is generally unaffected when the fillets are employed. However, it is premature to make conclusions about the overall blade loading on the filleted blade surface based on these C_p data. The blade profile pressure distributions are expected to be affected near the endwall with the fillets.

4.2 Boudary Layer Measurements

The upstream boundary conditions and reference quantities used to normalize data are presented in Table 4. The upstream data are measured in a plane located 100 mm upstream of the inlet plane of the blade passage. Both the hot-wire anemometer and the

five hole pressure probe are used to measure the upstream conditions. The mean velocities with the two measurement techniques agree quite well with each other. Reference quantities in Table 4 are the ensemble averages of the data measured in this plane. Since the cascade operates in a suction mode, the pressures measured are below atmospheric pressure. The boundary layer properties in the table are estimated by numerically integrating the measured velocity data using the Matlab™ function "trapz.m."

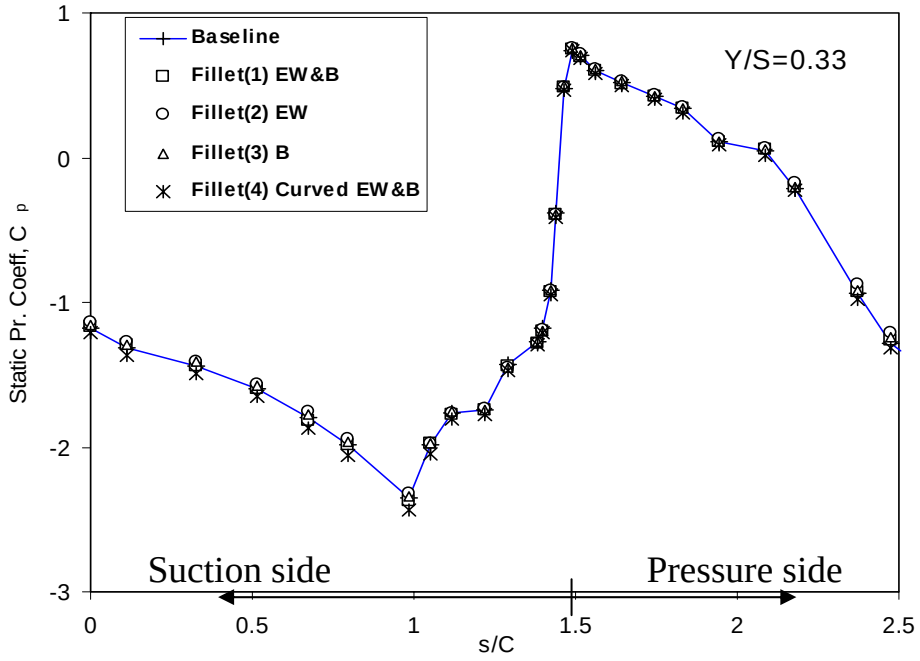

Figure 14: Blade Surface Static Pressure Coefficient

Table 3: Upstream Boundary and Reference Properties

Average upstream reference velocity, U_{ref} (m/s)	10.26
Average reference static pressure (below atmospheric), $P_{stat,0}$ (Pa, gage)	121.9
Average reference total pressure (below atmospheric), $P_{tot,0}$ (Pa, gage)	60.5
BL thickness, δ (mm)	46.0
Displacement thickness, δ1 (mm)	8.4
Momentum thickness, δ2 (mm)	6.6

Table 4: Experimental Configurations

Measurement	Endwall Geometry	Leading Edge Geometry	Description	Reference Velocity
Blade Surface Pressure	Flat	None, Fillet #'s 1,2,3,4	Y/S = 0.04, Y/S = 0.09, Y/S = 0.13, Y/S = 0.33	10.26 m/s
Blade Surface Pressure	Contoured Endwall	None	Y/S = 0.33	10.145 m/s
Endwall Surface Pressure	Flat	None, Fillet #'s 1,4	77 pressure taps	10.26 m/s
Endwall Surface Pressure	Contoured Endwall	None	135 pressure taps	9.84 m/s
Instantaneous Flow Structure Smoke Flow Visualization	Flat	None, Fillet #'s 1,2,3,4	Stagnation Plane, X/Cax = 0.05, X/Cax = 0.285	0.80 m/s
Instantaneous Flow Structure Smoke Flow Visualization	Contoured Endwall	None	Stagnation Plane, X/Cax = 0.17, X/Cax = 0.285, Suction Side Planes, Pressure Side Planes	0.80 m/s
Flow Structure: Hot Wire Anemometry	Flat	None, Fillet #'s 1,2,3,4	X/Cax = 0.16, X/Cax = 0.50, X/Cax = 0.97	10.26 m/s
Flow Structure: Hot Wire Anemometry	Contoured Endwall	None	X/Cax = 0.16, X/Cax = 0.50, X/Cax = 0.97, X/Cax = 1.26	10.84 m/s
Flow Structure: Hot Wire Anemometry	Film Cooled Contoured Endwall	None	X/Cax = 0.50, X/Cax = 0.97	10.84 m/s
Flow Structure: 5-Hole Pressure	Flat	None	X/Cax = 0.16, X/Cax = 0.50, X/Cax = 0.97, X/Cax = 1.26	10.26 m/s
Flow Structure: 5-Hole Pressure	Flat	Fillet #'s 1,2,3,4	X/Cax = 0.97, X/Cax = 1.26	10.26 m/s
Flow Structure: 5-Hole Pressure	Contoured Endwall	None	X/Cax = 0.16, X/Cax = 0.50, X/Cax = 0.97, X/Cax = 1.26	10.145 m/s
Flow Structure: 5-Hole Pressure	Film Cooled Contoured Endwall	None	X/Cax = 0.50, X/Cax = 0.97	10.145 m/s
Flow Temperature	Contoured Endwall	None	X/Cax = 0.16, X/Cax = 0.50, X/Cax = 0.97	10.145 m/s

4.3 Fillet Results

The baseline measured endwall static pressure coefficients, defined the same way as the blade surface static pressure coefficients, can be seen in figure 15. The two green regions are the blades. A high pressure region can be seen near the pressure side of the bottom blade at the entrence to the passage. The lowest pressures exist near the suction surface in the throat region. This pressure gradient drives the crossflow which strengthens the passage vortex. Figure 16 and 17 show the measured endwall pressure coefficients for fillet 1 and fillet 4, respectively. The fillets covered the pressure taps around the leading edge so no data exists in that region. Besides the immediate vicinity around the fillets, the overall endwall pressure distribution is not affected.

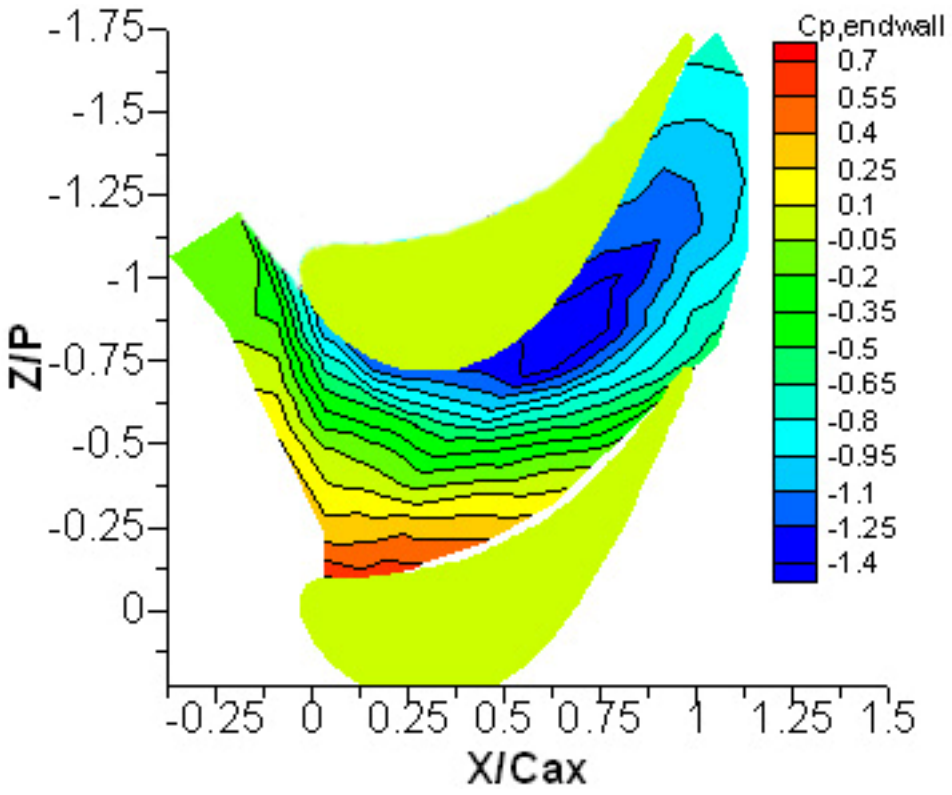

Figure 15: Baseline Endwall Static Pressure Coefficient

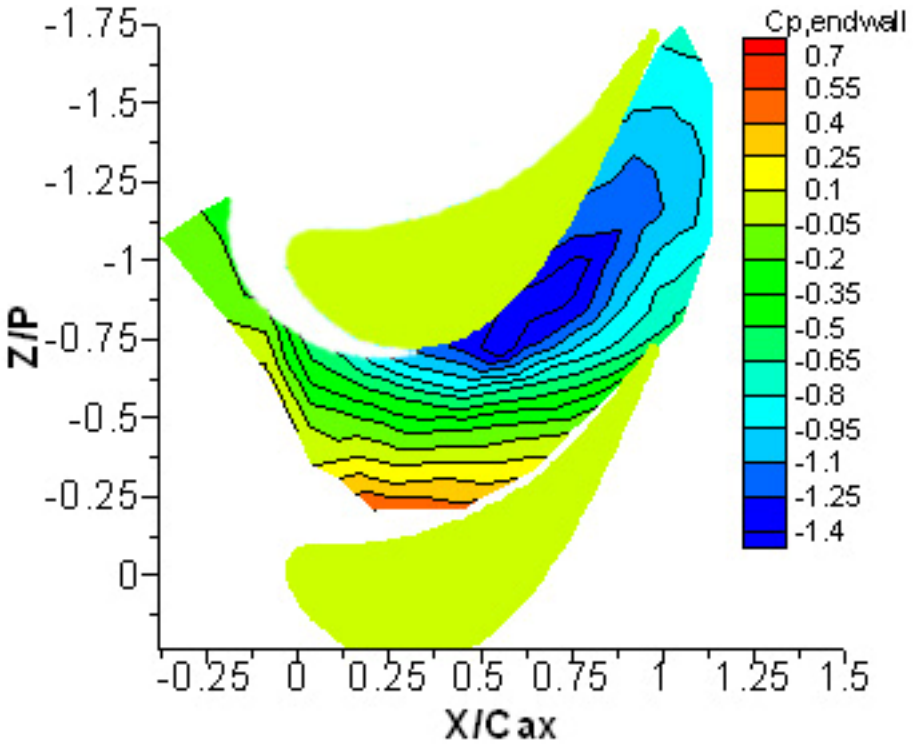

Figure 16: Fillet #1 Endwall Static Pressure Coefficient

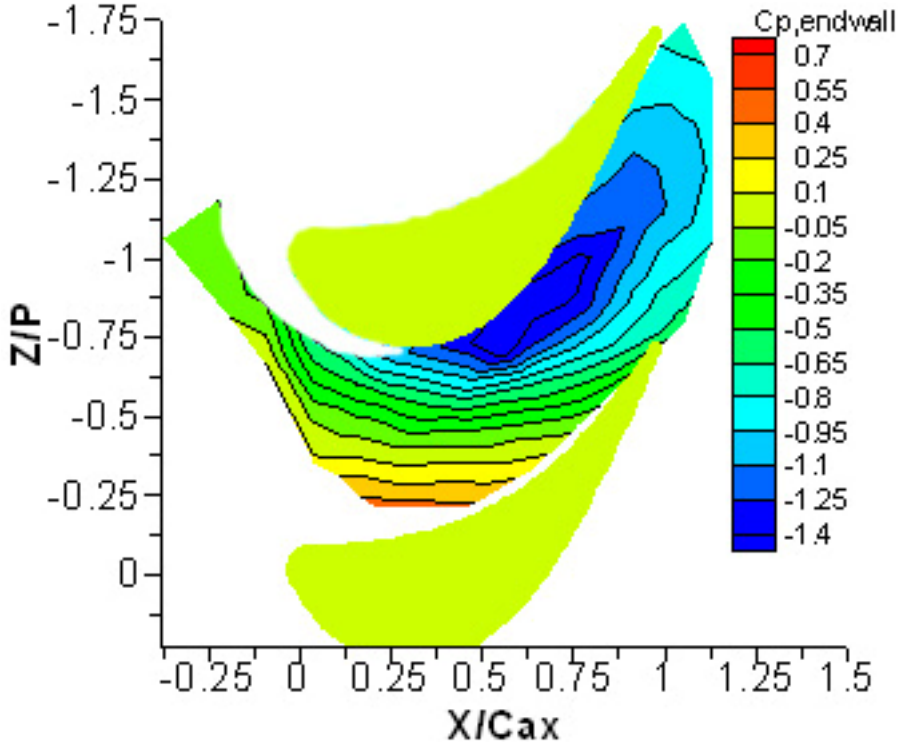

Figure 17: Fillet #4 Endwall Static Pressure Coefficient

4.3.1 Instantaneous Secondary Flow Structures

Instantaneous images from smoke flow visualization are obtained in three planes, the stagnation-line plane and two parallel planes inside the passage between the center blade and the pressure side blade. The planes inside the passage are parallel to the inlet plane and located at the axial distances X_G/C_{ax}=0.05, PS1, and 0.285, PS3. Figure 18 to figure 20 present snapshot images of secondary flow patterns in these three planes for the baseline case, and for the case when the leading edge is contoured with the fillets. The locations of each light plane and camera view are also shown in the figures.

In figure 18, all the images show a clear structure of the horseshoe vortex. The horizontal bright white line at the bottom of each image is the location of the end-wall, and the wedge shaped object represents the fillet. The top horizontal smoke line in the images is located about 55 mm above the end-wall. When the size of the horseshoe vortex patterns in figure 18 is compared, it is clearly evident that the vortex patterns are smaller for the fillets than for the baseline. As the boundary layer moves up the fillet surface along the stagnation-line plane, the flow area in the blade-span direction is reduced. This leads to the boundary layer fluid being displaced away from the stagnation-line plane to maintain mass conservation. Therefore, the reduction in the size of the horseshoe vortex can be considered to be a consequence of the displacement of the boundary layer fluid away from the stagnation location. Further, the fillets introduce a pressure gradient in the direction from the fillet leading edge to the blade leading edge. This is counter to the adverse pressure gradient on the blade/fillet leading edge that drives the horseshoe vortex. Thus, the presence of the fillet reduces the size of horseshoe vortex in the leading edge region. Also, immediately behind the visible horseshoe vortex in the

images of figure 18, smoke traces indicate the development of a secondary vortex. The apparent shape and size of this second structure is about the same as the primary horseshoe vortex. The two structures merge into one periodically as has also been shown by Wang et al. (1997). The primary vortex structure for the baseline, unfilleted case, is at least twice the size observed for the filleted cases.

Figure 19 presents the instantaneous structures of the pressure side leg of the horseshoe vortices in the pitchwise Y-Z plane at X_G/C_{ax}=0.0. The pressure side of the passage is located on the right side of each image, and it's outline along with that of the end-wall can be seen in the images. A pair of distinct vortices, which roll-up in a clockwise rotation, is visible for all cases. Due to the pitchwise displacement of the flow by the fillets, the location of the vortex pair is farther from the pressure side for the filleted cases when compared to the baseline. The location of these vortex structures also depend on the strength of the cross flow, which sweeps the structures towards the suction side. The right side vortex of the pair represents the primary horseshoe vortex in the stagnation plane. In general, the size of this primary pressure-side vortex is smaller for the filleted cases (consistent with the size of the structures in the stagnation plane) when compared to the baseline. Fillets 1, 2 and 4, which blend into the EW, show a smaller structure than fillet 3, which blends only to the blade. The second vortex on the left of the pair is also smaller for the filleted cases. As noted earlier, the vortex structures do exhibit some periodic unsteadiness, with the two vortex-structures periodically merging into a single structure. This is also observed in the pair of pressure side vortices in figure 19.

Figure 20 presents flow visualization images in the pitchwise plane at X_G/C_{ax}= 0.285. The main flow direction is into the plane of the image, and the right and left edge

of the images correspond to the pressure and suction side of the passage, respectively. As the location of this image plane is farther downstream, the passage vortices are now located closer to the suction side, being driven there by the cross flow pressure gradients. While there are essential differences in the vortex structures for the various cases, at this axial location, the size of the structures appear to be comparable. However, the locations of the passage vortices appear to be nearer to the suction side for the filleted cases than for the baseline.

From the images shown in figures 18-20, it would appear that the fillets reduce the size of the secondary flow structures near the leading edge, and upstream of the throat. However, downstream of X_G/C_{ax}= 0.285, the secondary flow structures appear to have grown to comparable sizes. The main role of the fillets, from smoke visualization, appears to be a shift of the structures toward the suction surface. It should be noted that these flow visualization experiments are performed at lower Reynolds numbers than those of the five-hole probe and heat transfer measurements. Therefore they only provide a qualitative measure of the effects of the fillets.

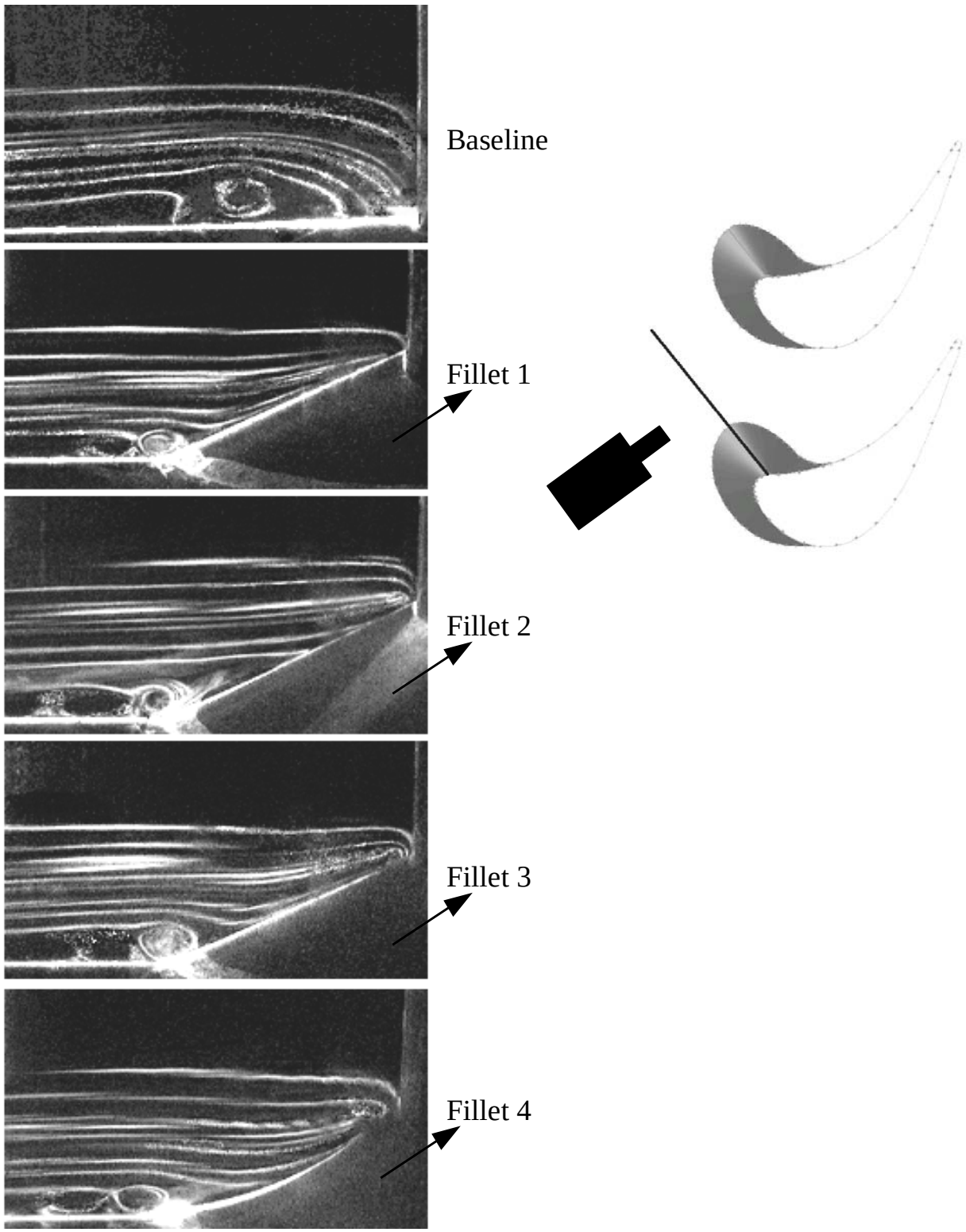

Figure 18: Flow Visualization Baseline / Fillets in Stagnation Plane

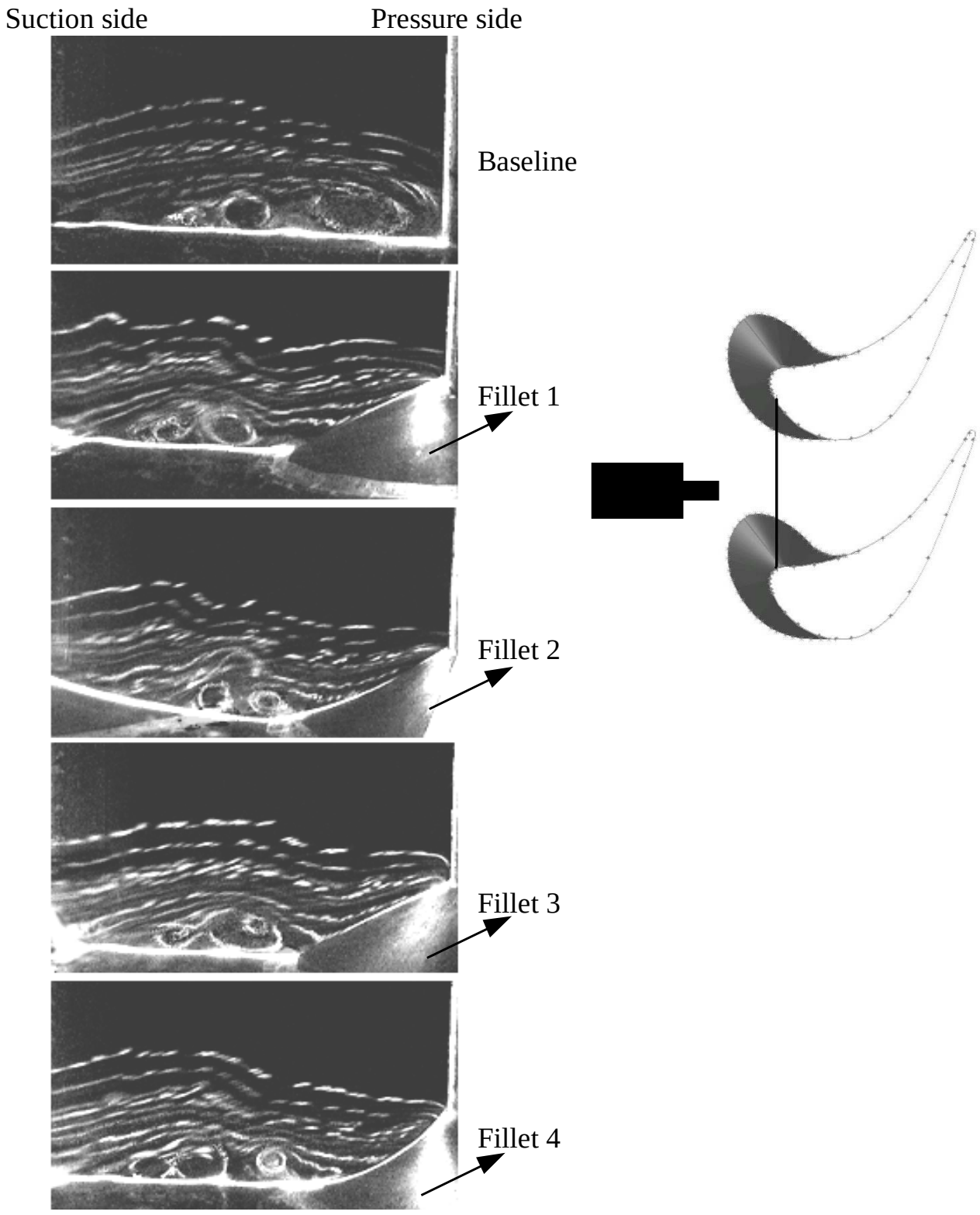

Figure 19: Flow Visualization Baseline / Fillets at X/Cax = 0.0 Plane

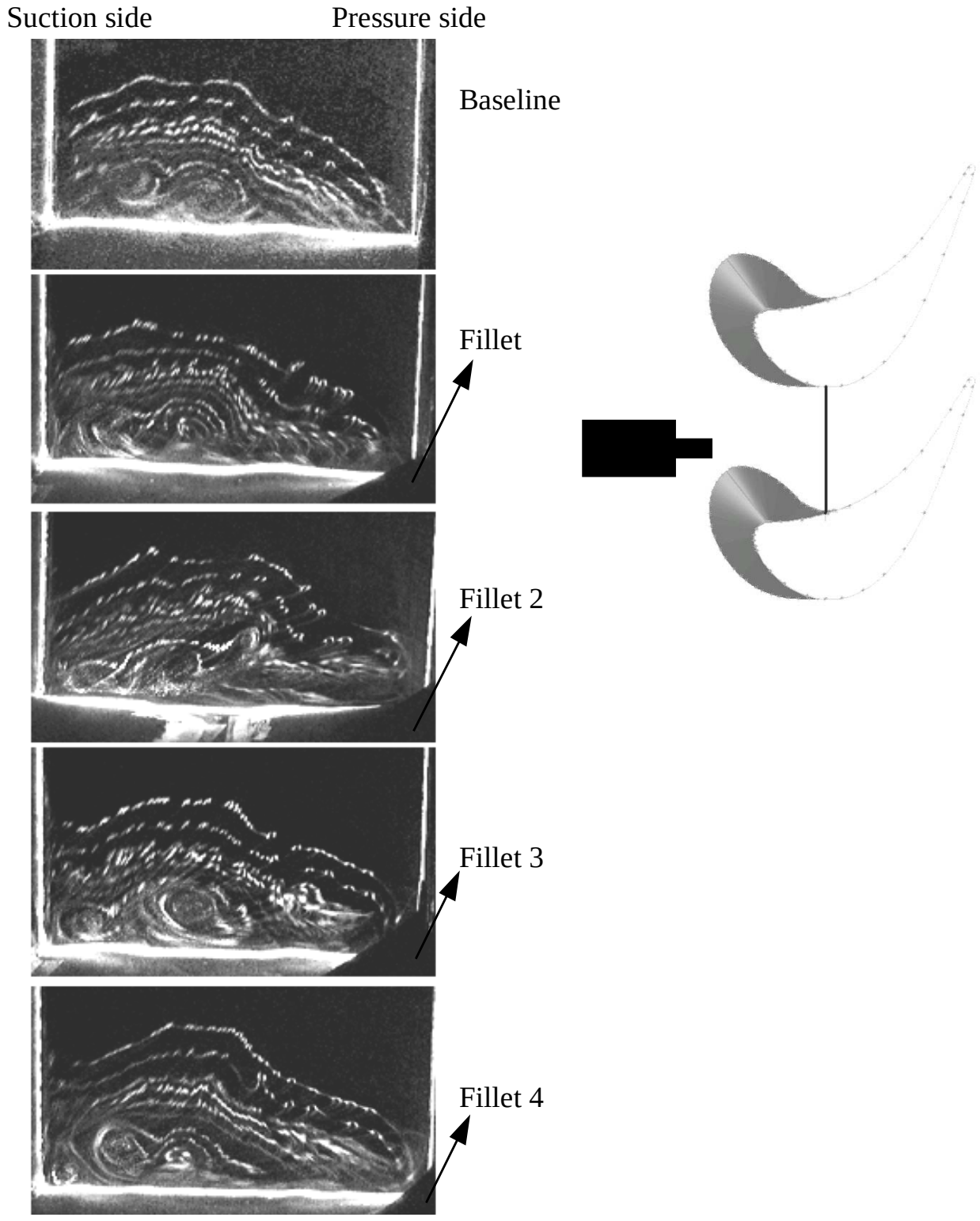

Figure 20: Flow Visualization Baseline / Fillets at X/Cax = 0.285 Plane

4.3.2 Time Averaged Secondary Flow Structures

Time-averaged flow structures are measured at an inlet velocity of 10.26 m/s using a five-hole probe and a hot wire anemometer. This section presents measurements of axial vorticity, mean pitchwise velocity, total pressure loss coefficients, streamwise turbulence intensity, and streamwise velocity. Figure 21 presents normalized axial vorticity and pitchwise velocity near the end-wall region in a pitchwise normal plane at X_G/C_{ax}= 0.215 for the baseline case. These measurements are taken with the five-hole probe. Location Z/P=0.0 (right side of the plot) corresponds to the pressure side while the left side of the plot corresponds to the suction side. Vorticity ($_x$) is computed from the velocity components W and V in this plane. The magnitudes of the normalized vorticity just above the end-wall region are high because of the passage vortex, primarily the pressure side leg of the horseshoe vortex. The negative W/U_{ref} magnitudes in figure 21 correspond to the cross flow from pressure to the suction side. It is clearly seen that just above the end-wall these magnitudes are positive, indicating a reverse flow region created by the passage vortex.

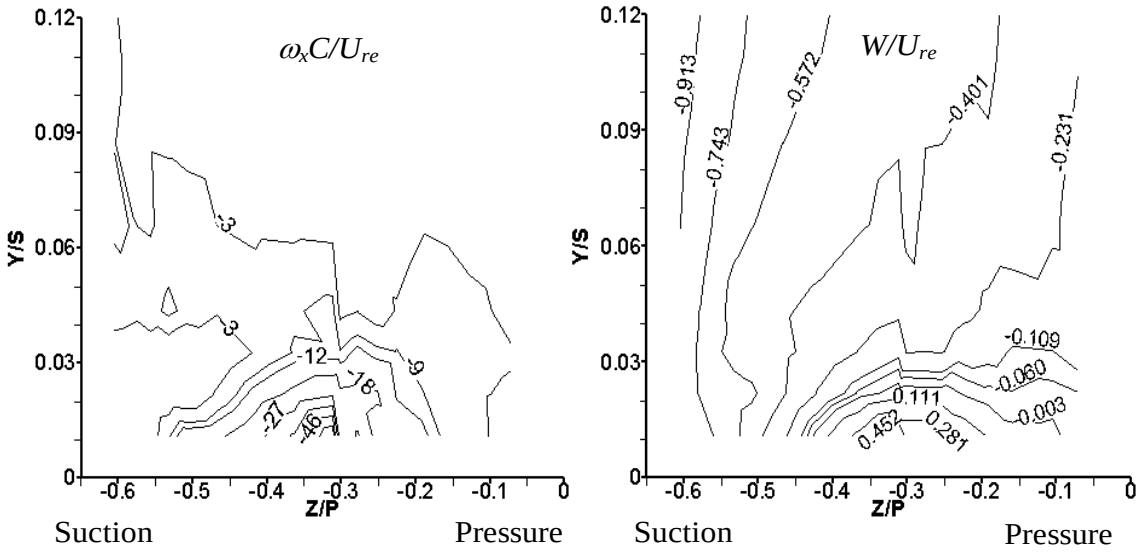

Figure 21: Baseline axial vorticity and pitchwise velocity at X/Cax=0.215

Figure 22 and figure 23 show the normalized axial vorticity and pitchwise velocity for the filleted cases at the same locations as in figure 21. The locations Z/P= 0.0 and -0.65 again correspond to the pressure and suction sides, respectively. No data is presented near the junction of the blade and endwall because of the presence of fillet profiles.

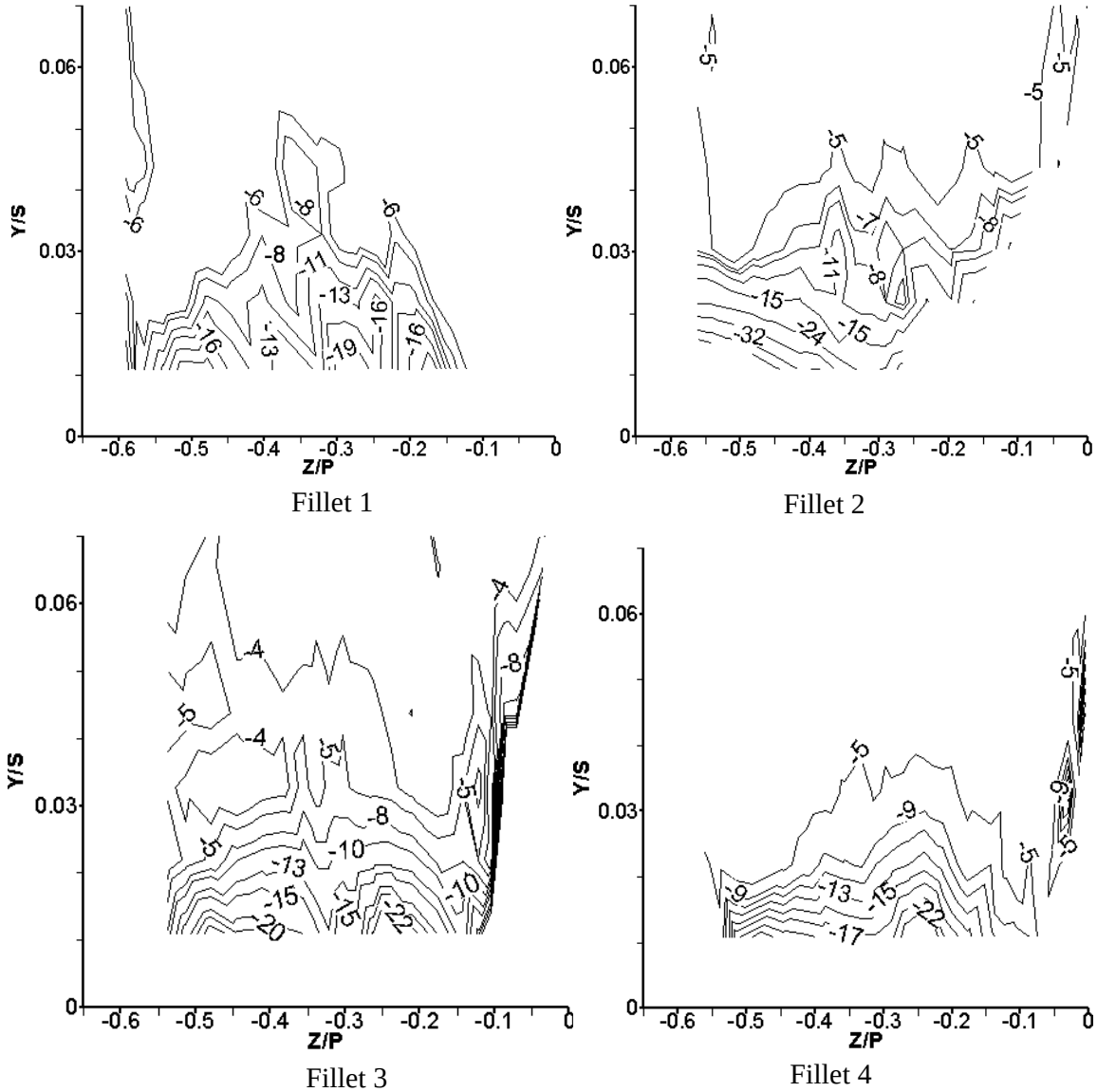

Fillet 1 Fillet 2

Fillet 3 Fillet 4

Figure 22: Fillet axial vorticity at X/Cax=0.215

When $_xC/U_{ref}$ magnitudes near the endwall in the region -0.45<Z/P<-0.15 and Y/S<0.03 are compared, the baseline values vary between -9 and –50. The data for filleted cases generally vary between -8 and -27. Thus, the fillets weaken the passage vortex structure at this location. Comparing the various fillet cases with each other, it can be seen that the magnitudes for fillet 2 are slightly higher than for other fillets. For fillets 1, 3, and 4, the peak vorticity magnitude exhibits a reduction of nearly 50% over the baseline case.

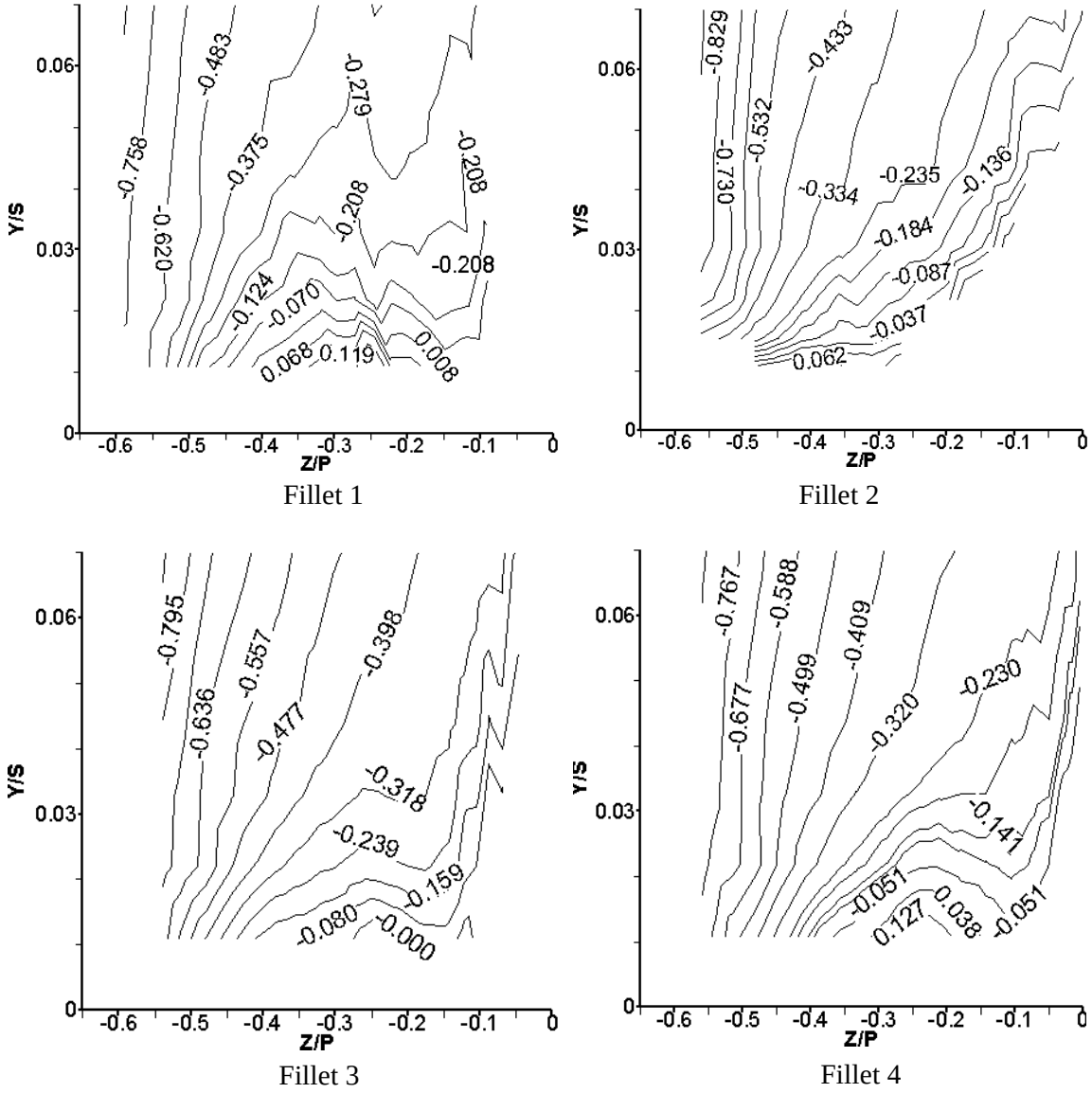

Fillet 1 Fillet 2

Fillet 3 Fillet 4

Figure 23: Fillet pitchwise velocity at X/Cax=0.215

The magnitudes of the pitchwise cross flow, W/U_{ref}, for the fillets in figure 23 are different from those for the baseline, especially near the endwall between Y/S=0.0 and 0.03. This confirms the observations made in the vorticity plots in figure 22. Here, the reverse flow region, with W/U_{ref} >0.0 near the end wall, is smaller with the fillets than for the baseline. Again, this indicates a weaker and smaller passage vortex structure with the fillets. The cross flow velocities from the pressure side to the suction side, with W/U_{ref} <0.0 in the near-wall region (Y/S<0.03), have higher magnitudes for the filleted cases than for the baseline. This is a consequence of the physical deflection of the flow by the fillets on the pressure side. These negative magnitudes are the highest for fillet 3 followed by fillet 4.

Figures 24 and 25 present total pressure loss coefficients for the baseline and filleted cases. This pitchwise normal plane at X_G/C_{ax}= 1.071 is located just downstream of the exit plane of the blade passage. The loss coefficient is computed from the five-hole probe total pressure measurements. In figure 24, the high magnitude of the loss coefficients in the suction side region between Z/P=0.05 to 0.25 and Y/S=0.15 to 0.30 is associated with the passage vortex. According to Wang et al. (1997), the passage vortex, which is dominated by the clockwise-rotating horseshoe leg from the pressure side, is strengthened by the cross-flow and the incoming boundary layer. The vortex lifts away from the endwall somewhere in the middle of the passage. Figure 25 shows that the center location of the passage vortex, identified by the eye of the contours associated with it. The filleted cases are about *0.02S* to *0.025S*, or *9.0* mm to *11.0* mm, above the center location for the baseline passage vortex. The stronger endwall crossflow in the filleted passage, see figures 21 and 23, lifts the passage vortex higher than the location of the

baseline passage vortex. Except for fillet 1, no reduction in the pressure loss coefficient is seen with the fillets at this location. Rather, for fillets 3 and 4, they are higher. Presumably a consequence of the stronger pitchwise velocity, W/U_{ref}, observed near the fillets on the pressure side for these two cases, see figure 23. Also, note in figures 24 and 25 the loss contour magnitudes are very high in the small region between *Z/P*=-0.06 and 0.06, and below *Y/S*=0.04. This is the endwall blade junction region immediately downstream of the blade trailing edge. The corner vortices are responsible for the high contour values in this region.

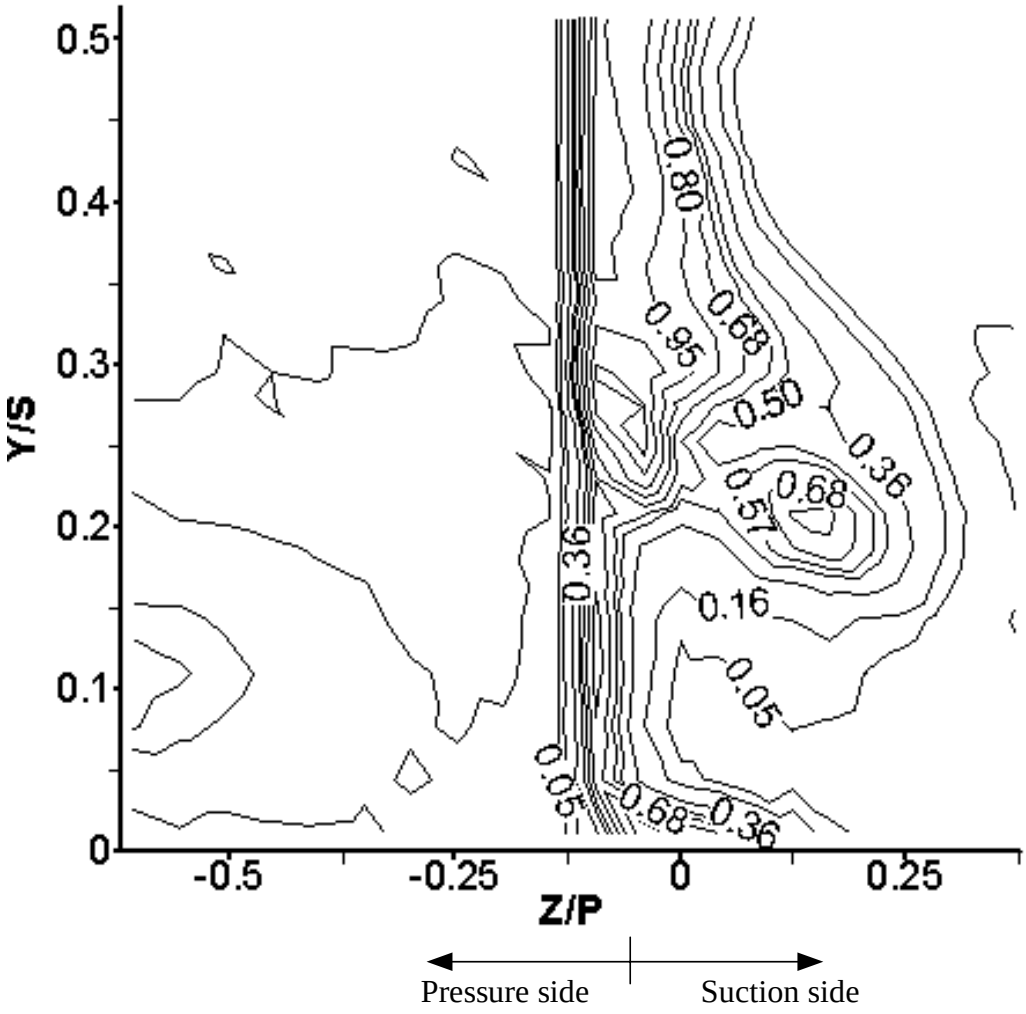

Figure 24: Baseline Total pressure loss coefficient at X/Cax=1.071

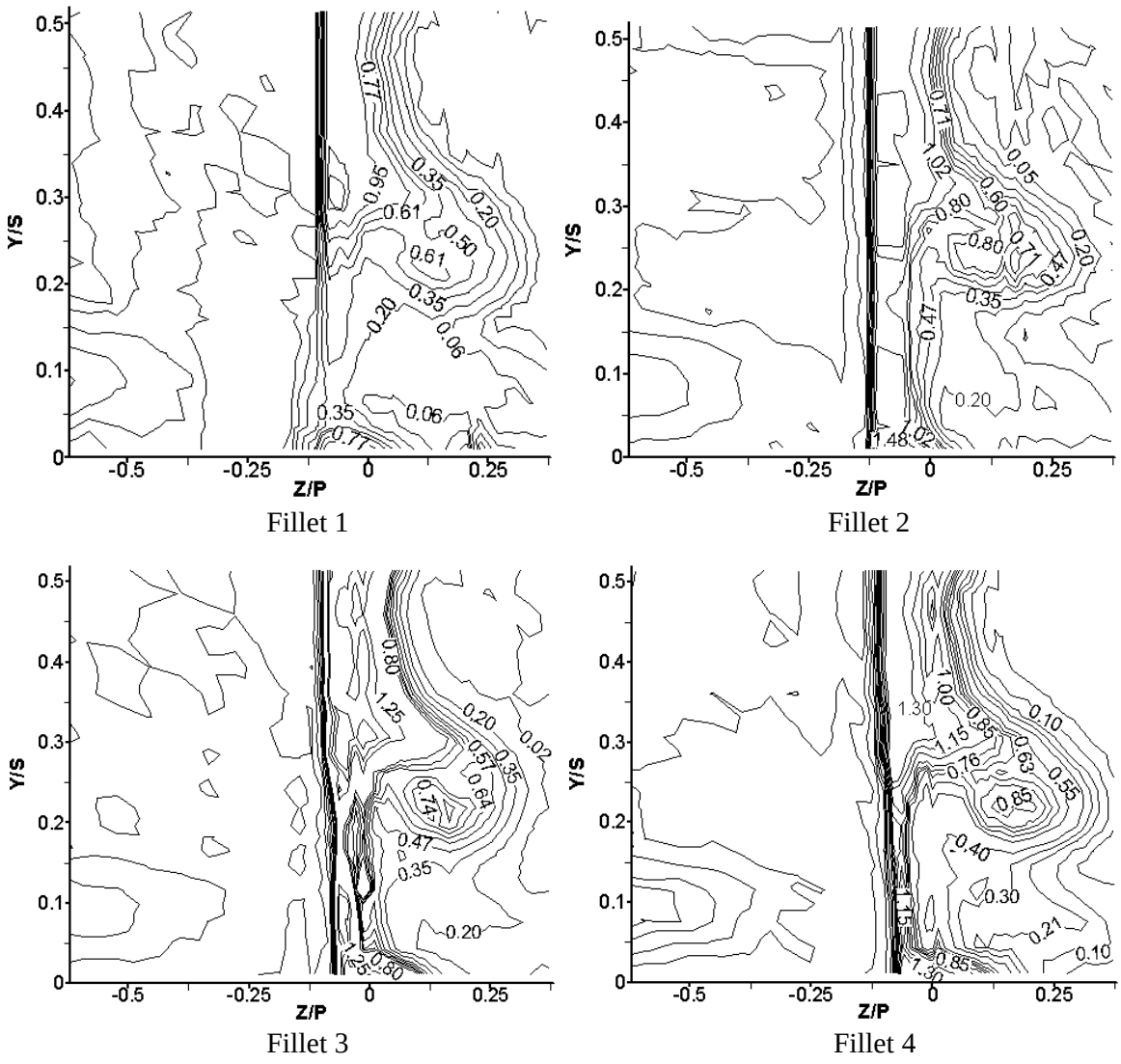

Figure 25: Fillet total pressure loss coefficient at X/Cax=1.071

The effects of the crossflow with the fillets are further evident in the streamwise turbulence intensity and streamwise normalized velocity distributions in figures 26 and 27, respectively. The data in these figures are presented along the pitchwise line located at the middle of the passage at different axial locations. In figure 26, turbulence intensity values from Y/S=0.0 to 0.10 and from X_G/C_{ax}=0.16 to 0.50 are high in general because of the boundary layer and passage vortex system. Further downstream at X_G/C_{ax}= 0.97 the high values lift up to the locations between Y/S=0.08 and Y/S=0.17 as the passage vortex

system lifts away from the endwall region. It can also be seen that in these high turbulence intensity regions the values are higher for the baseline than for the fillets. This indicates a more turbulent boundary layer for the baseline case than for the filleted cases. Kang et al. (2000) indicate that the fillets cause the endwall region flow to deviate less from the direction of mid-span streamlines, resulting in smaller pitchwise velocity. This is consistent with the weaker crossflow in the endwall region for the fillets than for the baseline, as seen earlier in figures 21 and 23. The lower turbulence intensity for the filleted cases is likely to have a beneficial impact on the end wall heat transfer.

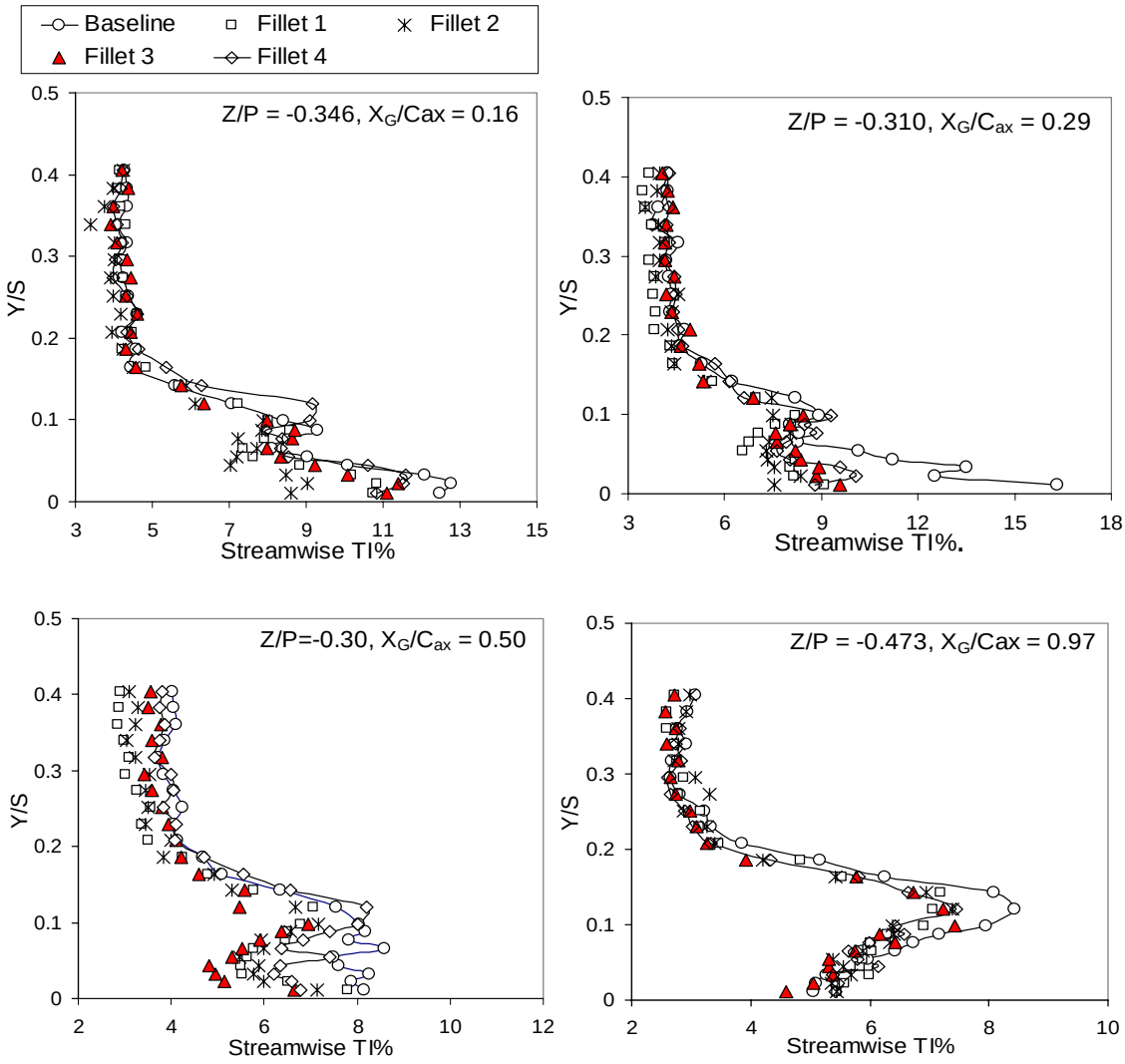

Figure 26: Baseline / Fillet streamwise turbulence intensity in passage center

Figure 27 shows the streamwise velocity distribution at two axial chord locations, X_G/C_{ax}=0.29 and 0.50. Boundary layer effects appear to extend up to 10-15% of the blade span. No significant effects of the fillets are seen since these effects are primarily confined to the end wall region and influence the secondary flows to a greater extent.

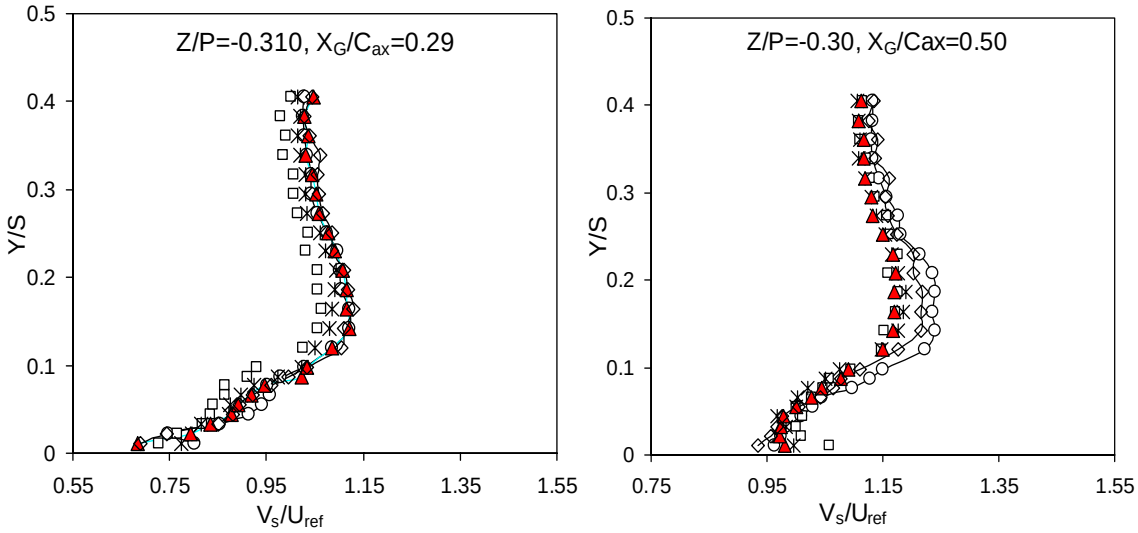

Figure 27: Baseline / Fillet streamwise velocity in passage center

4.4 Non-Axisymmetric Endwall Contour Results

This next section will review the experimental results for the non-asisymmetric contoured endwall (CE) and compare it to the baseline flat endwall results. The upstream section of the contoured endwall starts at the same height as the flat endwall. In order to compare the baseline to the contoured endwall the spanwise location of Y/S = 0.0 was kept at the same position. Thus traverse data taken near the suction side of the blade is presented below Y/S = 0.0.

The blade surface pressure coefficient was taken at Y/S = 0.33, as with the baseline case, and can be seen in figure 28. For the contoured endwall the C_p curve is shifted up, which can be explained by a slight cross sectional area change. Five-hole data also shows different static pressures near the blade surface. When the contoured endwall

was installed, reference static pressures changed in the blade channel. Because of the Cp definition, the curve is shifted up. Here, the contoured endwall does not affect the blade loading in the inviscid region because the curve is uniformly shifted up.

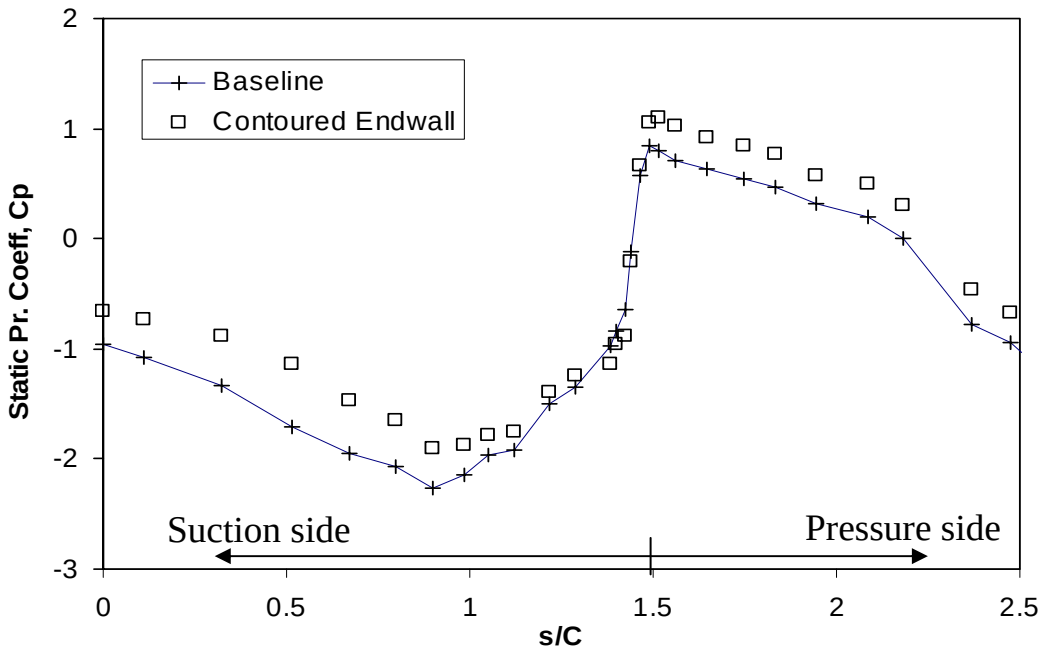

Figure 28: Baseline / Contoured Endwall Blade Surface Static Pressure Coefficient

The measured contoured endwall static pressure coefficient distribution can be seen in figure 29. A cross passage pressure gradient can be defined as the difference in endwall pressures between the pressure side and suction side along a pitchwise line. This cross passage pressure gradient is shown in figure 30. When compared to the baseline endwall, figure 15, a 47% decrease in the cross passage pressure gradient at X/Cax = 0.25 can be seen. In the latter half of the passage the endwall pressure gradient returns to similar levels to that of the baseline case. It should be noted that in the latter half of the passage he cross passage pressure gradient is better represented by lines approximately perpendicular to both the pressure and suction surface. Defined this way, the contoured endwall slightly reduces the cross passage pressure gradient in the latter half of the

passage. This overall decreased pressure gradient will reduce the crossflow and consequently the secondary flow losses.

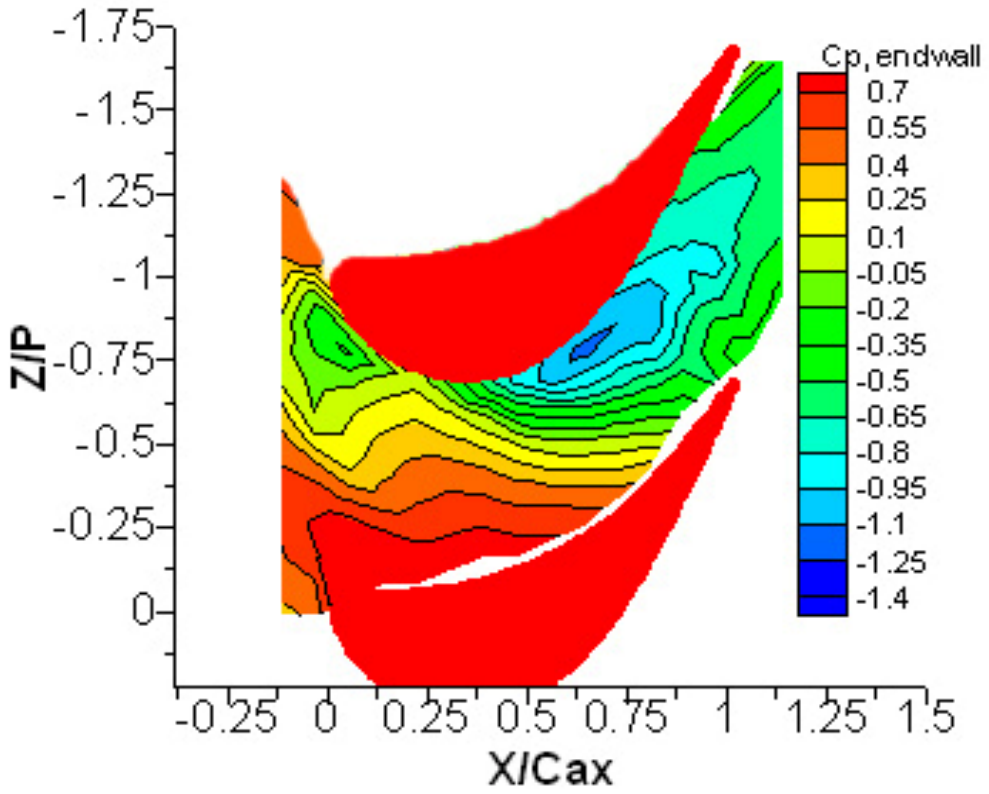

Figure 29: Contoured Endwall Static Pressure Coefficient

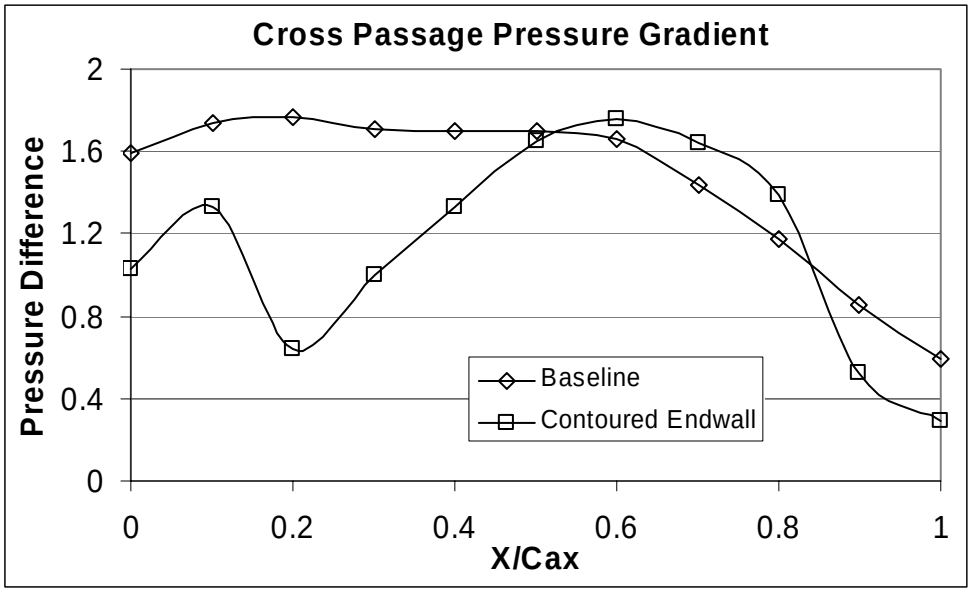

Figure 30: Baseline / Contoured Endwall Cross Passage Gradient

4.4.1 Instantaneous Secondary Flow Structures

Instantaneous images from smoke flow visualization are obtained in several planes. These planes can be seen in figure 7 and the images are presented in figures 32 - 36. The contoured endwall is shown on the left and the baseline endwall is shown on the right. The planes PS2, X/Cax = 0.17, and PS3, X/Cax = 0.285, are axial coordinate planes along pitchwise lines, while PS5 and PS6 are approximately perpendicular to the pressure surface and show structures originating from the pressure side more clearly. PS8 is near the throat region, and is approximately perpendicular to both the suction surface and pressure surface. SS3 is perpendicular to the upstream section of the suction surface. Structures originating on the suction side can be seen here more clearly. In each viewing plane the camera is positioned approximately perpendicular to the plane. The pressure side (PS) of the blade is on the right and the suction side (SS) is on the left of each image. These are usually indicated by a white vertical line on each side. The scale of each pair of images was kept the same so structure sizes can be directly compared.

An overhead view of the secondary structure flow paths for the baseline and contoured endwall can be seen in figure 31. These figures show the vortex paths and an arrow indicates the rotation on the top of the vortex. The position of the stagnation plane and PS3 plane is also shown. In regions where two vortexes travel side by side, they sometimes merge into one structure. All the vortex paths that come together in the latter half of the passage near the suction side form the passage vortex system. One or more vortexes may exist in this passage vortex system and can rotate in opposite directions. The following flow visualization planes will explain these flow paths and show the individual vortex structures.

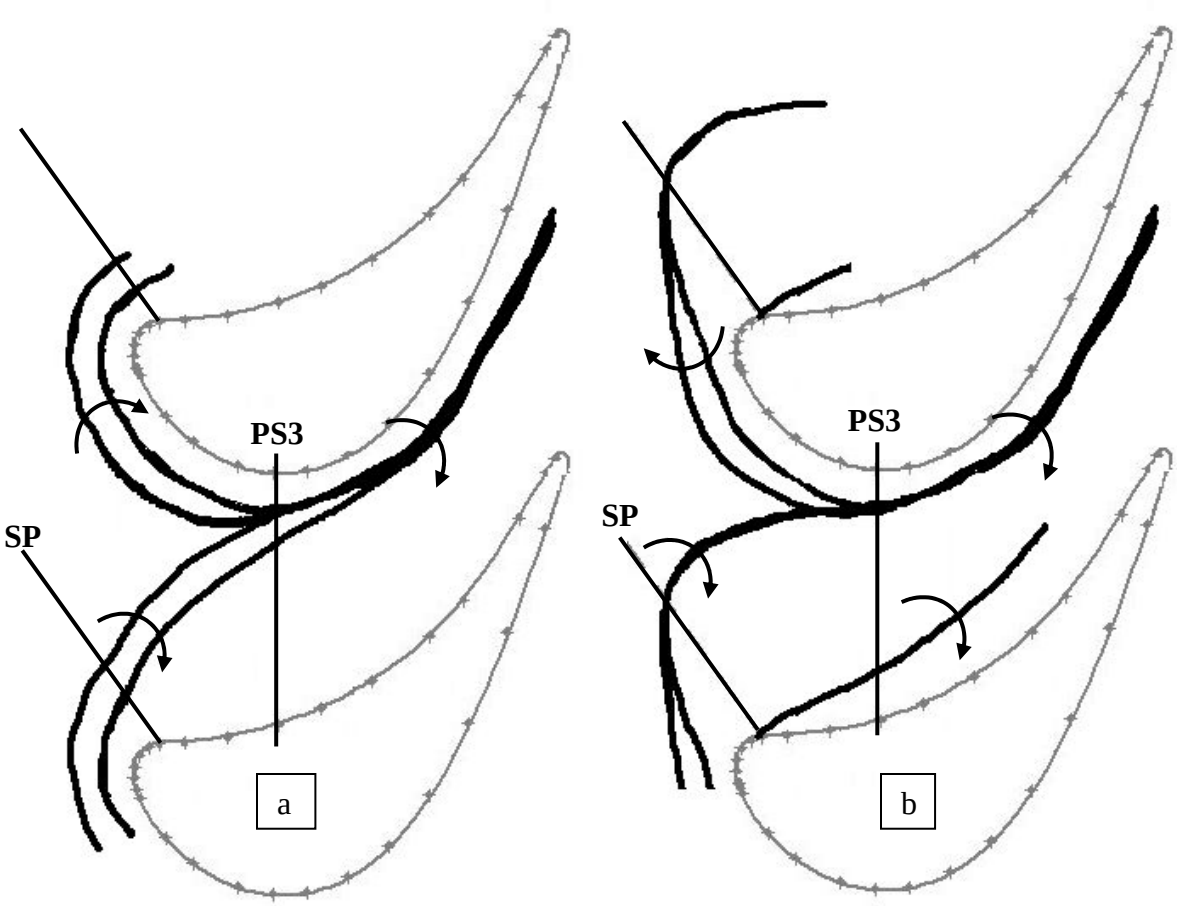

Figure 31: Secondary Flow Paths Observed from Flow Visualization (a) Baseline, (b) Contoured Endwall

Figure 32 presents the flow visualization pattern along the stagnation plane (SP). The baseline case shows a distinct horseshoe vortex system. A horseshoe vortex cannot be seen in the stagnation plan of the contoured endwall. A thick bright white line is seen on the contoured endwall because the surface has a downward slope which exaggerates the light plane thickness. The horseshoe vortex is likely too small to entrain smoke. Thus, flow structure comparison will begin slightly downstream. Figure 33 (a) shows the PS2 plane at X/Cax = 0.17. In the baseline image two large vortex structures originating from the pressure side leg of the horseshoe vortex can easily be seen. These structures periodically merge together and form one vortex and their paths are shown in figure 31.

For the contoured endwall these structures are reduced dramatically in size and are separated far apart. One remains close to the pressure side and the other is very near the suction side. Since neither structure was observed in the stagnation plane it was questionable as to whether these structures were part of the horseshoe vortex system.

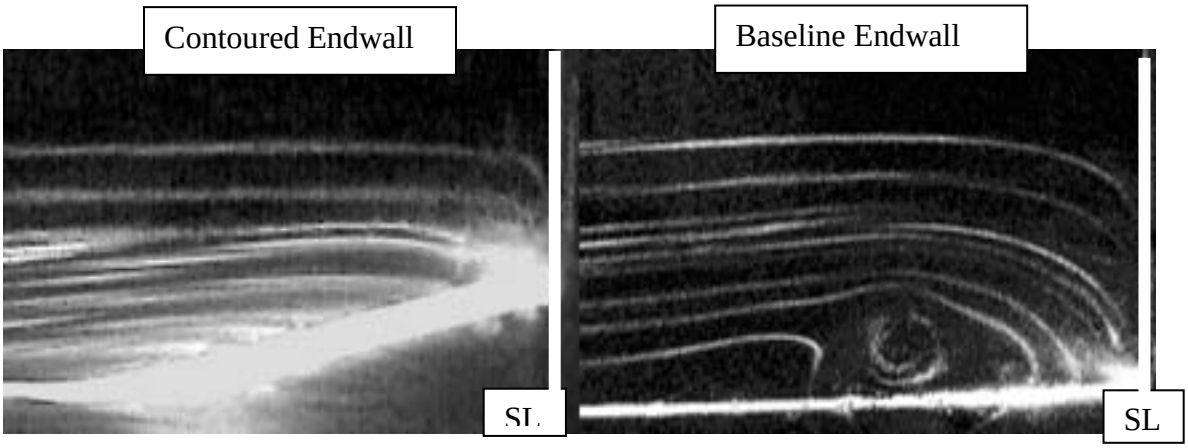

Figure 32: CE / Base Stagnation Plane Flow Visualization

To understand the origin of these structures smoke traces were observed across the entire channel without the use of a light plane. Small traces of smoke originating far upstream of the blade in the stagnation plane could be seen on the endwall traveling nearly perpendicular to the main flow. The traces then traveled toward the suction side to the same location as the vortex near the suction side in PS2, figure 33 (a). This vortex is the pressure side leg of the horseshoe vortex near the suction side, PHVS. Its path is shown in figure 31 to be further upstream of the horseshoe in the baseline case. This side of the contoured endwall acts like a large fillet. The horseshoe vortex was displaced further upstream by the contoured endwall than by any of the fillets. It was displaced upstream to the point where the flat endwall transitions to a contoured endwall. This vortex also remained too small to entrain smoke in an observable circulation until it entered the low pressure trough on the suction side. As with the fillets the boundary layer fluid is

displaced away from the stagnation plane effectively reducing the size of the horseshoe vortex. An induced pressure gradient along the contoured endwall to the blade stagnation line also counters the adverse pressure gradient that drives the horseshoe vortex. The vortex near the pressure side in PS2 of figure 33 (a) originates in the stagnation corner of the endwall and blade and is part of the horseshoe vortex system. It is referred to as PHVP.

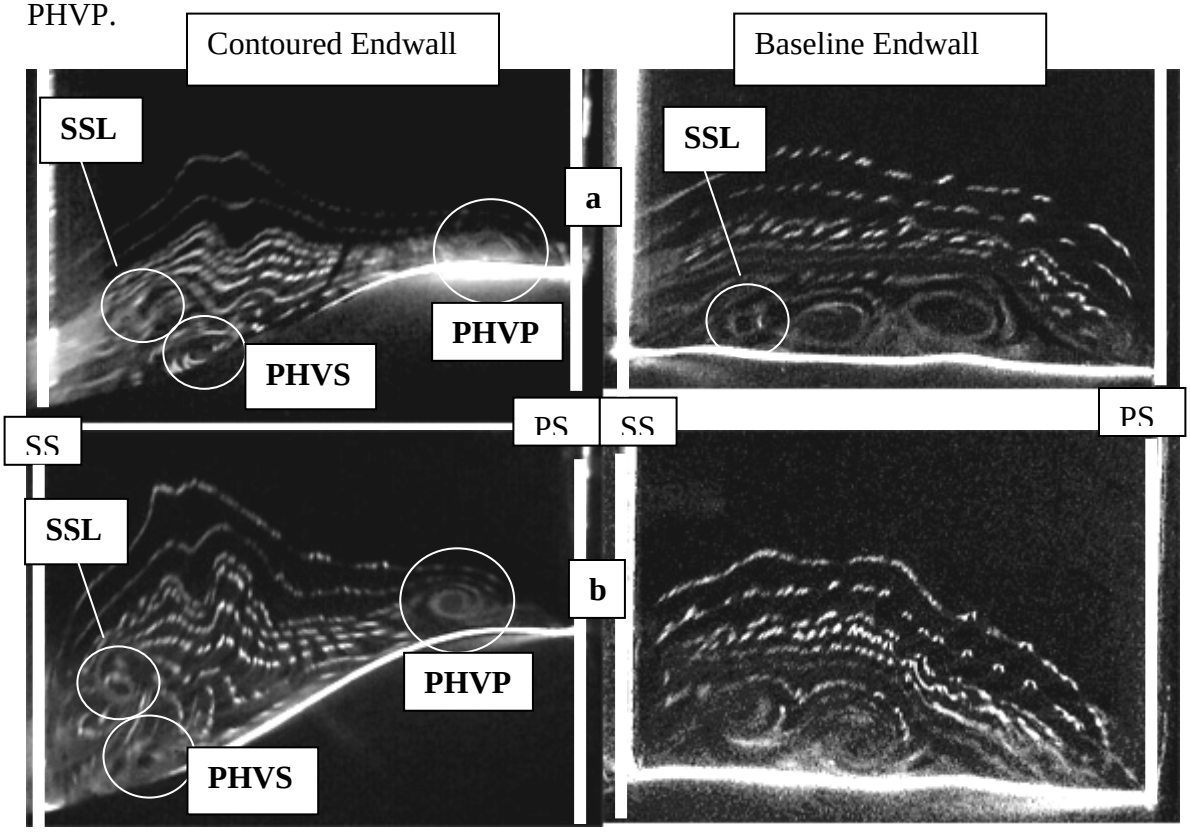

Figure 33: CE / Base Pitchwise Plane Flow Visualization at (a) PS2 X/Cax = 0.17, (b) PS3 X/Cax = 0.285

It is shown to start at the stagnation point of figure 31 and proceed along the pressure surface. It is too small to be observed in the stagnation plane because the boundary layer is very thin there. By X/Cax = 0.17 it grows to an observable size. Near the suction side of the baseline case a small vortex can be seen. This is the suction side leg (SSL) of the horseshoe vortex. It can also be seen with the contoured endwall just above and to the left

of the far pressure side leg of the horseshoe vortex. It is severely blurred by smoke upstream and downstream of the viewing plane, but is more comparable in size to the baseline case. It also has a larger relative size compared to its neighboring pressure side leg. As indicated by Saucer et al. (2000) a larger suction side leg of the horseshoe vortex may reduce the strength of the passage vortex.

In the PS5 plane the pressure side legs of the horseshoe can be seen in figure 34 (a). This plane begins at X/Cax = 0.17 on the pressure side and is perpendicular to the pressure surface. Two large vortex structures can be seen near the center of the passage for the baseline case. These again periodically merge into one. For the contoured endwall, a much smaller structure can be seen near the pressure surface. The other structure, which moves quickly toward the suction surface, is just beginning to become large enough to entrap smoke. Its presence is indicated by the small bump in the smoke line nearest the endwall on the left side of the image. Figure 31 shows this vortex to be much closer to the suction surface in this plane.

Images in the PS3 plane at X/Cax = 0.285 are shown in figure 33 (b). The two large pressure side legs of the horseshoe vortex in the baseline case have moved closer to the suction side. These structures are now considered the passage vortex system and periodically merge into one. They are shown in figure 31 to be two separate structures in this plane. One vortex still remains near the pressure side for the contoured endwall, and its path is shown to stay near the pressure surface in figure 31. One reason this vortex has remained near the pressure side is that the crossflow has been reduced. The contoured endwall was designed to reduce the pressure gradient from pressure side to suction side. The structure just above the contoured endwall near the suction side is the pressure side

leg of the horseshoe vortex and rotates in a clockwise direction. Another vortex exists just above and to the left of this pressure side leg. It is the suction side leg of the horseshoe vortex and rotates in a counterclockwise direction. Their paths merge in figure 31 by this plane because one is on top of the other. The suction side leg in the baseline case has merged with the passage vortex or is too weak to be seen.

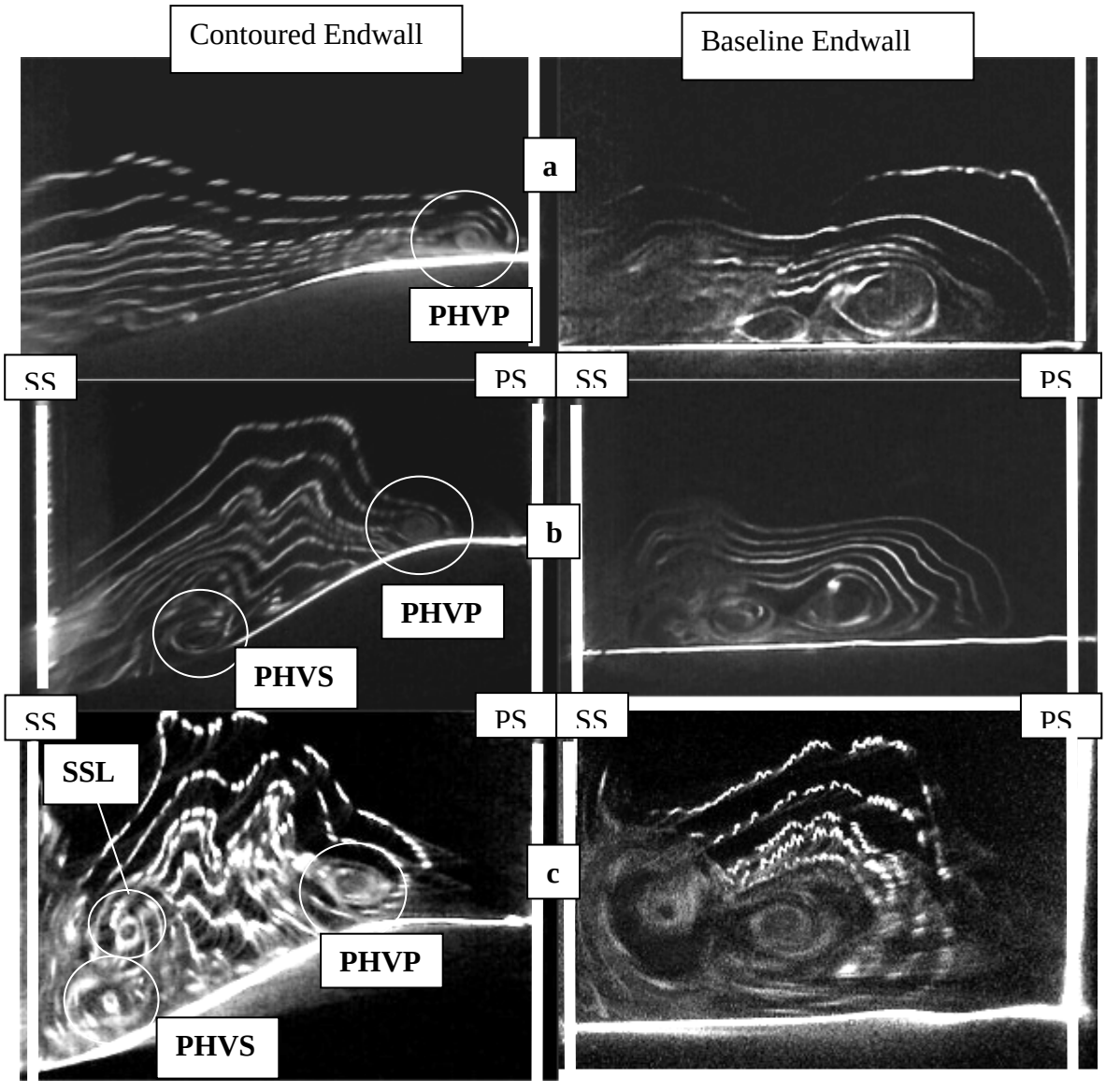

Figure 34: CE / Base Perpendicular to Pressure Surface Flow Visualization at (a) PS5, (b) PS6, (c) PS8

PS6 begins at X/Cax = 0.285 on the pressure side but is also perpendicular to the pressure surface. Figure 34 (b) shows the secondary flows in this plane. The two large pressure side legs of the horseshoe vortex can again easily be seen in the baseline case. The contoured endwall exhibits much smaller structures and still keeps the two pressure side legs separated far apart. This plane simply repeats what has been shown in PS2 and PS3, indicating that the crossflow has been reduced.

PS8 is near the throat region and approximately perpendicular to both the pressure and suction surface. Figure 34 (c) shows the images captured here. The baseline case shows two large structures of the passage vortex system, which again periodically merge into one. Figure 31 shows one path in this plane which is the passage vortex system and may include more than one vortex. The contoured endwall again shows one pressure side leg structure near the pressure side as shown in the paths of figure 31. This is further proof that the contoured endwall reduces the crossflow. Near the suction surface the bottom vortex is from the pressure side and rotates in the clockwise direction. The vortex on top is from the suction side and rotates in the counterclockwise direction.

The suction side leg of the horseshoe vortex on the contoured endwall is next observed to better understand its origins. US1 is a plane perpendicular to the stagnation plane and upstream of the leading edge. An image taken here for the contoured endwall case can be seen in figure 35 (a). The bottom white line shows the endwall and the beginning of the trough that leads to the suction side. A vortex structure can be seen here in the trough, which is the suction side leg of the horseshoe vortex. US2 is parallel plane to US1 but downstream and closer to the leading edge of the blade. Figure 35 (b) shows an image taken here with the contoured endwall. Now, two vortexes can be seen.

Contoured endwall secondary flow paths in figure 31 show this vortex to start as one, travel almost parallel to the stagnation plane, and split into two structures.

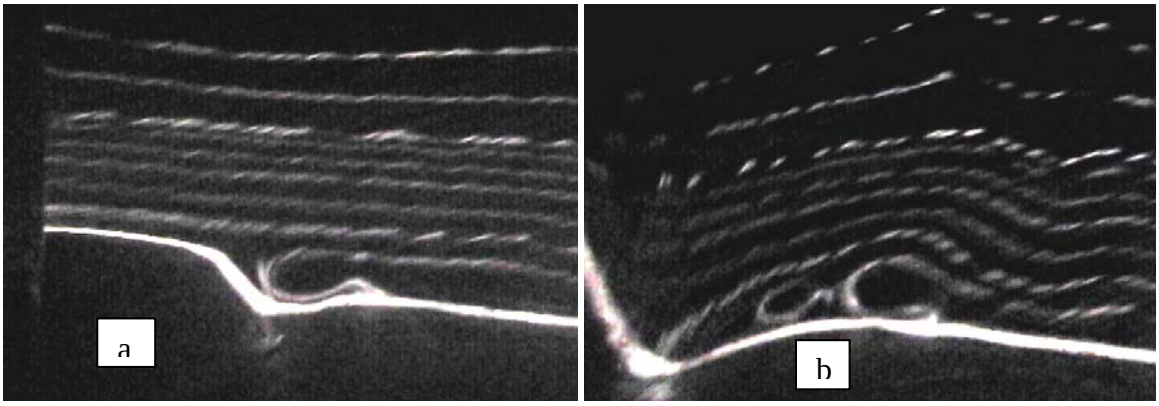

Figure 35: Contoured Endwall Flow Visualization at (a) US1, (b) US2

SS3 starts at X/Cax = 0.08 on the suction side and is perpendicular to the suction surface. Figure 36 shows images taken here and allows the suction side legs to be further tracked. Both the baseline and contoured endwall show two vortex structures of comparable size. Two paths are shown in this plane for both cases in figure 31. The structures in the contoured endwall move down the trough and along the suction side. These suction side legs of the horseshoe vortex next appear at X/Cax = 0.17, PS2, but only one is observable from now on. Downstream of this plane they either merge together or one is consumed by the passage vortex.

These flow visualization experiments are performed at very low Reynolds numbers. It is believed that the secondary flows might behave differently at higher Reynolds numbers. Five hole data, which will be shown later, does not support that the pressure side leg of the horseshoe vortex stays near the pressure surface. It is believed to merge towards the suction surface at higher Reynolds numbers. Viewing these images on a comparative basis shows that the contoured endwall reduces the crossflow and presumably reduces the cross passage pressure gradient. The horseshoe vortex, pressure

side legs, and passage vortex are also dramatically reduced in size. The stronger suction side leg will hopefully reduce the strength of the passage vortex. The overall reduction in secondary flow size and strength will reduce pressure losses and endwall heat transfer coefficients. One clear advantage can be seen with the contoured endwall flow paths in figure 31. The horseshoe vortex forms much further upstream of the blades stagnation point than for the baseline case. This region just upstream of the blades stagnation point is traditionally a high heat transfer region because of the horseshoe. Moving the horseshoe further upstream will reduce the heat transfer in this region also.

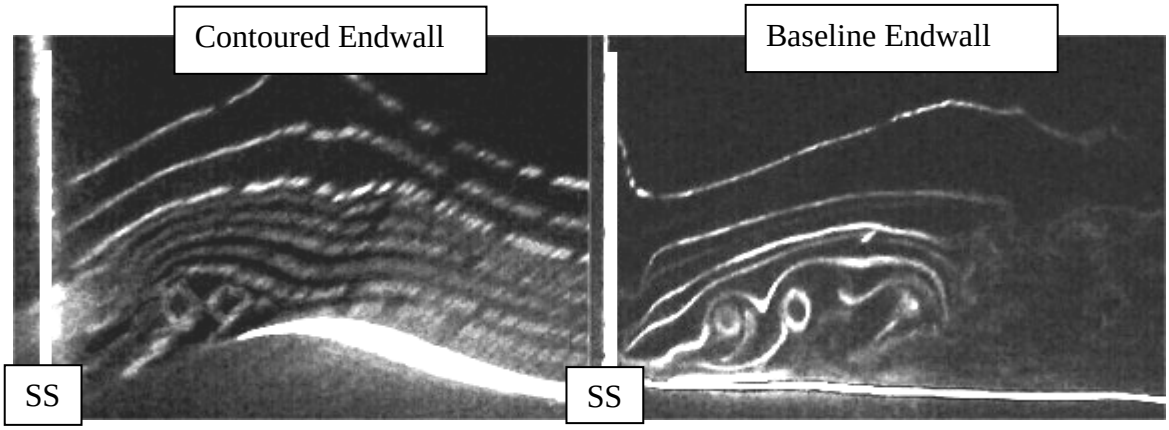

Figure 36: CE / Base Perpendicular to Suction Surface Flow Visualization at SS3

4.4.2 Time Averaged Secondary Flow Structures

Time-averaged flow structures are measured using a five-hole probe and a hot wire anemometer. This section presents measurements of total pressure loss coefficients, mean pitchwise velocity, axial vorticity, offset parallel plane vectors, streamwise turbulence intensity, and air temperature measurements for the baseline and contoured endwall (CE). Due to a finite probe tip length five-hole and hot wire measurements are taken in planes slightly upstream of the slot locations and are shown in figure 37 with pitchwise Z/P position markers.

Figure 38 shows the pressure losses at X/Cax = 0.05 for the baseline case. Five hole data was not available for the contoured endwall in this case. The left side of the figure is near the suction side (Z/P = -0.8) and the right side is closer to the pressure side (Z/P = 0.0). A high pressure loss region exists on the endwall near the suction side. This indicates the presence of the suction side leg of the horseshoe vortex.

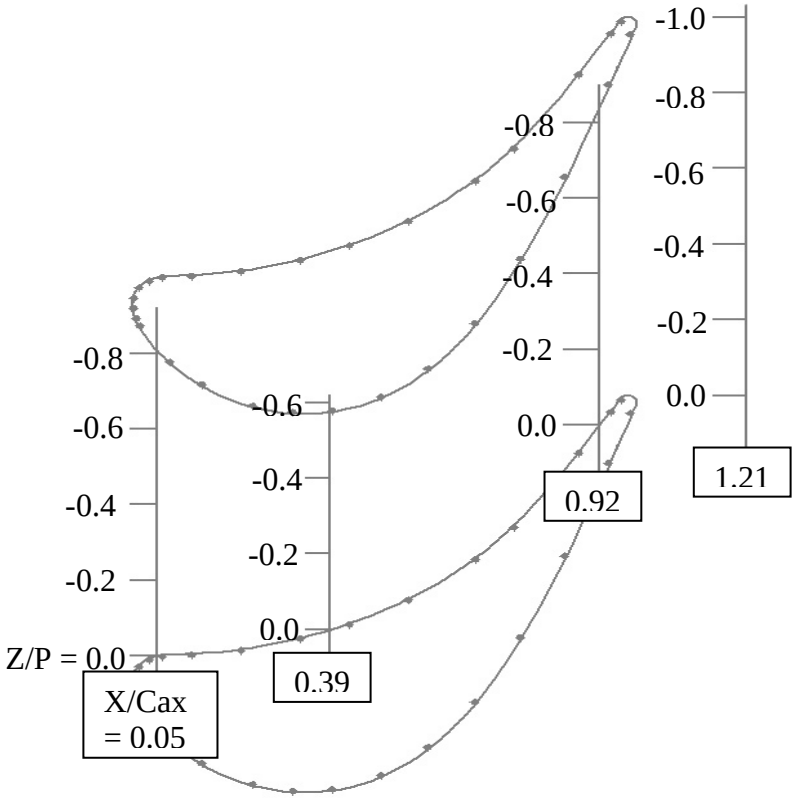

Figure 37: 5-Hole Probe Tip locations with Z/P markers

Figure 39 shows the velocities in the pitchwise direction. A vortex is indicated by the curving of the iso-velocity lines towards the suction surface near the endwall. Lower velocity spikes at Y/S = 0.04 near the suction surface on the baseline endwall indicate the upper half of the counterclockwise rotating suction side leg of the horseshoe vortex. Near zero values near the pressure surface on the baseline endwall indicate the upper half of the clockwise rotating pressure side leg of the horseshoe vortex.

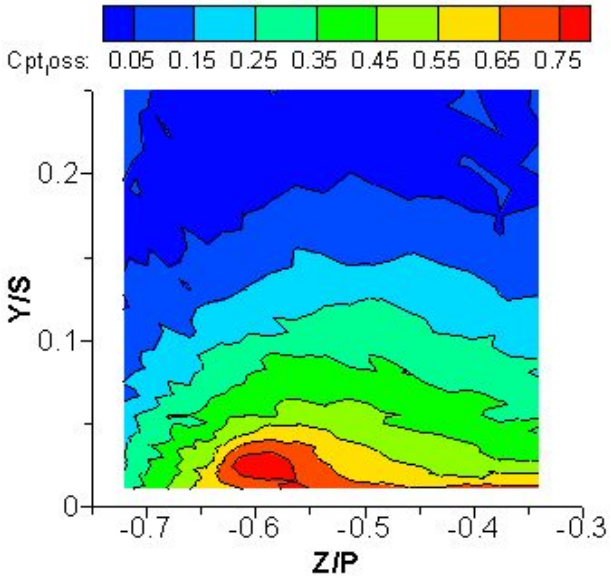

Figure 38: Pressure loss coefficient at X/Cax = 0.05 for baseline

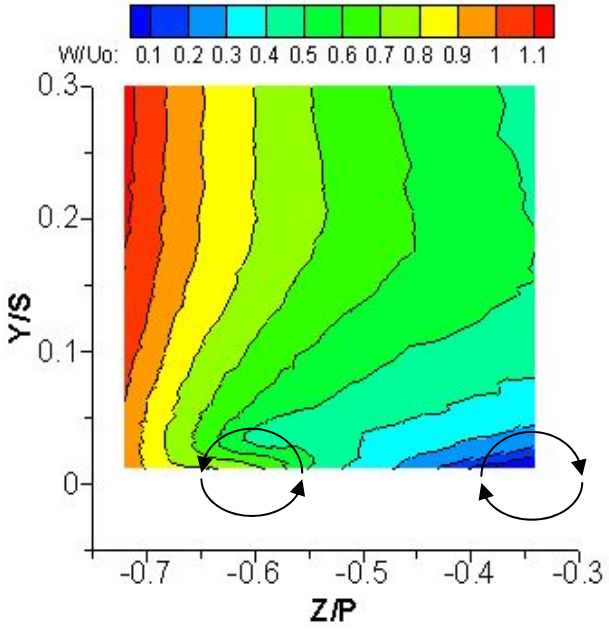

Figure 39: Pitchwise Velocities at X/Cax = 0.05 for baseline

Vorticity is shown in figure 40 at X/Cax = 0.05. Spline curves are used to fit the spanwise and pitchwise velocities at each pitchwise and spanwise location, respectively. Derivatives are taken and the vorticity is calculated as follows.

Vorticity: $\omega_x = \frac{\partial w}{\partial y} - \frac{\partial v}{\partial z}$

The high negative values indicate the strength and position of the suction side leg of the horseshoe vortex. There exists a region of positive vorticity closer to the pressure surface. This indicates the presence of the pressure side leg of the horseshoe vortex.

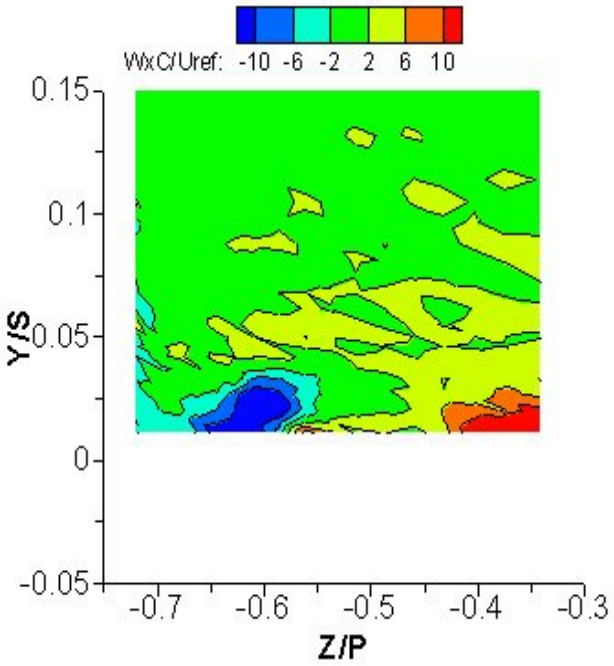

Figure 40: Voricity at X/Cax = 0.05 for baseline

Offset parallel plane velocity vectors can be seen in figure 41. These vectors lie in planes, which are perpendicular to the approximate inviscid streamwise direction. Each line of vectors at a specific pitch location lie in a parallel but slightly upstream or downstream plane of the neighboring line of vectors. These planes are approximately perpendicular to the vortex axis of rotation and thus show the vortex center, size, and rotation very clearly. Vector direction indicates yaw and pitch angles and their length represents magnitude. The baseline case shows a counterclockwise rotating suction side leg of the horseshoe vortex at Z/P = -0.62 and Y/S = 0.025. This corresponds to the negative vorticity region in figure 40 and the high pressure loss region in figure 38. Figure 42 shows the turbulence intensities at X/Cax = 0.10 in the average inviscid streamwise direction at

X/Cax = 0.05. Hot wire measurements are always taken approximately five millimeters above the endwall due to probe safety. When these hot wire measurements were taken, the objective was to measure near wall turbulence levels in the center of the passage. This would give an indication of heat transfer on the endwall. Thus, turbulence intensities were not measured over the entire vortex region. High turbulence intensities can be seen near the endwall for the baseline case. This indicates higher heat transfer regions. The contoured endwall presents approximately 35% lower peak turbulence intensities.

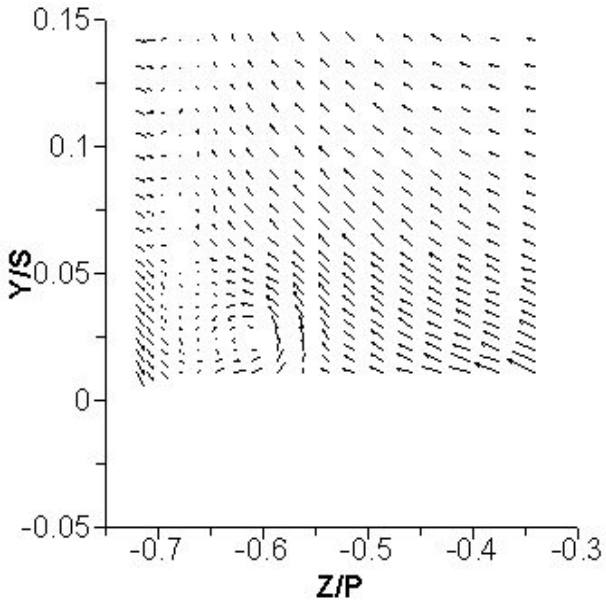

Figure 41: Offset Parallel Plane Vectors at X/Cax = 0.05 for baseline

A non-dimensional temperature profile for the contoured endwall at X/Cax = 0.16 can be seen in figure 43. Here the endwall was heated and allowed to reach a steady state temperature. The effect of the suction side leg of the horseshoe vortex can be seen. The counterclockwise rotating vortex is convecting hot air from the endwall at –0.55 < Z/P < -0.50 up to the mainstream flow. Colder fluid is being moved down towards the endwall at –0.65 < Z/P < -0.60.

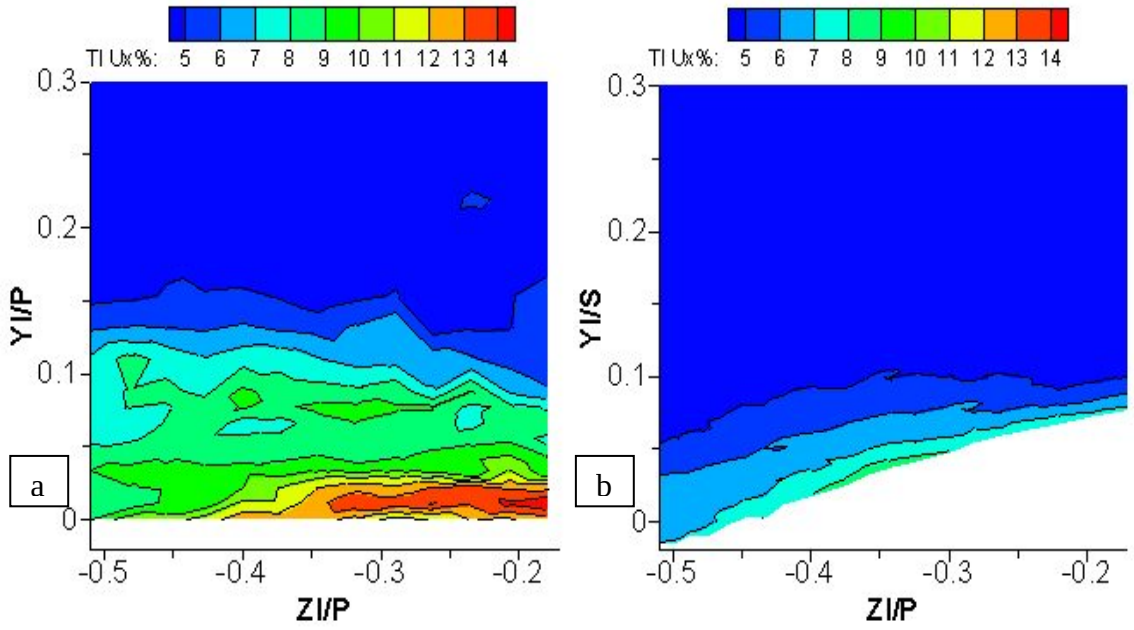

Figure 42: Streamwise Turbulence Intensties at X/Cax = 0.10 (a) baseline, (b) CE

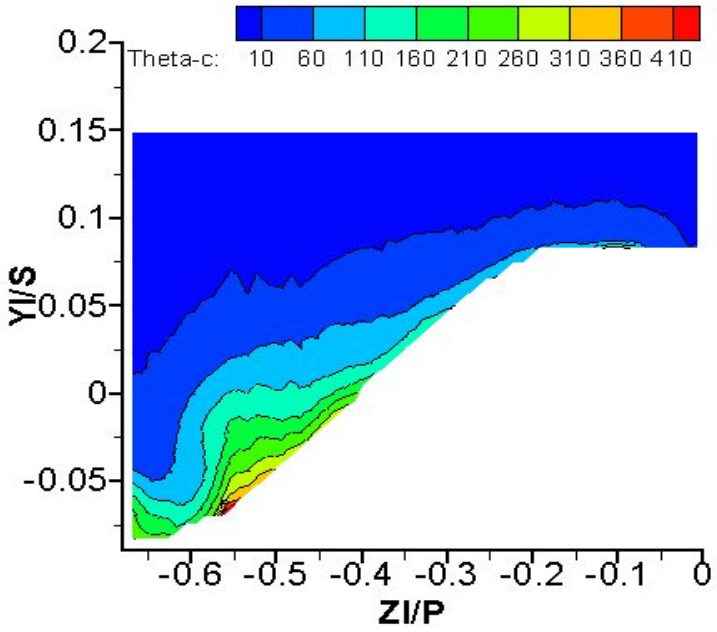

Figure 43: Non-dimensional Temperature at X/Cax = 0.16 for Contoured Endwall

Pressure loss contours at X/Cax = 0.39 can be seen in figure 44. All figures are presented with the blade pressure surface on the right side of the figure and the suction surface on the left. Both the baseline and contoured endwall show a well defined pressure loss core on the endwall near the suction side. This loss core is created by the passage

vortex, which rotates in a clockwise direction. The peak core pressure losses are 23% less for the contoured endwall. This indicates that the contoured endwall reduces the secondary flow strength. The flow field also indicates the presence of a clockwise vortex.

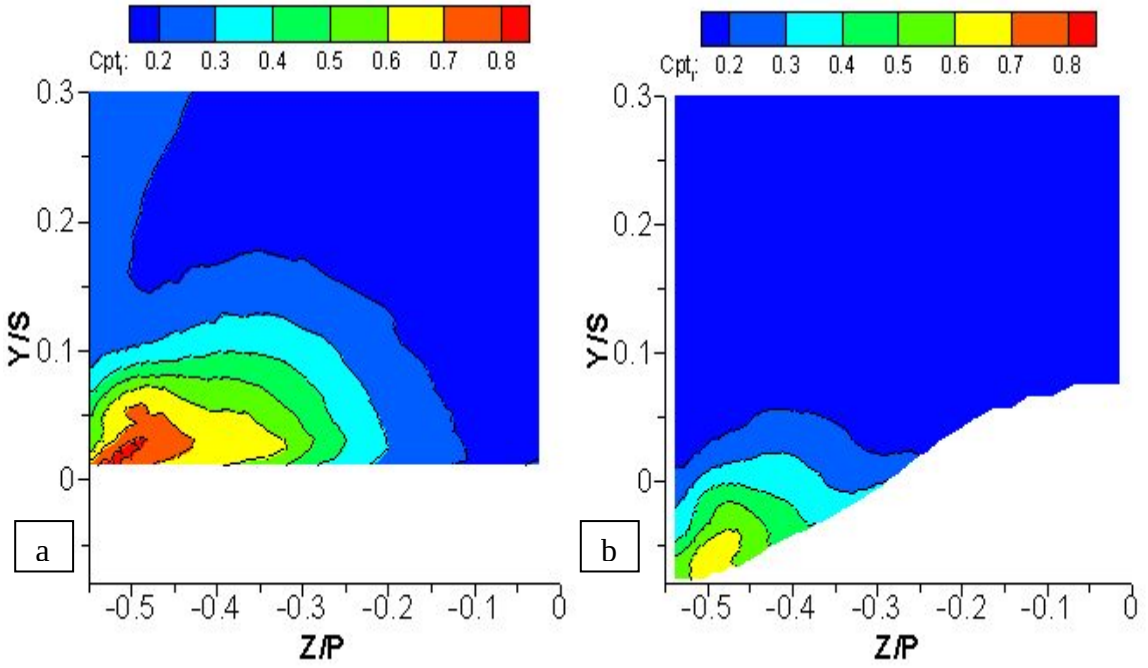

Figure 44: Pressure loss coefficient at X/Cax = 0.39 (a) baseline, (b) CE

Figure 45 shows pitchwise velocities. Higher velocities on the endwall are directed towards the suction surface and are indicative of the crossflow. It can be seen that the baseline case has a thicker and stronger crossflow region. The contoured endwall reduces the crossflow because the cross passage pressure gradient has been reduced. In the suction surface endwall corner for the baseline at Z/P = -0.475 and Y/S = 0.05 a small region of low velocity flow can be seen. This is the top half of the clockwise rotating passage vortex. A similar region exists in the suction surface contour endwall corner. Vorticity for X/Cax = 0.39 is shown in figure 46. A large positive vorticity region for the baseline near the endwall exists. This represents the clockwise rotating passage vortex. Note that this axial plane is not perpendicular to the vortex axis. The contoured endwall

shows much weaker vorticity levels and a smaller positive vorticity region, indicating a weaker passage vortex. A small negative vorticity region exists above and to the left of the passage vortex in both cases. This represents a weak suction side leg of the horseshoe vortex. This structure is comparable in size and strengthfor both cases, but for the contoured endwall it is larger relative to the passage vortex. Wang et al. (1997) has shown this suction side leg to stay separated from the passage vortex. The contoured endwall may produce a stronger suction side leg which would further reduce the strength of the passage vortex.

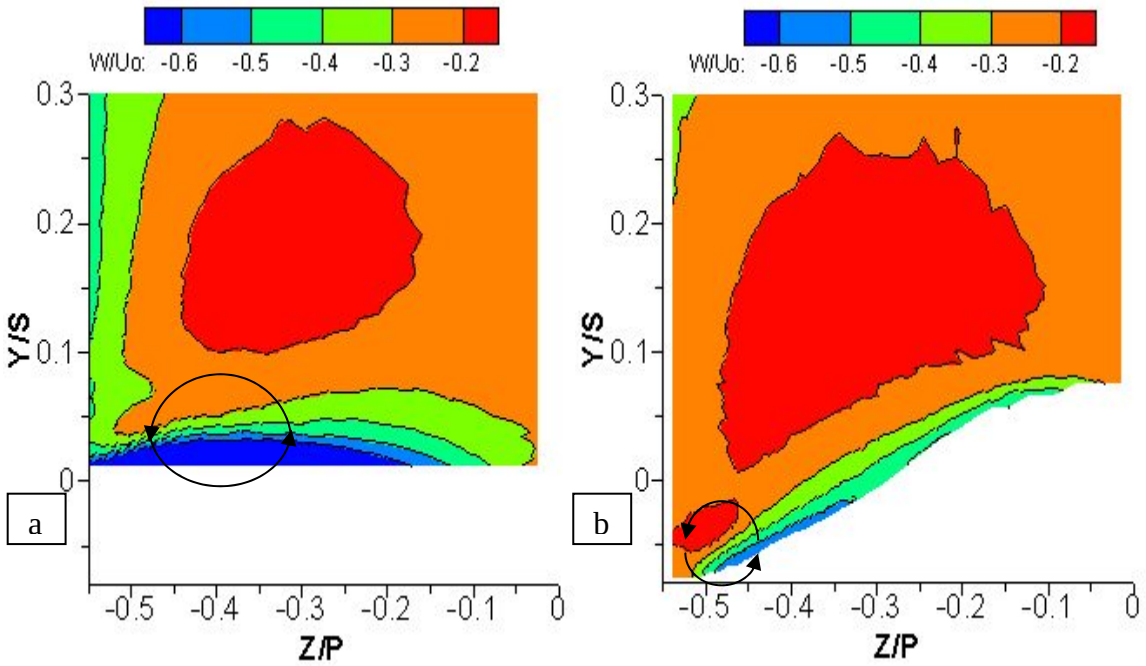

Figure 45: Pitchwise velocity at X/Cax = 0.39 (a) baseline, (b) CE

Vector plots are shown in figure 47 and are in offset parallel planes as explained previously. The baseline case shows the clockwise rotating passage vortex at Z/P = -0.36 and Y/S = 0.03. The contoured endwall shows a smaller and weaker vortex centered at Z/P = -0.45 and Y/S = -0.06. Figure 48 shows turbulence intensities at X/Cax = 0.45 are much weaker on the contoured endwall. Peak values are approximately 28% less for the

contoured endwall. Again, this indicates regions of higher heat transfer. The heated endwall non-dimensional temperature profile at X/Cax = 0.50 for the contoured endwall is presented in figure 49.

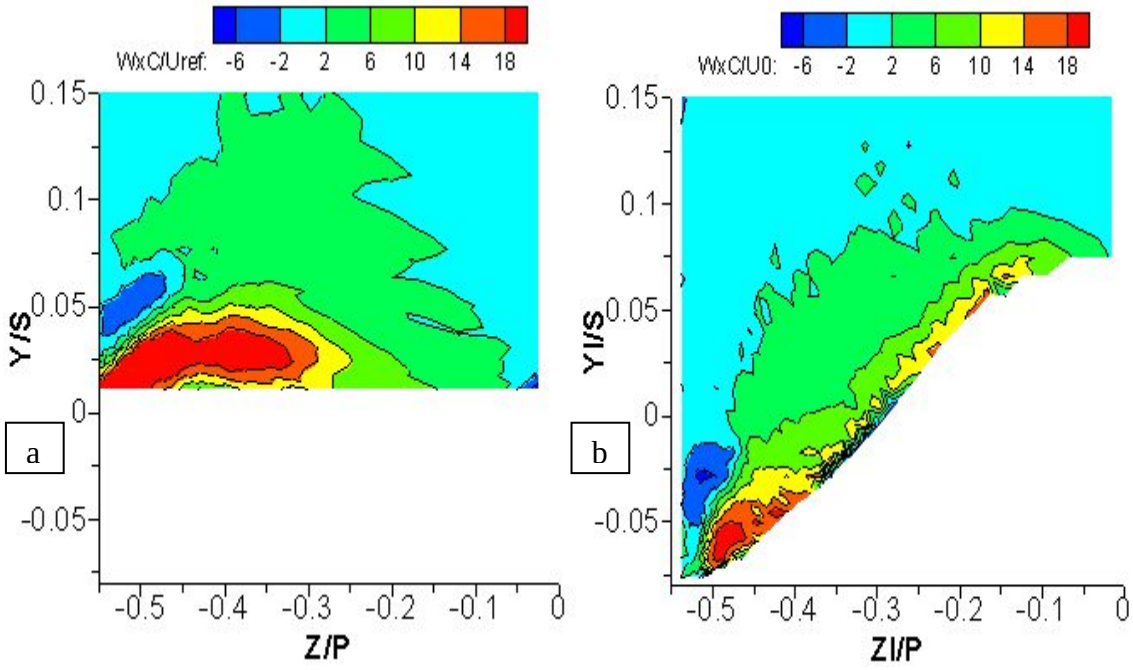

Figure 46: Vorticity at X/Cax = 0.39 (a) baseline, (b) CE

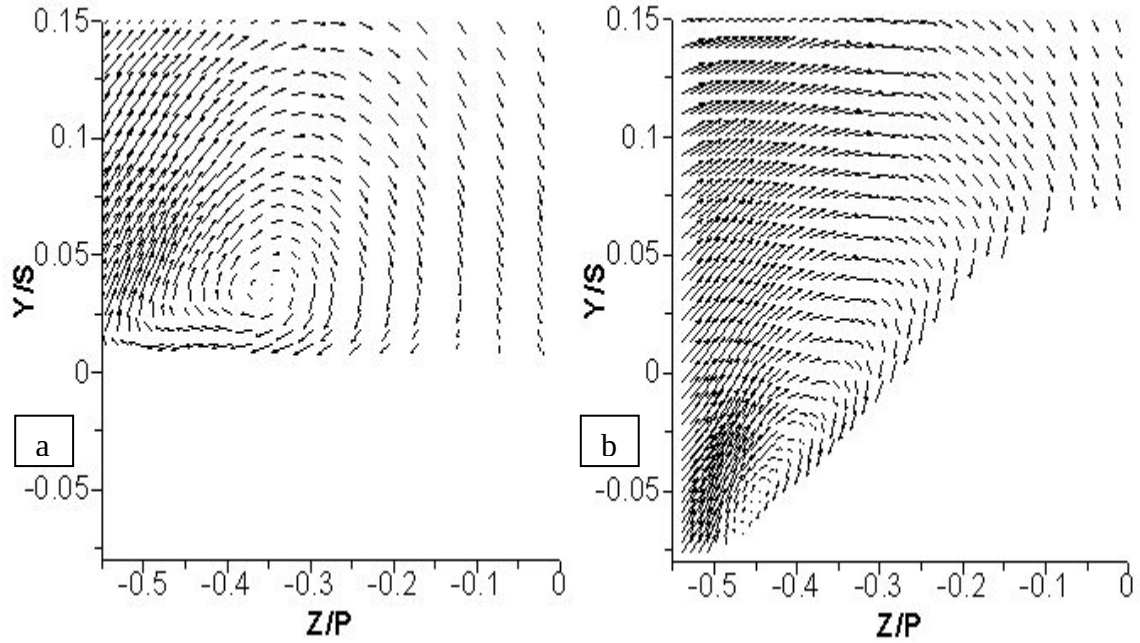

Figure 47: Offset Parallel Plane Vectors at X/Cax = 0.39 (a) baseline, (b) CE

The passage vortex can be seen convecting hotter endwall fluid up and away from the endwall, while cooler fluid is being circulated down along the endwall towards the suction surface. Higher heat transfer coefficients would exist on the endwall near the suction side.

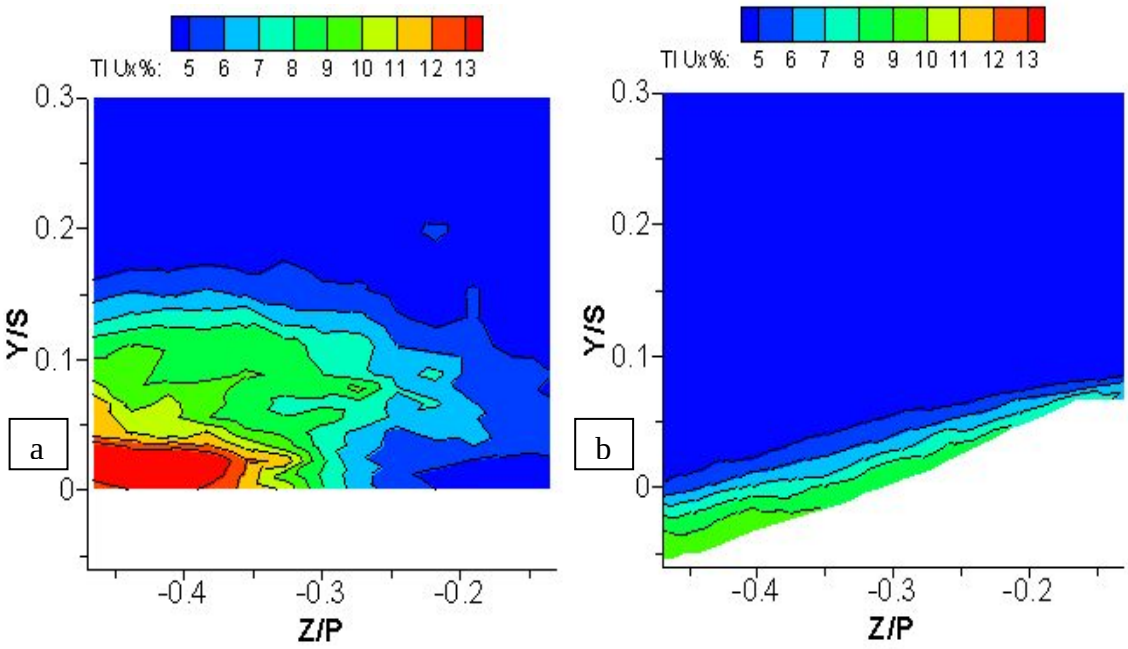

Figure 48: Streamwise Turbulence Intensties at X/Cax = 0.45 (a) baseline, (b) CE

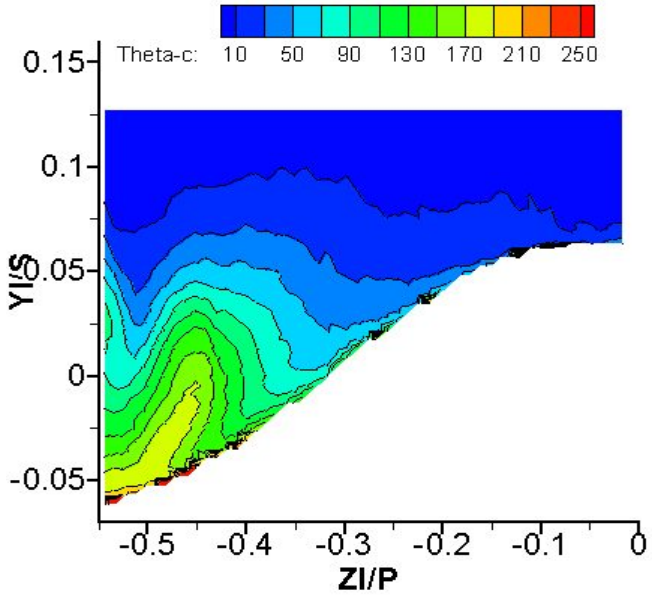

Figure 49: Non-dimensional Temperature at X/Cax = 0.50 for Contoured Endwall

The next plane data will be shown in is at X/Cax = 0.92, which is just upstream of the trailing edge. Pressure loss contours are shown in figure 50. The loss core has moved up the suction surface, showing that the passage vortex has lifted up from the endwall. Again the baseline experiences a much higher pressure loss core. The peak pressure loss core values are a conservative 37% less for the contoured endwall. Mass averaged pressure losses over the entire plane are reduced by 55%.

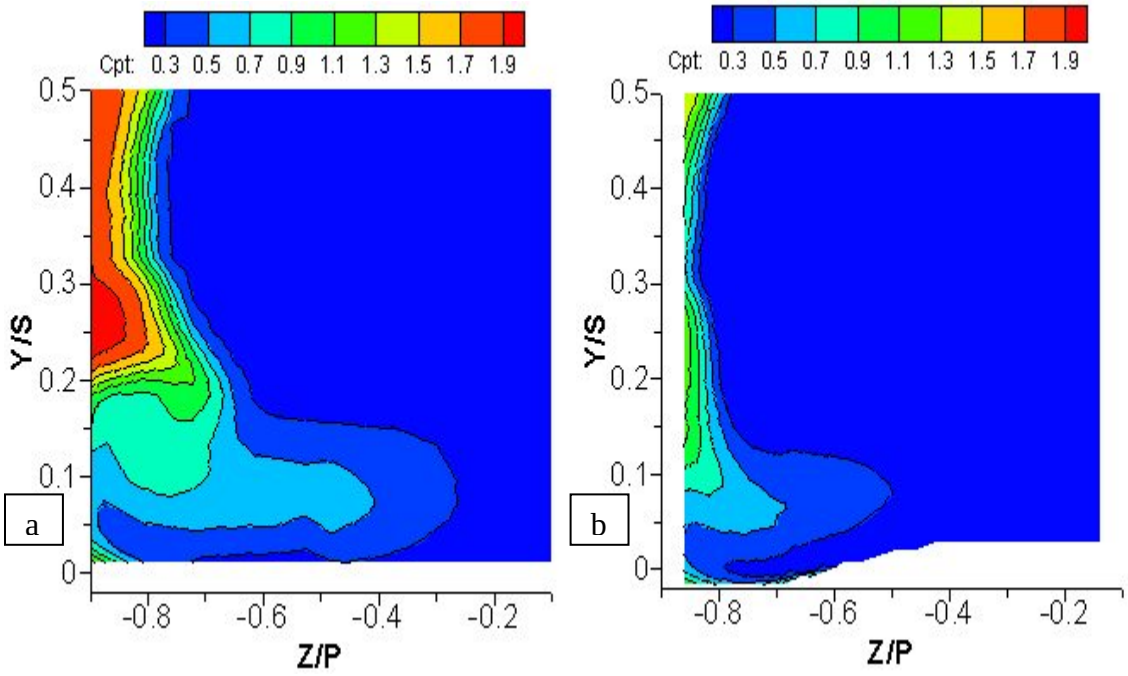

Figure 50: Pressure loss coefficient at X/Cax = 0.92 (a) baseline, (b) CE

Pitchwise velocities, shown in figure 51, at this location help explain why the passage vortex has lifted up. For the baseline case, stronger pitchwise velocities exists near the suction surface up to Y/S = 0.12 than in the inviscid region. This indicates a thick region of cossflow. As this corssflow region approaches the suction surface the flow is deflected and the spanwise component becomes stronger in the positive Y/S direction, pushing the passage vortex up and strengthening it. The contoured endwall case in figure 51 shows a thinner crossflow region from the endwall up to Y/S = 0.05. This indicates that the

crossflow is weaker and does not drive the passage vortex to be as strong as with the baseline. Weaker crossflows also do not push the passage vortex as high as with the baseline.

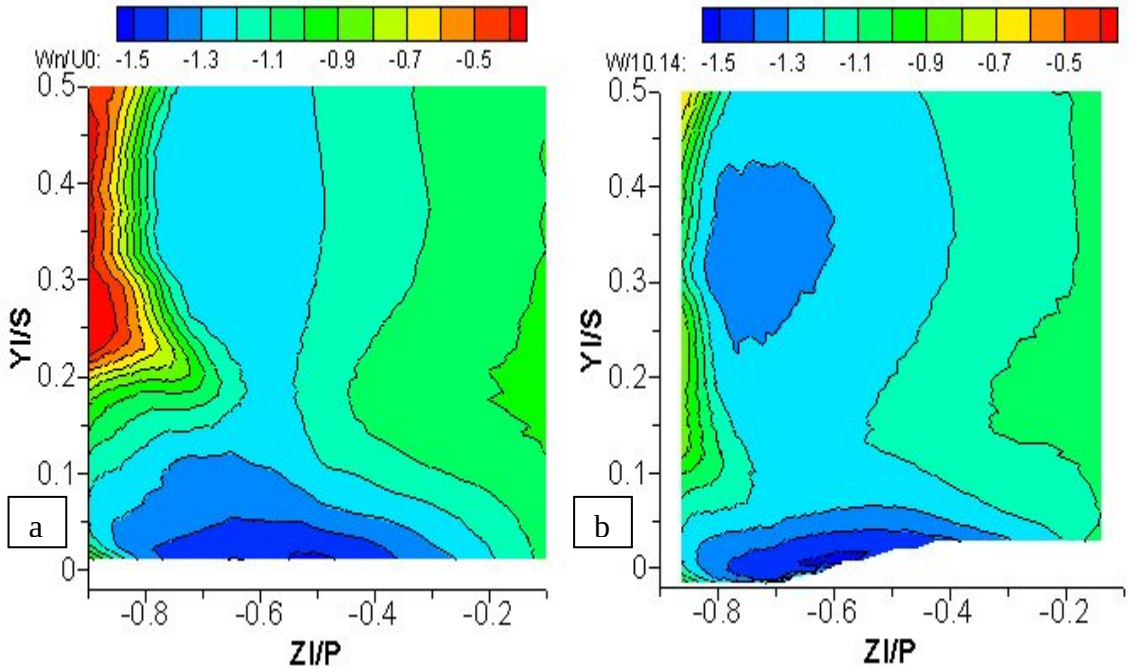

Figure 51: Pitchwise Velocities at X/Cax = 0.92 (a) baseline, (b) CE

Vorticity in this plane is shown in figure 52. It should be remembered that this is axial vorticity and in this plane the vortex axis is approximately at a 70 degree yaw angle away from the perpendicular. Thus, axial vorticity can look stretched and noncircular. The positive vorticity region near the endwall and suction side represents the passage vortex. For the contoured endwall this positive vorticity region is weaker and at a lower spanwise location. Again this shows the contoured endwall has reduced the secondary flow and crossflow strength. A small negative vorticity region exists above the passage vortex and represents the suction side leg of the horseshoe vortex. It is weaker and smaller for the contoured endwall indicating interaction with the passage vortex has reduced its strength. Vectors in offset planes are presented in figure 53.

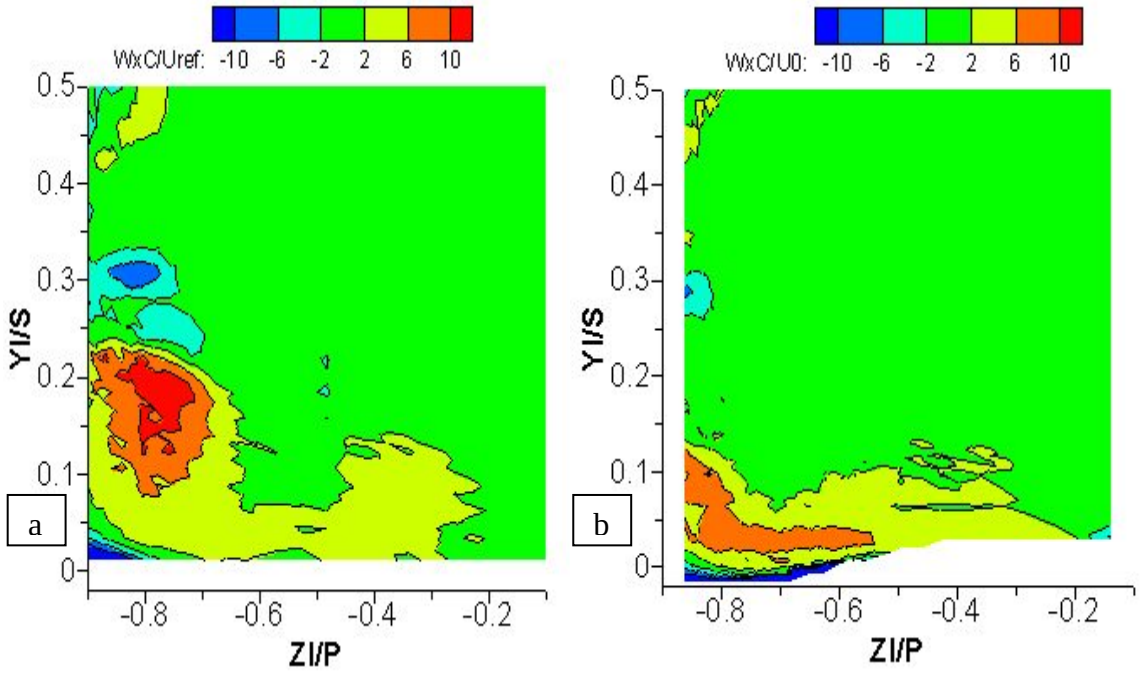

Figure 52: Vorticity at X/Cax = 0.92 (a) baseline, (b) CE

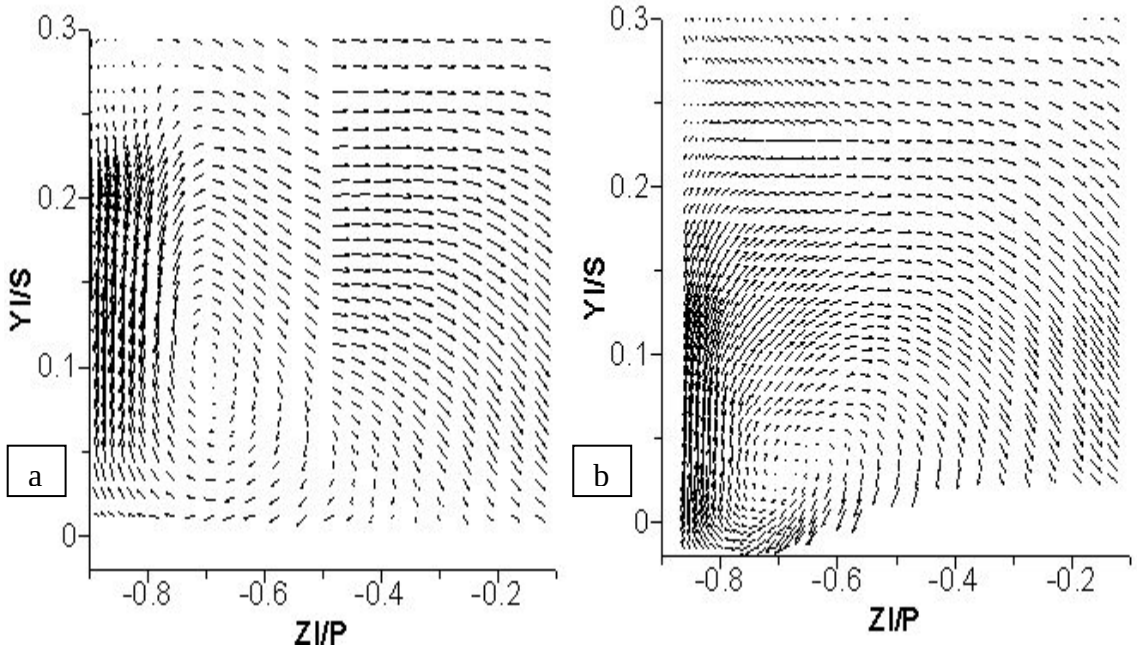

Figure 53: Offset Parallel Plane Vectors at X/Cax = 0.92 (a) baseline, (b) CE

The passage vortex center in the baseline case lies at Z/P = -0.7 and Y/S = 0.09. A smaller and weaker vortex is centered at Z/P = -0.62 and Y/S = 0.05 for the contoured endwall. Stronger upward vertical components along the suction surface exist at higher

spans for the baseline than the contoured endwall. This shows why the passage vortex is pushed up higher in the baseline case. It also explains the high vorticity levels seen above and to the left of the vortex center. Turbulence intensities at X/Cax = 0.94 in figure 54 are not as high with the contoured endwall. Peak values have been reduced by 25%. Higher turbulence levels have lifted above the endwall and should have little effect on endwall heat transfer. Lower turbulence intensities indicate a less unsteady secondary flow field. A less unsteady flow field should have lower pressure losses which is shown to be true in figure 49.

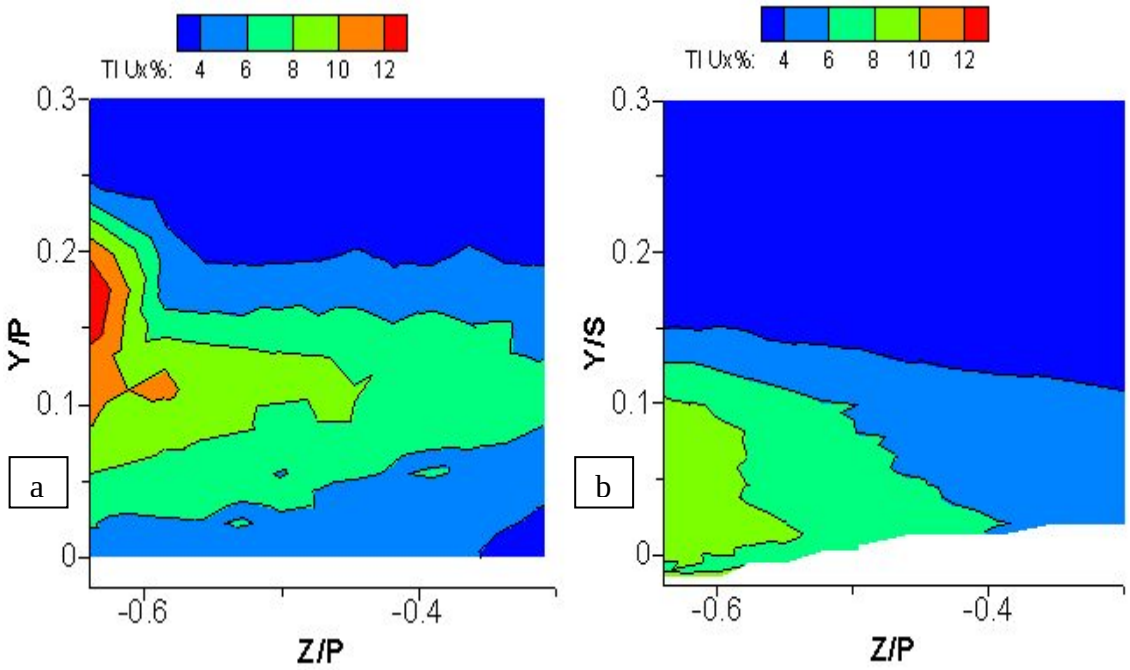

Figure 54: Streamwise Turbulence Intensities at X/Cax = 0.94 (a) baseline, (b) CE

The non-dimensional temperature profile at X/Cax = 0.97 for the contoured endwall is presented in figure 55. The passage vortex has separated from the endwall and now pushes hotter fluid up along the suction surface. Colder bulk temperature fluid is being moved by the crossflow along the endwall from the pressure to suction side. It is important to keep in mind that in an actual turbine engine the temperature fields would be

reversed. The bulk fluid would be at a higher temperature, and it would be desired to keep the endwall and blade walls cool. Here the blade suction surface near the endwall would actually be cooled by the secondary flows. The endwall would be heated more so because of the cross flow.

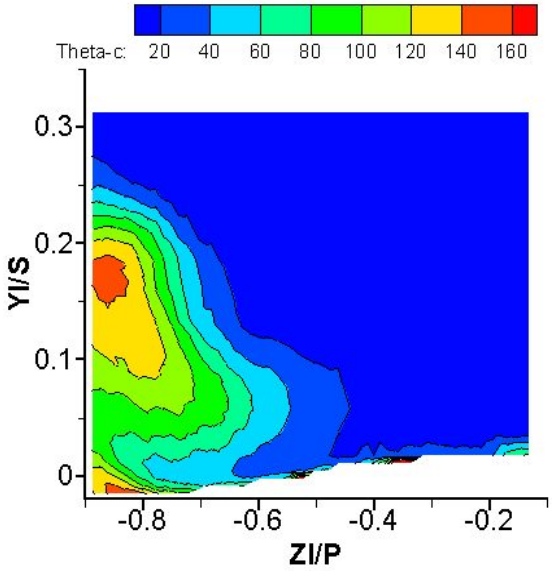

Figure 55: Non-dimensional Temperature at X/Cax = 0.97 for Contoured Endwall

The next plane data will be shown in is downstream of the trailing edge. This plane is important because it shows the exiting flow field of a turbine stage. Losses for the stage can be shown, and the inlet flow field for the following vane row will be known. Figure 56 presents pressure losses at X/Cax = 1.21. The high pressure loss region for the baseline case at Z/P = -0.40 is called the wake. In the inviscid region it is created by higher and lower pressure fluid colliding after the trailing edge. The passage vortex creates the circular loss core region at Y/S = 0.20 and Z/P = -0.20. For the contoured endwall, the wake pressure loss region is still at Z/P = -0.40, but the passage vortex loss core is harder to define. It is the extended high pressure loss region between Z/P = -0.30 to -0.13 and Y/S = 0.08 to 0.18. Peak wake pressure losses are reduced by 18%, and the

passage vortex peak core pressure loss is reduced by a conservative 22%. Mass averaged pressure losses are reduced by 53%.

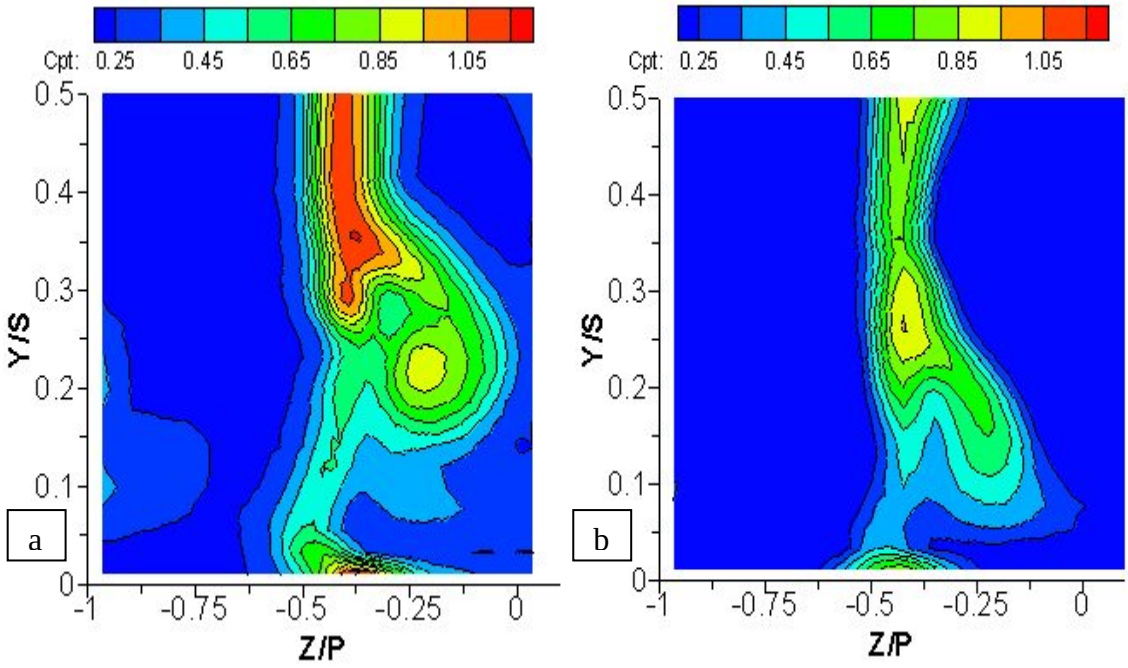

Figure 56: Pressure loss coefficient at X/Cax = 1.21 (a) baseline, (b) CE

Pitchwise velocities are shown in figure 57. In the wake region pitchwise velocities are lower because of losses associated with the high pressure low pressure fluid interacting. The most important advantage with the contoured endwall shown in the velocity contours is that the flow field is more uniform and the wake region is smaller. This is also shown in the pitch averaged yaw angles in figure 61. Yaw angles vary by 21.6 degrees for the baseline case. The contoured endwall yaw angles vary by only 18.3 degrees and deviate from the freestream at a much lower spanwise location. Figure 62 shows pitch averaged pitch angles deviate by 6.2 degrees for the baseline case and only 2.0 degrees for the contoured endwall. A more uniform exit flow field means the following stage will start off more efficiently. These efficiency improvements will only add up for each successive stage.

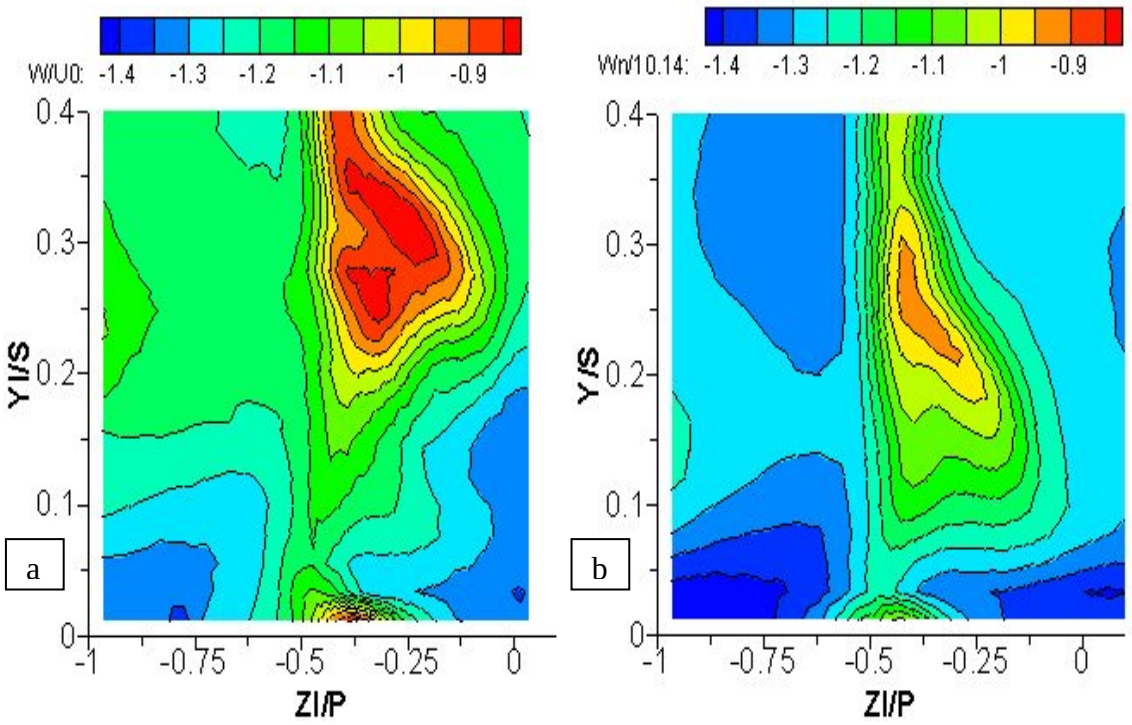

Figure 57: Pitchwise Velocities at X/Cax = 1.21 (a) baseline, (b) CE

Vorticity data is presented in figure 58. The high positive vorticty region for the baseline case at Z/P = -0.20 and Y/S = 0.25 represents part of the passage vortex. A lower vorticity region lies at Z/P = -0.30 and Y/S = 0.20 for the passage vortex with the contoured endwall. Again this shows the passage vortex is weaker and is not lifted as high by the crossflow than that for the baseline case. Overall the secondary flow strength is reduced across the blade passage. The negative vorticity region to the left of the passage vortex results from the suction side leg of the horseshoe vortex. Its strength is greatly reduced by the contoured endwall. Another negative vorticity region exists on the endwall for both cases around Z/P = -0.375. This is an indication of a corner vortex formed in the suction surface endwall corner of the latter half of the passage. Its strength is also reduced by the contoured endwall.

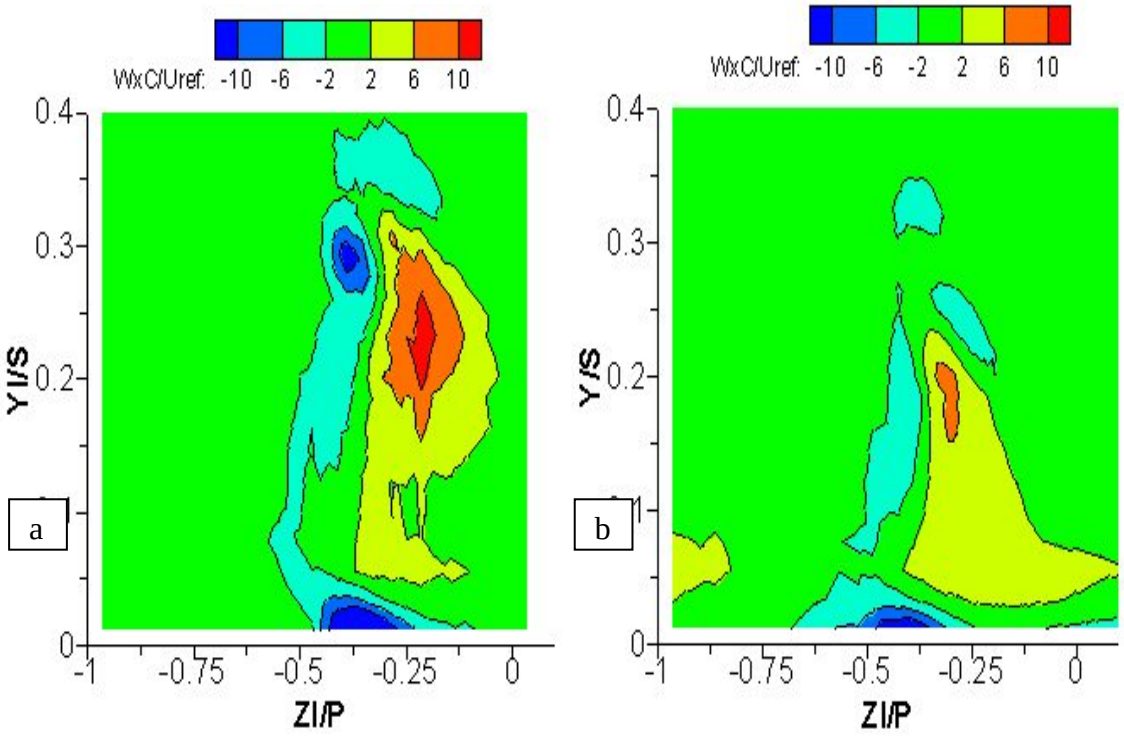

Figure 58: Vorticity at X/Cax = 1.21 (a) baseline, (b) CE

Vectors in offset parallel planes are shown in figure 59. The passage vortex center for the baseline is located at Z/P = -0.20 and Y/S = 0.20. A weaker, smaller, and lower passage vortex can be seen for the contoured endwall at Z/P = -0.20 and Y/S = 0.10. Again the passage vortex is not lifted as high. Higher spanwise velocities to the left and above the vortex center explain why high vorticity levels are seen in this region. Turbulence intensities in the average inviscid streamwise direction for the contoured endwall at X/Cax = 1.23 are shown in figure 60. Higher turbulence intensities lie in the upper half of passage vortex region and not the wake region. This is because velocities on this side of the vortex are higher and create more velocity fluctuations than high pressure low pressure wake interaction.

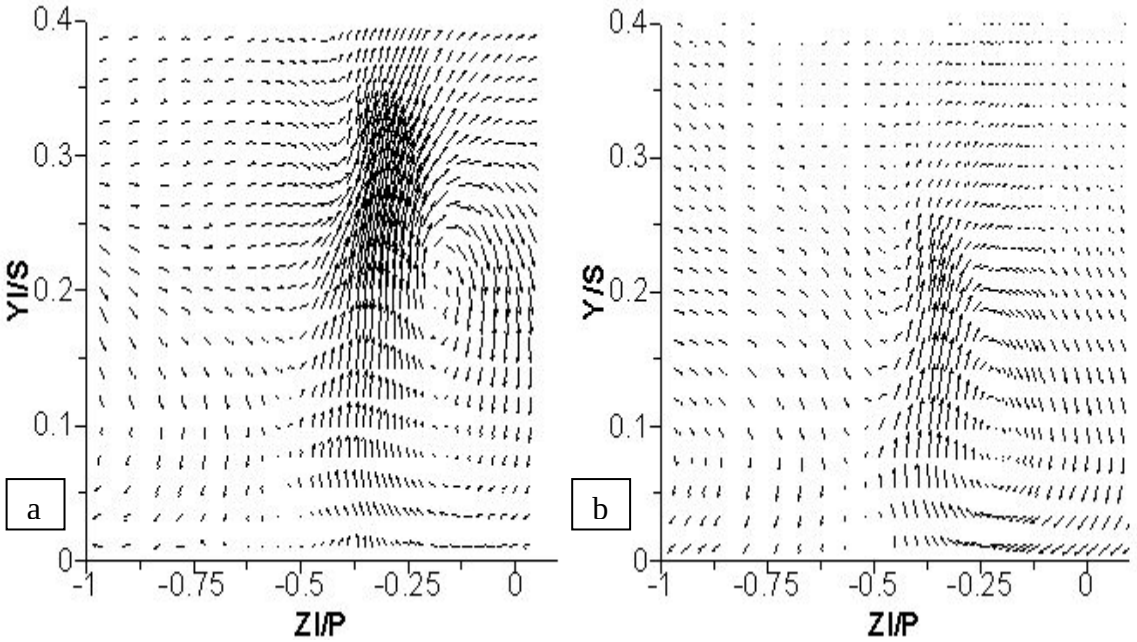

Figure 59: Offset Parallel Plane Vectors at X/Cax = 1.21 (a) baseline, (b) CE

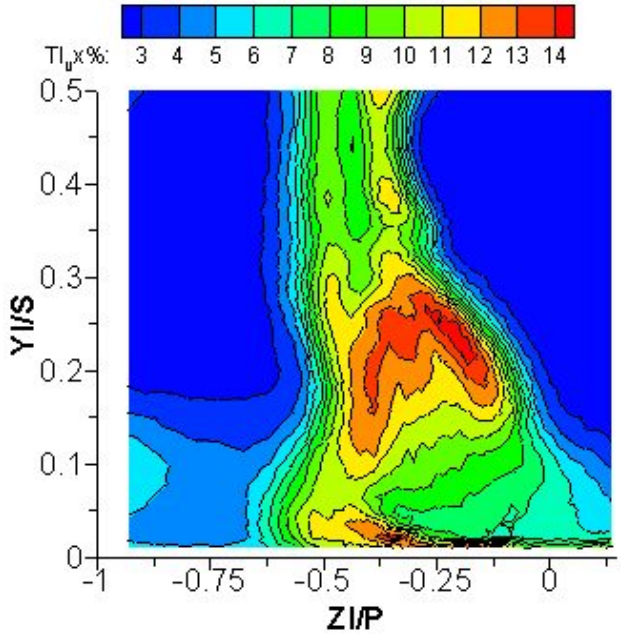

Figure 60: Streamwise Turbulence Intensity at X/Cax = 1.23 for Contoured Endwall

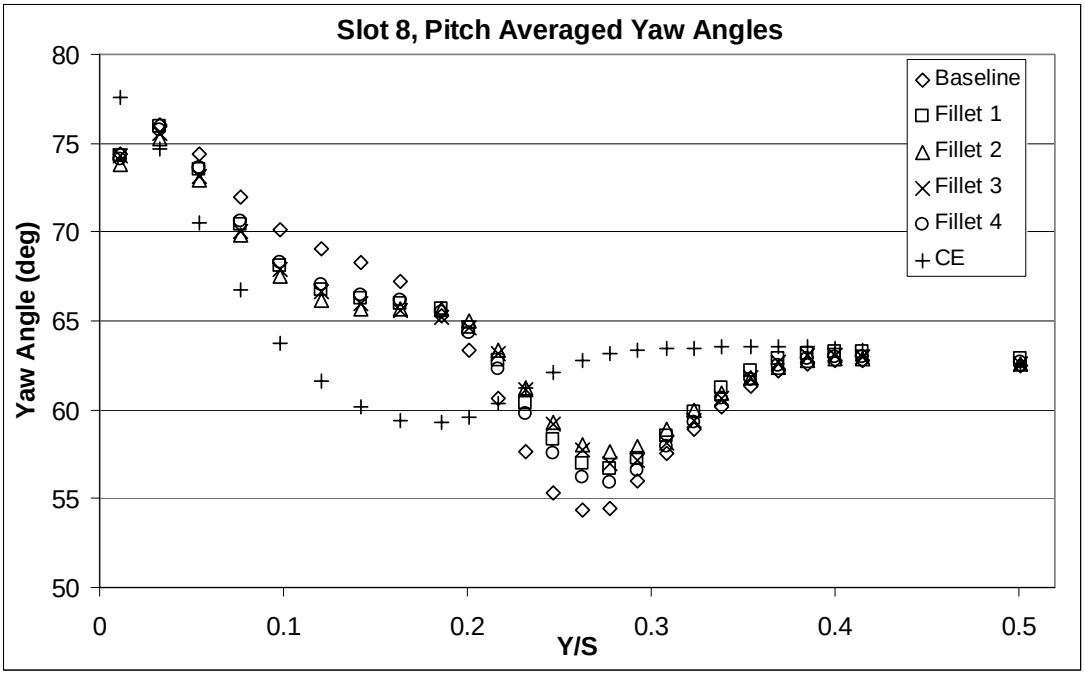

Figure 61: Pitch Averaged Yaw Angles at X/Cax = 1.21

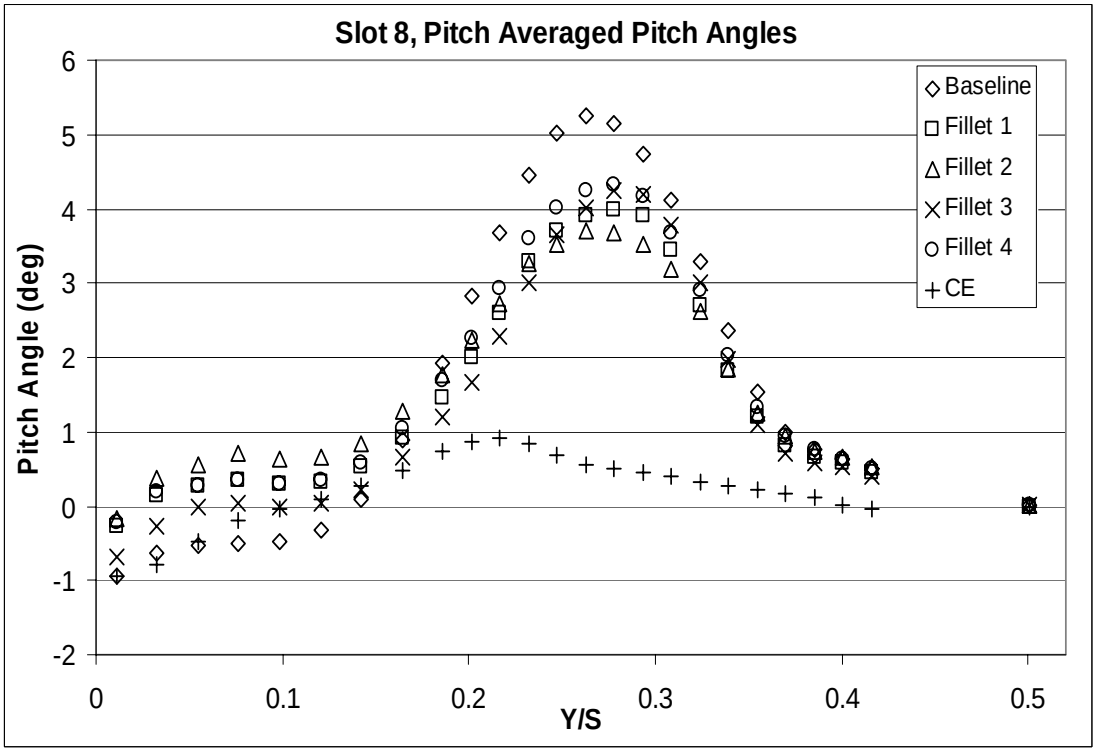

Figure 62: Pitch Averaged Pitch Angles at X/Cax = 1.21

4.5 Film Cooled Non-Axisymmetric Endwall Contour Results

This next section will review the experimental results for the film cooled non-asisymmetric contoured endwall (FCCE) and compare it to the uncooled contoured endwall results. The blade surface pressure coefficient was measured at Y/S = 0.33 with a blowing ratio of 1 and matched that of the uncooled contoured endwall. Endwall pressure measurements could not be made with adequate enough pressure taps. To estimate local blowing ratios the uncooled contoured endwall's static pressure distribution was used. Film cooling will effect the local endwall static pressure distribution but to a small extent. Figure 63 shows each hole's local blowing ratio for a inlet blowing ratio of one.

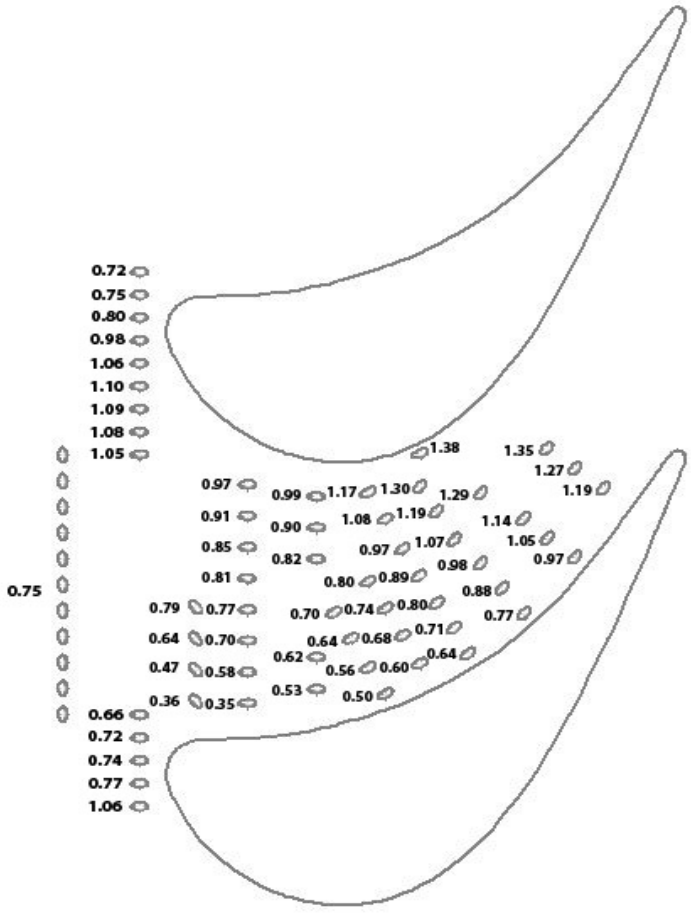

Figure 63: Contoured Endwall Local Blowing Ratios for M=1.0

Velocities were calculated based on the uncooled contoured endwall's local static pressure at the location of each film cooling hole exit and the plenum pressure. Smoke flow visualization could also not be performed because of low speed requirements and added unsteadiness from film cooling. For the current experiments, only a blowing ratio of one and two was tested. Measurements for a blowing ratio of two are shown only in slot 6, X/Cax = 0.92, to determine stage pressure losses. Slot 4, X/Cax = 0.39, showed little difference between the uncooled and cooled case. All hot wire and five hole probe measurements were taken with the mainstream inlet temperature equal to the plenum coolant temperature. Thus only unity temperature and density ratios were tested. This is a requirement for the constant temperature hot wire anemometer and pressure readings. Measurements were not taken downstream of the trailing edge since only the one central passage was cooled. Data taken here would not represent true film cooling because of the effects of the neighboring uncooled passage.

4.5.1 Time Averaged Secondary Flow Structures

Time-averaged flow structures are measured using a five-hole probe and a hot wire anemometer. This section presents measurements of total pressure loss coefficients, mean pitchwise velocity, axial vorticity, offset parallel plane vectors, and pitchwise turbulence intensity for the film cooled contoured endwall (FCCE).

The pressure loss coefficient at X/Cax = 0.39 can be seen in figure 64. As in the previous section the blade suction surface is on the left side of the figure and the blade pressure surface is on the right side at Z/P = 0.0. The high loss region in the suction surface endwall corner of both figures represents the passage vortex. Losses are slightly higher, 0.05%, in the core for the film cooled case. This is to be expected as explained by

Fredricks et al. (1997). For a blowing ratio of one, there exist holes in most of the passage with local blowing ratios below one, as can be seen in figure 63. Fluid exiting these holes has a lower total pressure than the mainstream flow. Adding more low pressure fluid to the inlet boundary layer increases the size and strength of the horseshoe vortex. Overall secondary flow strength is increased and higher losses are seen.

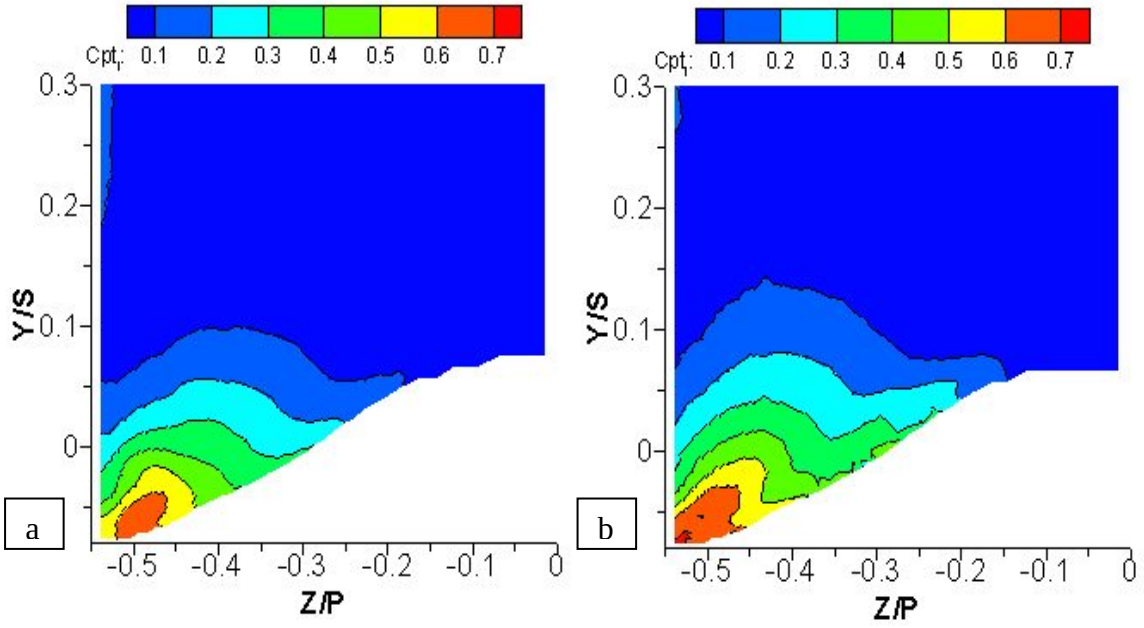

Figure 64: Pressure loss coefficient at X/Cax = 0.39 (a) CE, (b) FCCE

Pitchwise velocities are shown in figure 65, and the two cases are almost identical. The mainstream flow field for the film cooled case shows slightly lower velocities because film cooling slightly reduces the inlet velocity. The stage exit velocity remains the same for both cases. Strong velocities towards the suction side exist on the endwall in both cases and represent the crossflow. The film cooled case shows a slightly more disturbed flow field on the endwall due to coolant jets ejecting fluid from the endwall just upstream of this plane. Vorticity contours are shown in figure 66. The region of high positive vorticity in the uncooled case represents the passage vortex. Passage vortex vorticity

levels are slightly reduced for the film cooled case, but the positive vorticity region is larger. This is because the passage vortex is very near the ejected fluid from the coolant holes, and the vortex size is slightly increased. A small negative vorticity region exists along the endwall for the cooled case. This is due to fluid being ejected slightly towards the suction side along a downward slope. Negative vorticity is created when this fluid moves down towards the endwall. This negative vorticity protrudes into the passage vortex very near the endwall and makes it seem weaker. It should be kept in mind that these are not true vortexes and their lower pressures will strengthen the passage vortex and crossflow.

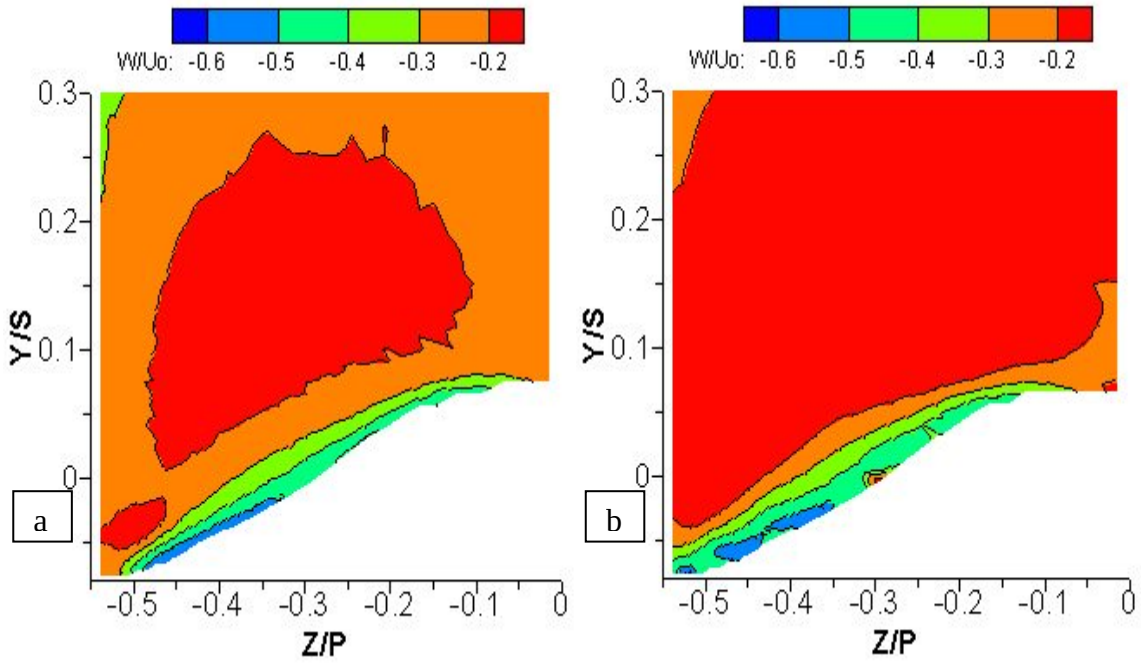

Figure 65: Pitchwise velocity at X/Cax = 0.39 (a) CE, (b) FCCE

Vector plots in offset parallel planes are shown in figure 67. The center of the vortex has been shifted slightly towards the suction side from Z/P = -0.45 to Z/P = -0.47, showing film cooling has pushed the passage vortex over slightly.

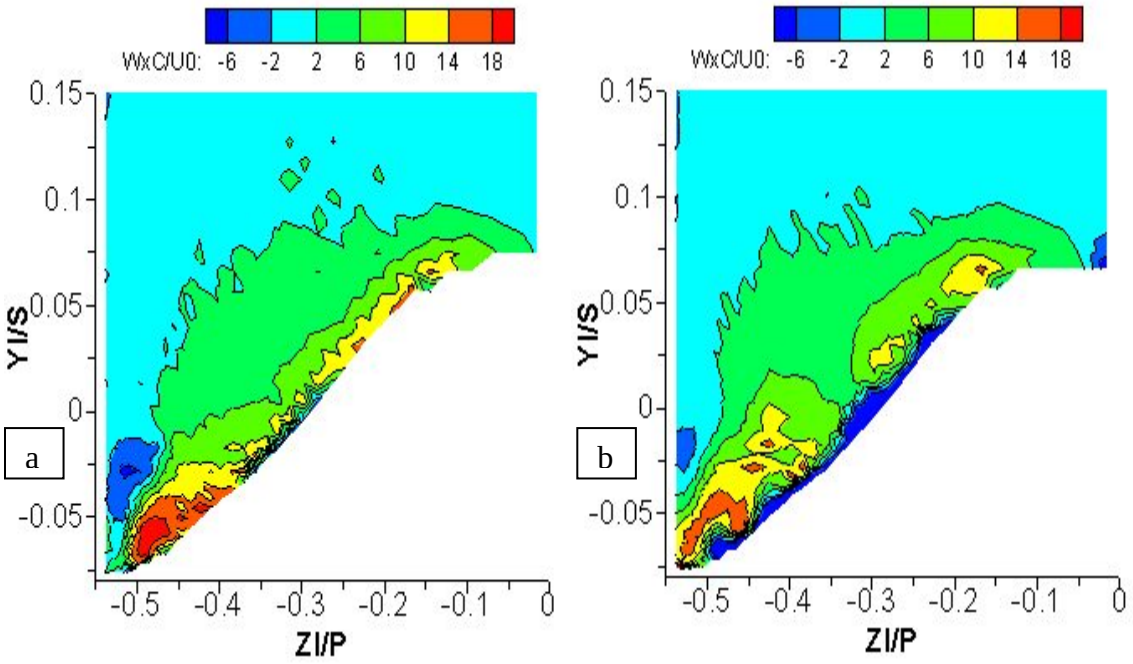

Figure 66: Vorticity at X/Cax = 0.39 (a) CE, (b) FCCE

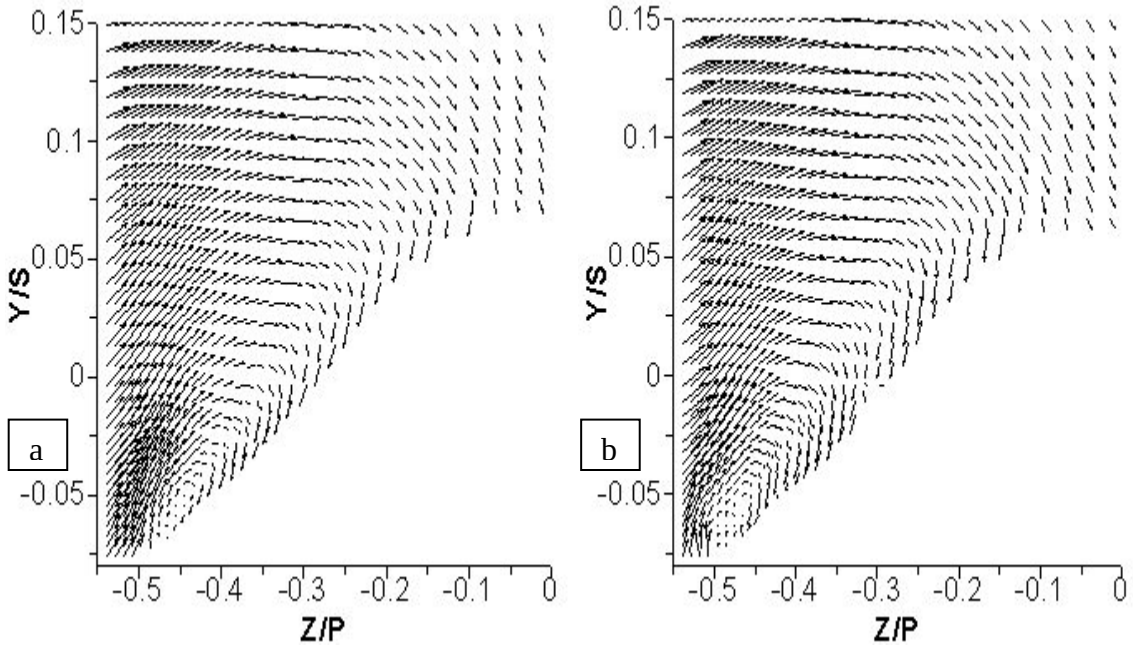

Figure 67: Offset Parallel Plane Vectors at X/Cax = 0.39 (a) CE, (b) FCCE

Turbulence intensities in the pitchwise direction are shown in figure 68. Higher intensity levels can be seen in the passage vortex region for the uncooled case. Figure 63 shows local blowing ratios near the suction surface in this plane are almost one. Although the

injected fluid has a lower total pressure than the freestream fluid, its total pressure is slightly higher than that of fluid near the endwall. Film cooling straightens and smoothes the secondary flows and reduces the unsteadiness by injecting slightly higher total pressure fluid. Lower turbulence intensity levels will also reduce heat transfer levels.

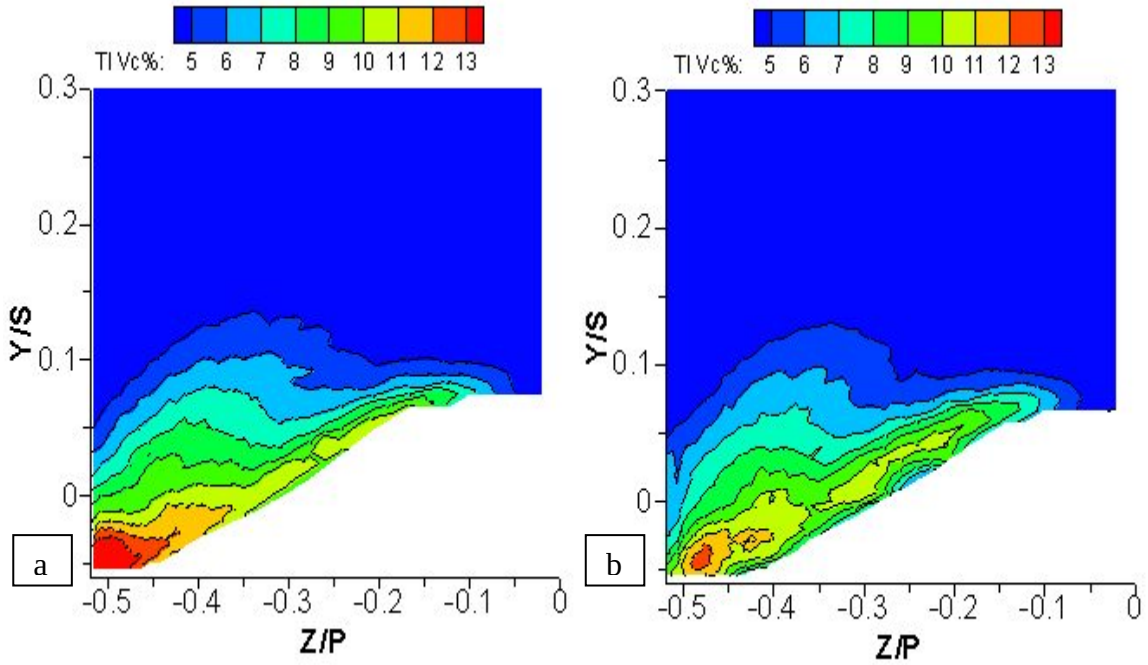

Figure 68: Pitchwise Turbulence Intensties at X/Cax = 0.45 (a) CE, (b) FCCE

Near the trailing edge greater differences can be seen between the uncooled and cooled contoured endwall. All the film cooling holes are located upstream of the plane at X/Cax = 0.92. In this plane, the overall effects of film cooling can be observed. Figure 69 shows the total pressure loss coefficient at X/Cax = 0.92. Peak loss coefficients have increased by 33% for the film cooled case. Mass averaged pressure losses increased by 24% for a blowing ratio of one and 48% for a blowing ratio of two. These losses still remain below that of the baseline case. This is due to a stronger crossflow strengthening and lifting the stronger passage vortex further up the blade suction surface.

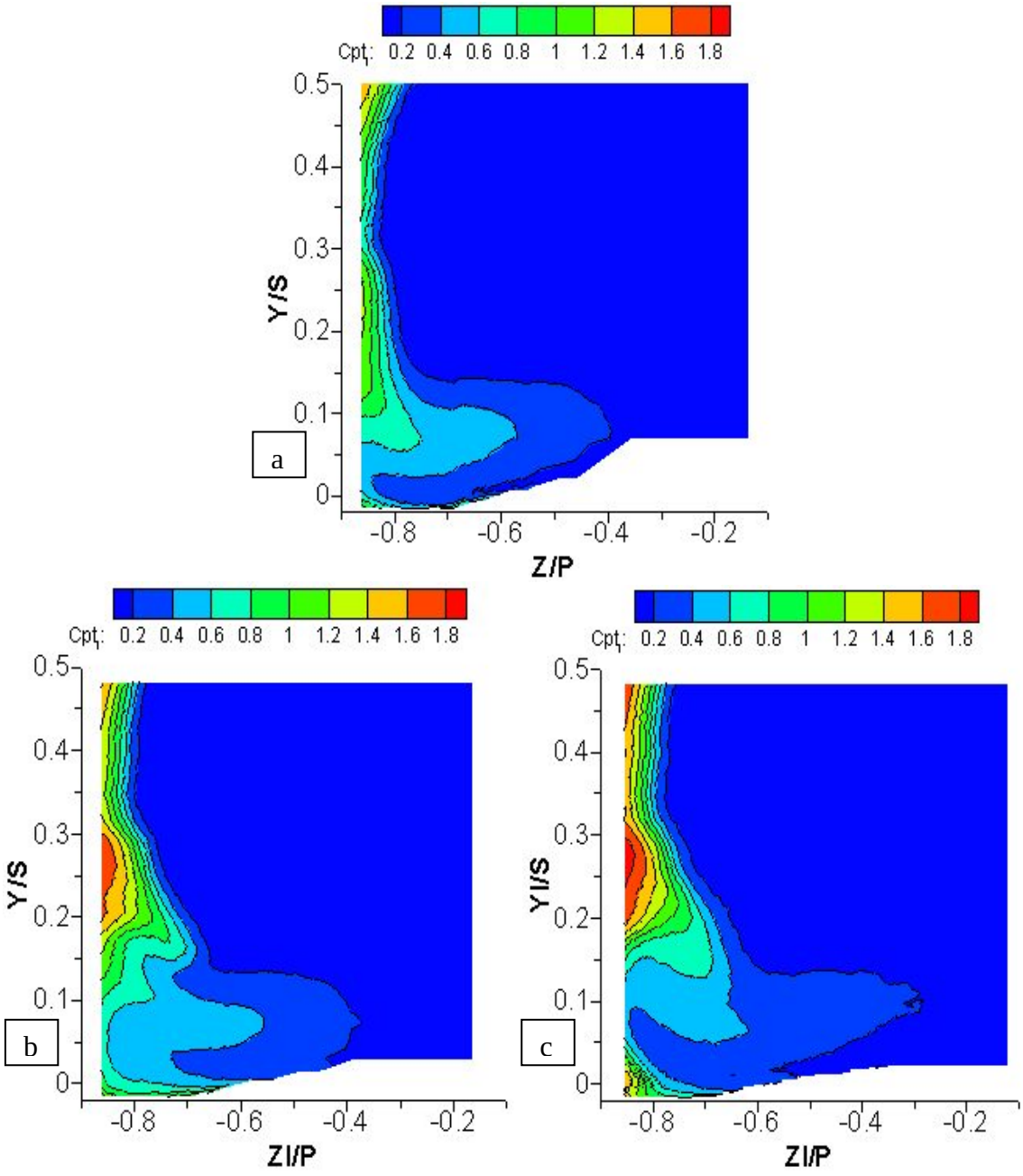

Figure 69: Pressure loss coefficient at X/Cax = 0.92 (a) CE, (b) FCCE (M = 1.0), (c) FCCE (M = 2.0)

Pitchwise velocities are shown in figure 70. For the most part the velocity field is the same for both cases except near the suction surface and endwall. The lower velocity region on the suction surface around Y/S = 0.15 for the cooled endwall represents the upper half of the clockwise rotating passage vortex. Lower velocities in this region show

that the passage vortex is stronger for both film cooled cases. The high velocity regions on the endwall represent the crossflow. A thicker crossflow region strengthens and lifts the passage vortex for the film cooled cases.

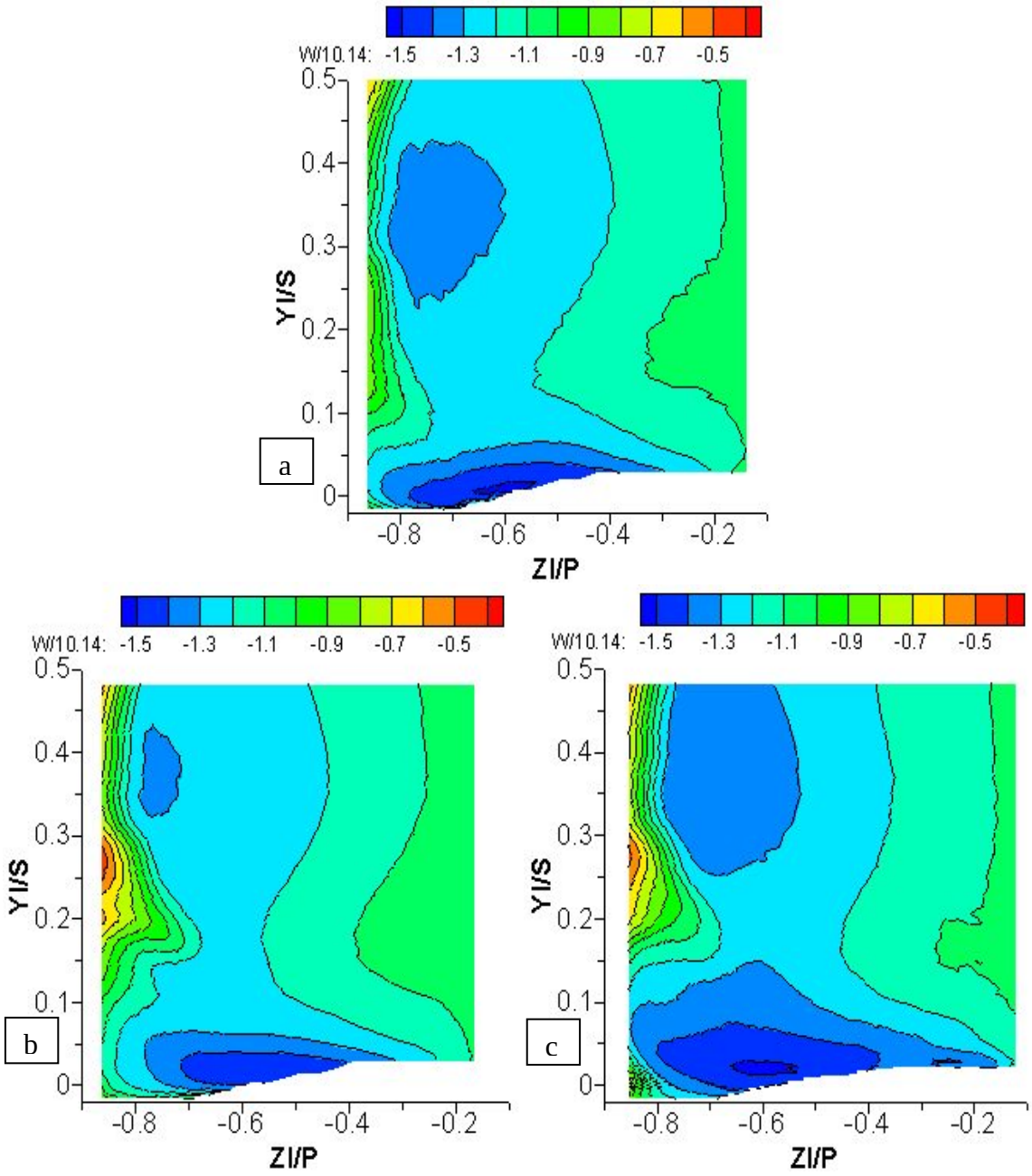

Figure 70: Pitchwise Velocities at X/Cax = 0.92 (a) CE, (b) FCCE (M = 1.0), (c) FCCE (M = 2.0)

Vorticity is presented in figure 71. It should be remembered that this is axial vorticity and in this plane the vortex axis is approximately at a 70 degree yaw angle away from the perpendicular. Thus, axial vorticity can look stretched and noncircular. The blowing ratio of one film cooled case shows slightly higher and larger positive vorticity regions representing the passage vortex. For a blowing ratio of two, the vorticity levels are slightly decreased but but the positive vorticity region is slightly higher. This suggests the passage vortex is larger but weaker for a blowing ratio of two. Two small positive vorticity regions can be seen on the endwall near the pressure surface, X/Cax = -0.2, for a blowing ratio of two. These represent the two film cooling jets which eject just upstream of this plane and are seen because of an increased hole exit velocity. Lower pressure, than that of the mainstream, film cooling fluid has strengthened the passage vortex for a blowing ratio of one. Ultimately higher blowing ratio film cooling strengthens the crossflow which in turn strengthens the passage vortex. The peak vorticity levels in the film cooled case do not represent the passage vortex core and can be better explained by the vector plots. Figure 72 shows vector plots in offset parallel plans. The passage vortex clockwise rotating structure is well defined in each case. A slightly larger and stronger structure can be seen with the film cooled cases. Strength and size differences are most notable in the upward velocities along the suction surface. The vector lengths represent magnitude, and it can be seen that strong spanwise velocities exist up to about Y/S = 0.17 along the suction surface for the uncooled case. The film cooled case shows strong spanwise velocities up to about Y/S = 0.22, revealing a stronger and larger passage vortex. Sharp turning in the flow in the region from Z/P = -0.70 to -0.80 and Y/S = 0.15 to 0.20 explains the high vorticity levels seen in this region. The vortex center for the

uncooled case lies at Z/P = -0.70 and Y/S = 0.30. Film cooling has shifted it away from the pressure surface to Z/P = 0.61 and slightly higher to Y/S = 0.50. Pitchwise turbulence intensity levels are shown in figure 73. Again the film cooled case shows reduced intensity levels because the secondary flows are filled with slightly higher pressure fluid.

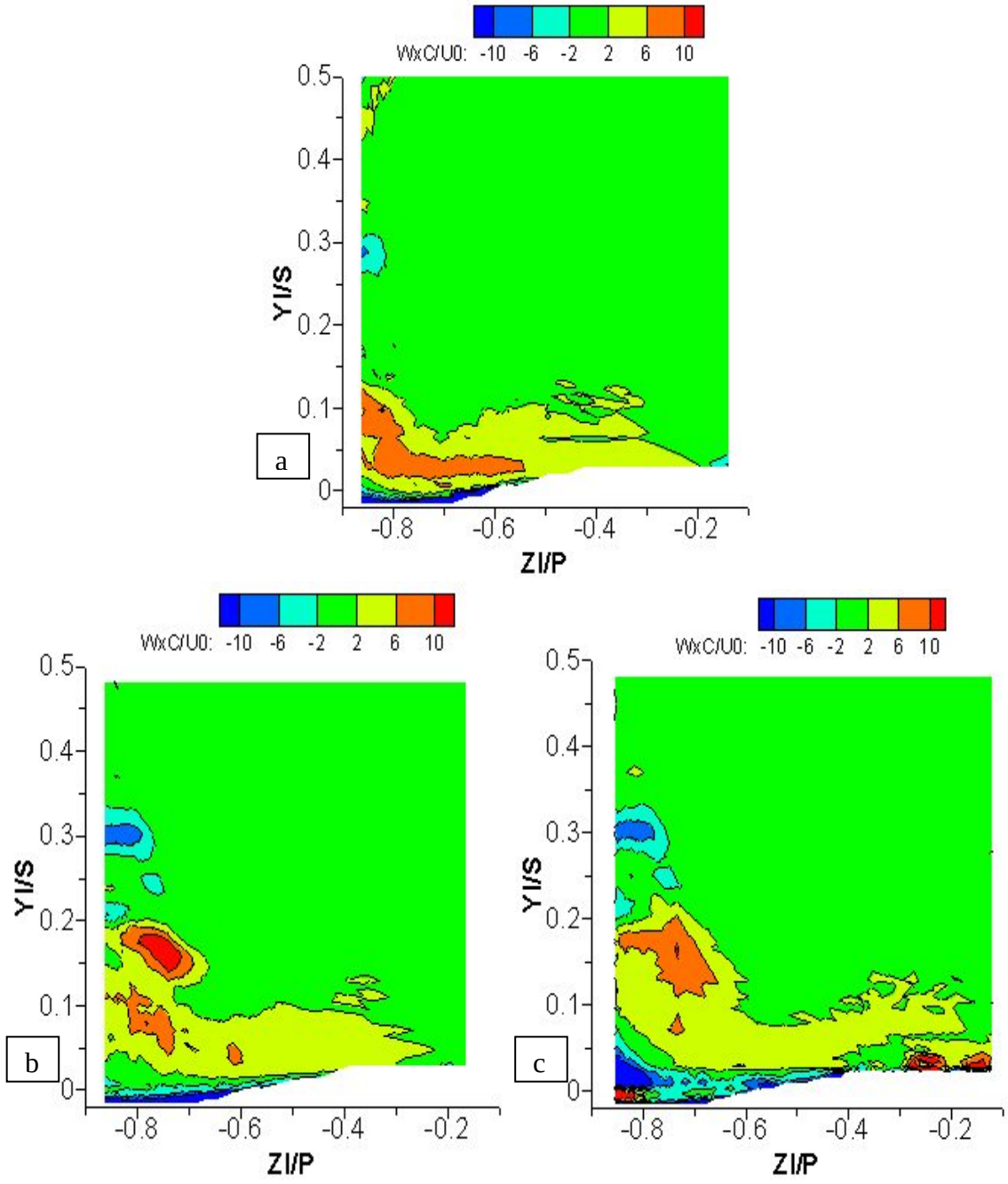

Figure 71: Vorticity at X/Cax = 0.92 (a) CE, (b) FCCE (M = 1.0), (c) FCCE (M = 2.0)

The resulting secondary flows are larger and stronger but become less unsteady with film cooling. For the blowing ratio of two case, high turbulence levels have lifted away from the endwall. This is due to high pressure film cooling fluid occupying the near endwall region.

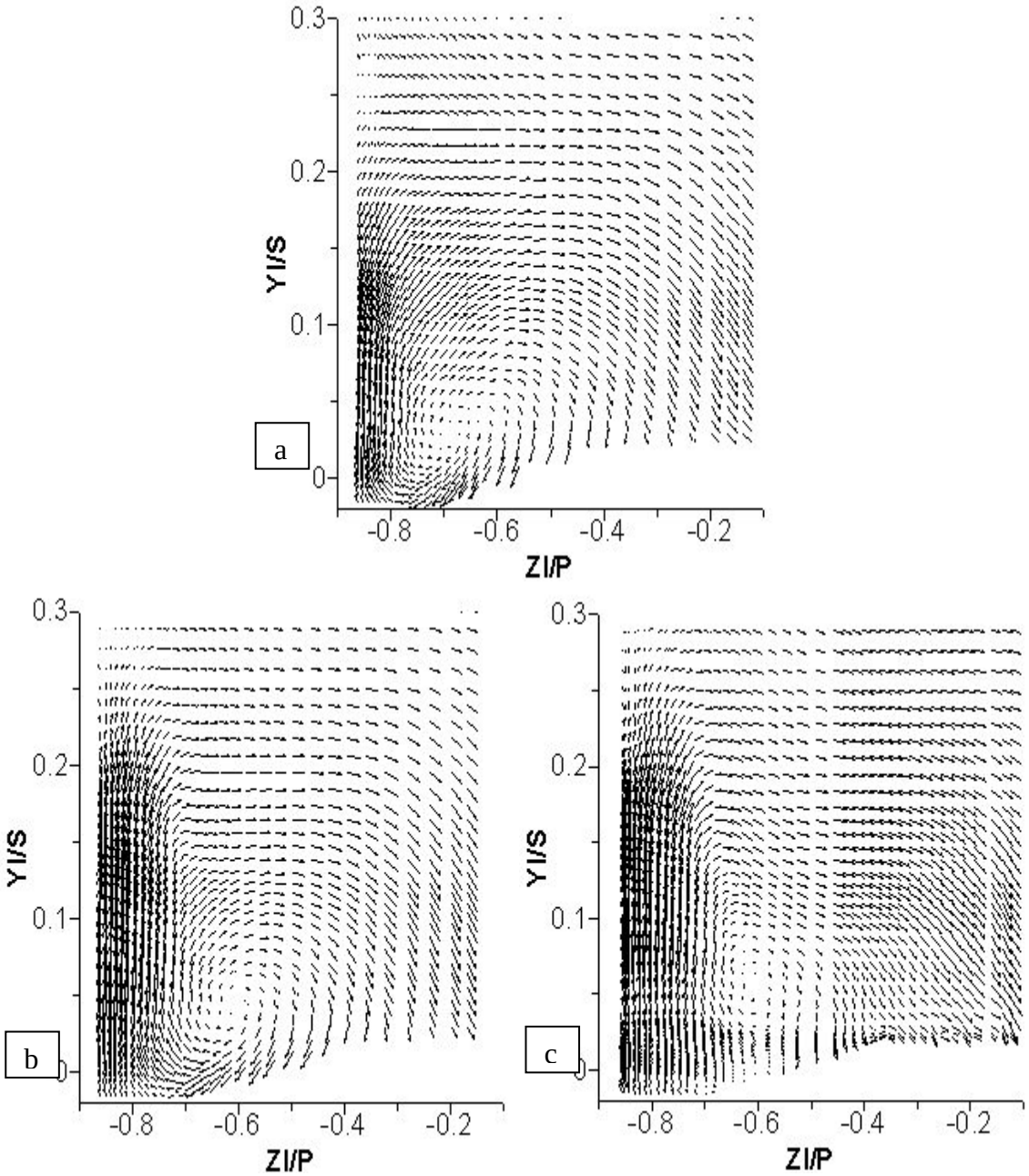

Figure 72: Offset Parallel Plane Vectors at X/Cax = 0.92 (a) CE, (b) FCCE (M = 1.0), (c) FCCE (M = 2.0)

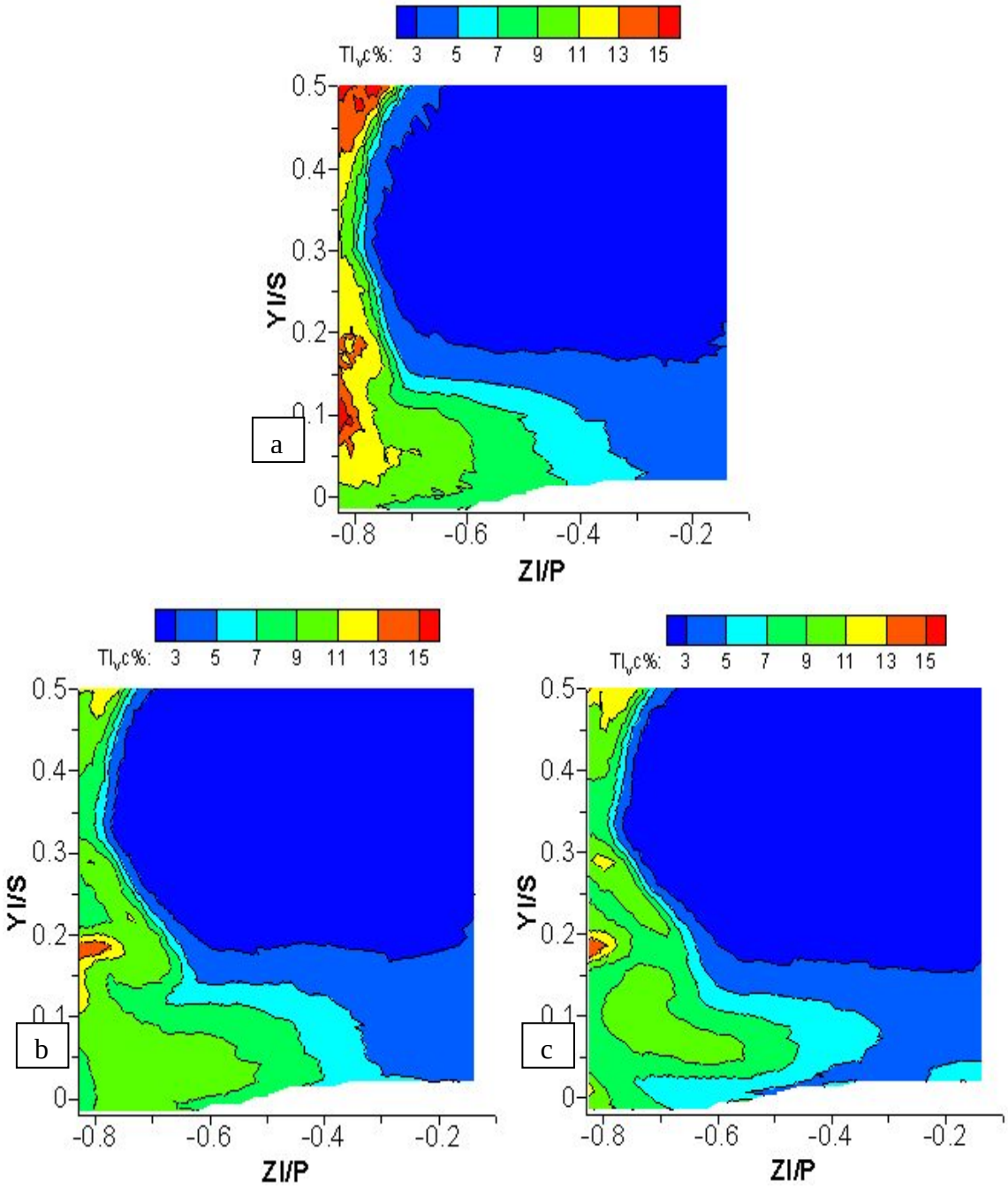

Figure 73: Turbulence Intensities at X/Cax = 0.94 (a) CE, (b) FCCE (M = 1.0), (c) FCCE (M = 2.0)

Chapter 5. Conclusion

Experimental results are presented on flow structures in a linear blade passage with leading edge fillets, non-axisymmetric endwall contouring, and film cooling. Peak total pressure loss coefficients in slots 4, 6, and 8 are shown in table 5. Table 6 shows mass averaged total pressure loss coefficients. These values show that the uncooled contoured endwall reduces pressure losses the most.

Table 5: Peak Total Pressure Loss Coefficients

Case	Slot 4	Slot 6	Slot 8 (wake)	Slot 8 (vortex)
Baseline	0.81	1.95	1.15	0.92
Fillet 1		1.83	1.17	0.87
Fillet 2		1.92	1.10	0.82
Fillet 3		1.98	1.22	0.86
Fillet 4		1.95	1.15	0.87
Contoured Endwall	0.67	1.22	0.90	0.70
Film Cooled Contoured Endwall	0.70	1.75		

Table 6: Mass Averaged Total Pressure Loss Coefficients

Case	Slot 6 (X/Cax = 0.92)	Slot 8 (X/Cax = 1.21)
Baseline	0.331	0.410
Fillet 1		0.407
Fillet 2		0.483
Fillet 3		0.408
Fillet 4		0.409
Contoured Endwall	0.147	0.190
Film Cooled Contoured Endwall (M = 1.0)	0.183	
Film Cooled Contoured Endwall (M = 2.0)	0.235	

Four different fillet profiles are studied: fillet 1 (EW&B) blends a linear profile simultaneously toward the end wall and the blade, fillet 2 (EW) blends a linear profile to the end wall only, fillet 3 (B) blends a linear profile to the blade only, and fillet 4 (curved

EW&B) blends a concave circular profile both to the end wall and the blade. The objective of the study is to explore the potential of the different fillet profiles in reducing the strength of the secondary flow structures. Instantaneous flow visualization images show smaller horseshoe vortex structures in the stagnation region with the leading edge fillets than with the baseline case. In the passage region, the secondary vortex structures are smaller in size near the leading edge, but the structures become comparable in size as the throat region is approached. The flow structure measurements (five-hole probe and hot wire anemometry) also show smaller magnitudes of near wall vorticity and lower positive values of pitchwise velocity in the region between the leading edge and the throat indicating weaker passage vortex structures in this region. Total pressure loss coefficients in pitchwise planes just downstream of the exit plane indicate no reductions in the total loss profile, but show that the fillets shift the passage vortex upwards by about *0.02S* to *0.025S*. Turbulence intensity magnitudes at different axial locations indicate that the fillets reduce the turbulence intensity in the near wall regions upstream of the throat. This mechanism would help reduce endwall heat transfer upstream of the throat.

The non-axisymmetric contoured endwall was designed to reduce the cross passage pressure gradient which would thereby reduce the crossflow strength. This is achieved by making the endwall convex near the pressure surface and concave near the suction surface. Convex curvature accelerates the flow and lowers endwall pressures in the high pressure region. The concave curvature increases pressure near the suction surface. A pitchwise curve was multiplied with an axial curve to create the endwall curvature. Pressure losses were decreased, with respect to the baseline case, through out the passage. Peak wake pressure losses are reduced by 18%, and mass averaged pressure

losses are reduced by 53%. This is due to reduced secondary flow size and strength. The horseshoe vortex is severely weakened and is displaced far upstream of the blade. A reduced cross passage pressure gradient reduces the crossflow, so the passage vortex is not strengthened as much as with the baseline case. The passage vortex is also not lifted as high with weaker crossflows. This leads to a more uniform exit flow field which will improve the efficiency of a downstream stage. Weaker secondary flows will produce more desireable endwall heat transfer rates. Turbulence intensities near the endwall were reduced which will also decrease heat transfer rates on the endwall.

Film cooling was added to the non-axisymmetric contoured endwall to examine how the flow field was affected. Cooling holes were placed along lines which were perpendicular to streamlines. This would help insure that ejected coolant would not interact with that of a neighboring hole and be wasted. Since the contoured endwall's surface angles constantly changed, each hole was made to eject at thirty degrees relative to the local surface angle at each hole's exit. With a blowing ratio of one, pressure losses throughout the channel were slightly increased but did not exceed that of the baseline case. Mass averaged pressure losses increased by 24% for blowing ratio one and 48% for blowing ratio two. The losses increased because crossflows were strengthened by film cooling, strengthening the secondary flows. The passage vortex position changed little from the uncooled contoured endwall case. Film cooling also reduced turbulence intensity levels along the endwall. Although for a blowing ratio of one, the injected fluid was of lower pressure than the mainstream flow, it was at a higher pressure than the present near wall fluid. This helped to smoothen and straighten the near wall flow field which produced lower turbulence intensity levels.

References

Bario, F., F. Leboeuf, A. Onvani, A. Seddini. “Aerodynamics of Cooling Jets Introduced in the Secondary Flow of a Low-Speed Turbine Cascade.” ASME Journal of Turbomachinery 112 (1990): 539-546.

Boletis, E. “Effects of Tip Endwall Contouring on the Three-Dimensional Flow Field in an Annular Turbine Nozzle Guide Vane: Part 1 – Experimental Investigation.” ASME Journal of Engineering for Gas Turbines and Power 107 (1985): 983-990.

Burd, Steven W., Terrence W. Simon. “Effects of Slot Bleed Injection Over a Contoured Endwall on Nozzle Guide Vane Cooling Performance: Part I – Flow Field Measurements.” ASME Paper 2000-GT-199, Munich 2000.

Davenport, W. J., N. K. Agarwal, M. B. Dewitz, R. L. Simpson, K. Poddar. “Effects of a Fillet on the Flow Past a Wing-Body Junction.” AIAA Journal 28 (1990): 2017-2024.

Dossena, V., A. Perdichizzi, M. Savini. “The Influence of Endwall Contouring on the Performance of a Turbine Nozzle Guide Vane.” ASME Journal of Turbomachinery 121 (1999): 200-208.

Friedrichs, S., H. P. Hodson, W. N. Dawes. “Aerodynamic Aspects of Endwall Film-Cooling.” ASME Journal of Turbomachinery 119 (1997): 786-793.

Friedrichs, S., H. P. Hodson, W. N. Dawes. “Distribution of Film-Cooling Effectiveness on a Turbine Endwall Measured Using the Ammonia and Diazo Technique.” ASME Journal of Turbomachinery 118 (1996): 613-621.

Friedrichs, S., H. P. Hodson, W. N. Dawes. “The Design of an Improved Endwall Film-Cooling Configuration.” ASME Journal of Turbomachinery 121 (1999): 772-780.

Gregory-Smith, D. G., J. G. E. Clerk. “Secondary Flow Measurements in a Turbine Cascade With High Inlet Turbulence.” ASME Journal of Turbomachinery 144 (1992): 173-183.

Harasgama, S. P. “Film Cooling Research on the Endwall of a Turbine Nozzle Guide Vane in a Short Duration Annular Cascade: Part 1 – Experimental Technique and Results.” ASME Journal of Turbomachinery 114 (1992): 734-740.

Hartland, J. C., D. G. Gregory-Smith, M. G. Rose. “Non-Axisymmetric Endwall Profiling in a Turbine Rotor Blade.” ASME Paper 98-GT-525, Stockholm 1998.

Hartland, J. C., D. G. Gregory-Smith, N. W. Harvey, M. G. Rose. "Nonaxisymmetric Turbine End Wall Design: Part II – Experimental Validation." ASME Journal of Turbomachinery 122 (2000): 286-293.

Harvey, Neil W., Martin G. Rose, Mark D. Taylor, Shahrokh Shahpar, Jonathan Hartland, David G. Gregory-Smith. "Nonaxisymmetric Turbine End Wall Design: Part I – Three-Dimensional Linear Design System." ASME Journal of Turbomachinery 122 (2000): 278-285.

Jabbari, M. Y., K. C. Marston, E. R. G. Eckert, R. J. Goldstein. "Film Cooling of the Gas Turbine Endwall by Discrete-Hole Injection." ASME Journal of Turbomachinery 118 (1996): 278-284.

Kang, M. B., K. A. Thole. "Flowfield Measurements in the Endwall Region of a Stator Vane." ASME Journal of Turbomachinery 122 (2000): 458-466.

Knost, D. G., K. A. Thole. "Adiabatic Effectiveness Measurements of Endwall Film-Cooling for a First Stage Vane." ASME Paper GT2004-53326, Vienna 2004.

Lethander, Andrew T., Karen A. Thole, Gary Zess, Joel Wagner. "Optimizing the Vane-Endwall Junction in a Turbine Vane Passage." ASME Paper GT2003-38939, Atlanta 2003.

Ligrani, P. M., B. A. Singer, L. R. Baun. "Miniature Five-hole Pressure Probe for Measurement of Three Mean Velocity Components in Low-Speed Flows." J. Phys. E: Sci. Instrum. 22 (1989): 868-876.

Ligrani, P. M., B. A. Singer, L. R. Baun. "Spatial Resolution and Downwash Velocity Corrections for Multiple-Hole Pressure Probes in Complex Flows." Exp. Fluids 7 (1989): 424-426.

Oke, Rohit A., Terrence W. Simon. "Film Cooling Experiments with Flow Introduced Upstream of a First Stage Nozzle Guide Vane Through Slots of Various Geometries." ASME Paper GT-2002-30169, Amsterdam 2002.

Oke, Rohit A., Terrence W. Simon, Steven W. Burd, Rickard Vahlberg. "Measurements in a Turbine Cascade Over a Contoured Endwall: Discrete Hole Injection of Bleed Flow." ASME Paper 2000-GT-214, Munich 2000.

Oke, Rohit, Terry Simon, Tom Shih, Bin Zhu, Yu Liang Lin, Minking Chyu. "Measurements Over a Film-Cooled, Contoured Endwall with Various Coolant Injection Rates." ASME Paper 2001-GT-0140, New Orleans 2001.

Pasinato, Hugo D., Zan Liu, Ramendra P. Roy, W. Jeffrey Howe, Kyle D. Squires. "Prediction and Measurement of the Flow and Heat Transfer Along the Endwall and Within an Inlet Vane Passage." ASME Paper GT-2002-30189, Amsterdam 2002.

Rose, M. G. “Non-Axisymmetric Endwall Profiling in the HP NGV’s of an Axial Flow Gas Turbine.” ASME Paper 94-GT-249, 1994.

Saucer, H., R. Muller, K. Vogeler. “Reduction of Secondary Flow Losses in Turbine Cascades by Leading Edge Modifications at the Endwall.” ASME Paper 2000-GT-0473, Munich 2000.

Shih, T. I-P., Y. –L. Lin. “Controlling Secondary-Flow Structure by Leading-Edge Airfoil Fillet and Inlet Swirl to Reduce Aerodynamic Loss and Surface Heat Transfer.” ASME Paper GT-2002-30529, Amsterdam 2002.

Shih, T. I-P., Y. –L. Lin, T. W. Simon. “Controll of Secondary Flows in a Turbine Nozzle Guide Vane by Endwall Contouring.” ASME Paper 2000-GT-0556, Munich 2000.

Sieverding, C. H. “Recent Progress in the Understanding of Basic Aspects of Secondary Flow in Turbine Blade Passage.” ASME Journal of Engineering for Gas Turbines and Power 107 (1985): 248-257.

Timko, L. P. “Energy Efficient Engine High Pressure Turbine Component Test Performance Report.” Contract Report for NASA, Report No. NASA CR-168289.

Wang, H. P., S. J. Olson, R. J. Goldstein, E. R. G. Eckert. “Flow Visualization in a Linear Turbine Cascade of High Performance Turbine Blades.” ASME Journal of Turbomachinery 119 (1997): 1-8.

Yan, J., D. G. Gregory-Smith, P. J. Walker. “Secondary Flow Reduction in A Nozzle Guide Vane Cascade by Non-Axisymmetric End-wall Profiling.” ASME Paper 99-GT-339, 1999.

Zess, G. A., K. A. Thole. “Computational Design and Experimental Evaluation of Using a Leading Edge Fillet on a Gas Turbine Vane.” ASME Paper 2001-GT-0404, New Orleans 2001.

Appendix A: Validyne Pressure Transducer Calibration

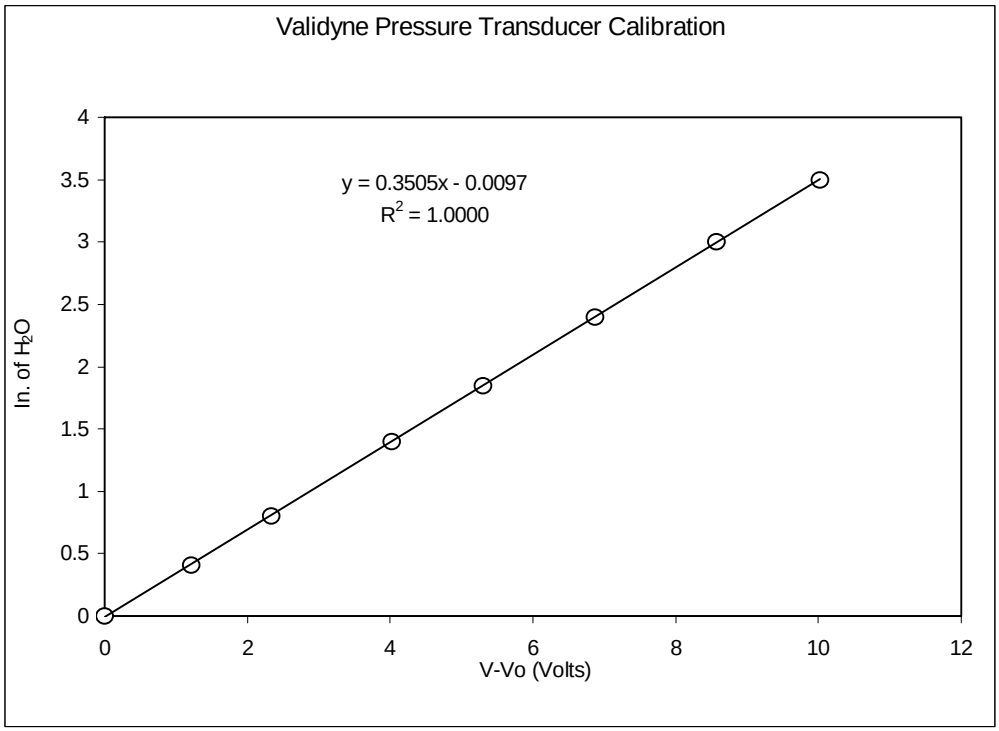

Appendix B: Hot Wire Calibration Curves

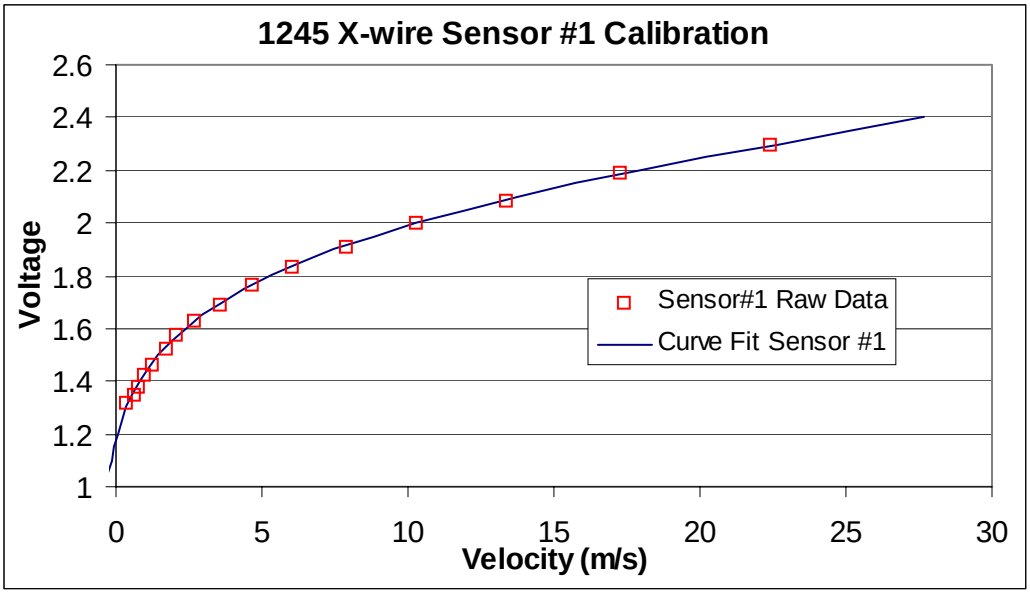

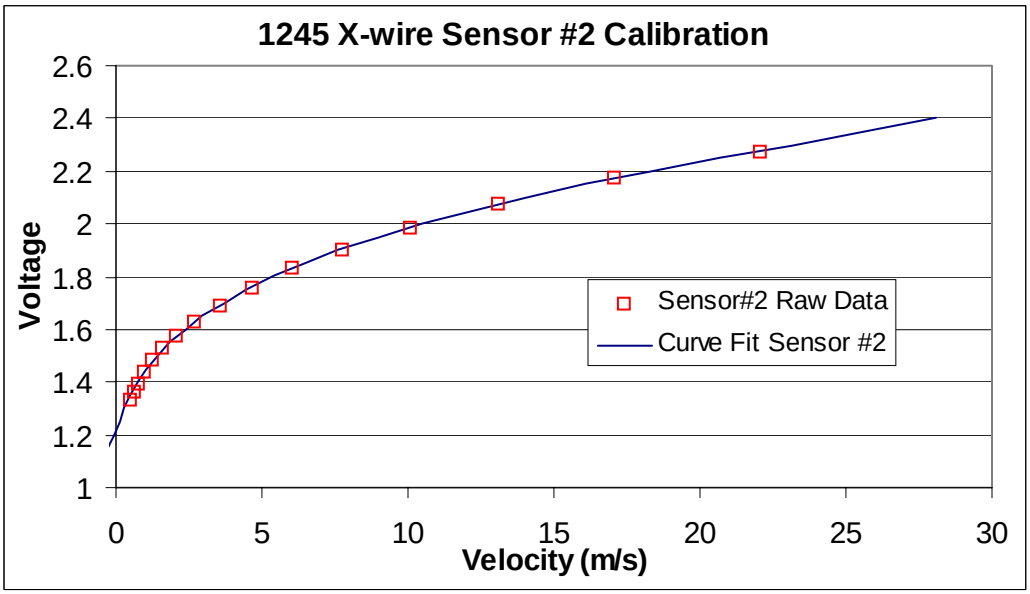

Appendix C: Five-Hole Calibration Curves

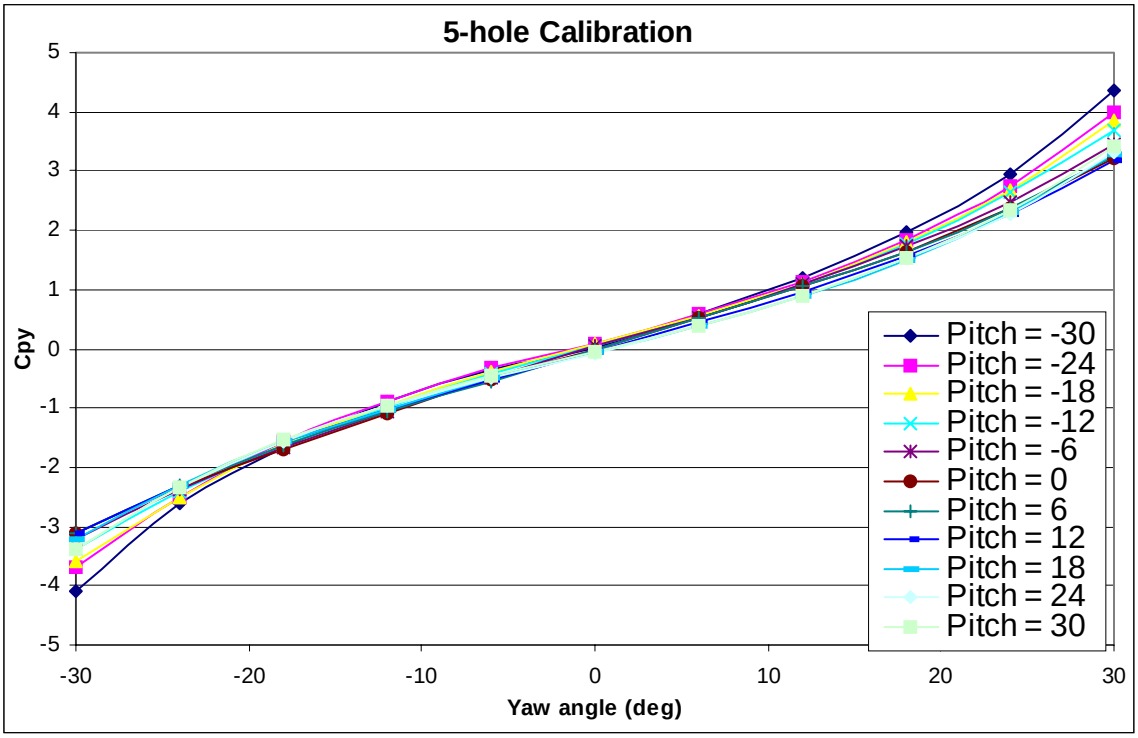

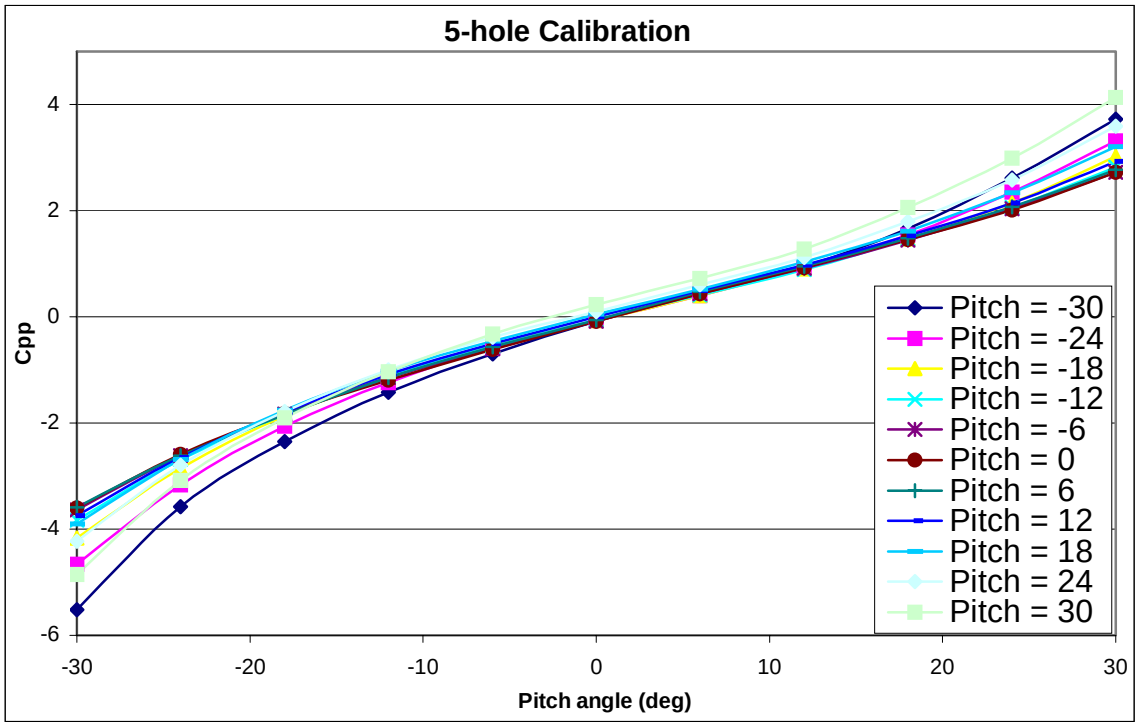

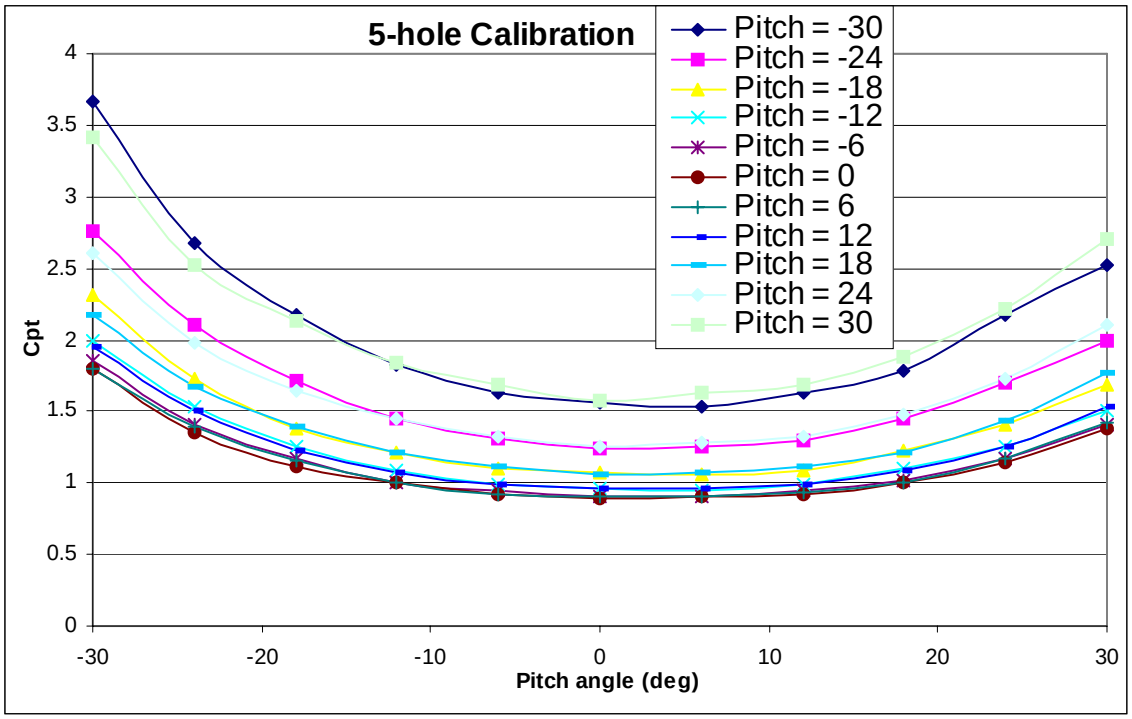
5-hole Calibration
Pitch = -30
Pitch = -24
Pitch = -18
Pitch = -12
Pitch = -6
Pitch = 0
Pitch = 6
Pitch = 12
Pitch = 18
Pitch = 24
Pitch = 30
Cpt
Pitch angle (deg)
4
3.5
3
2.5
2
1.5
1
0.5
0
-30
-20
-10
0
10
20
30

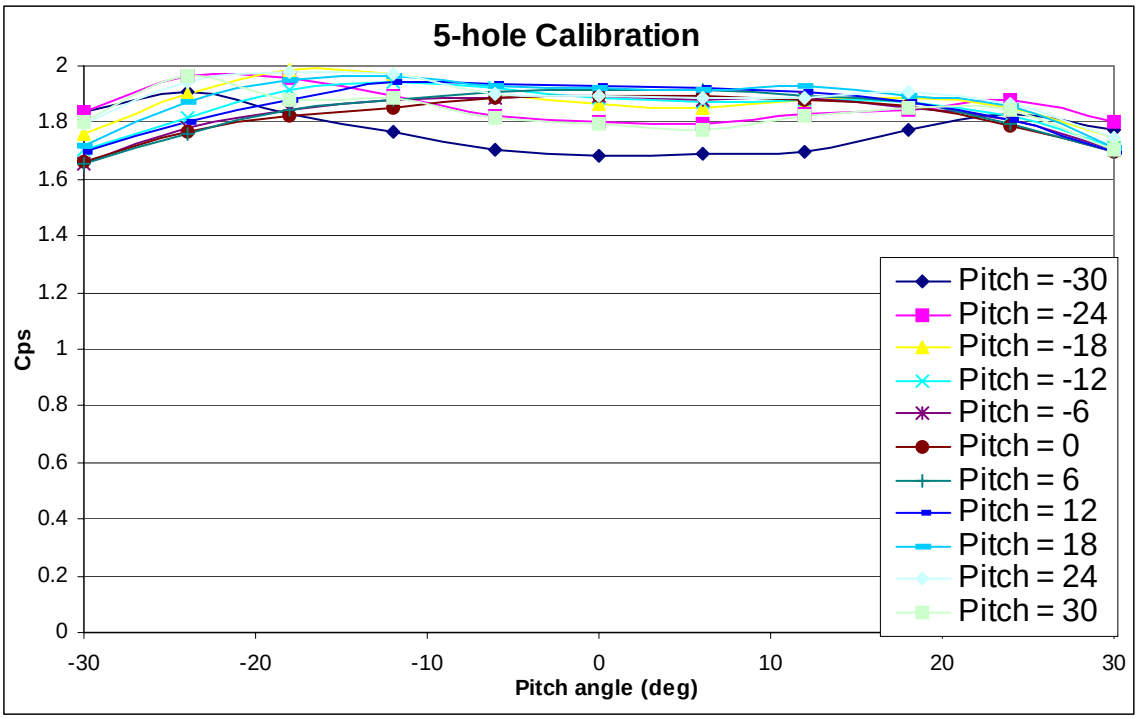
5-hole Calibration
Pitch = -30
Pitch = -24
Pitch = -18
Pitch = -12
Pitch = -6
Pitch = 0
Pitch = 6
Pitch = 12
Pitch = 18
Pitch = 24
Pitch = 30
Cps
Pitch angle (deg)
2
1.8
1.6
1.4
1.2
1
0.8
0.6
0.4
0.2
0
-30
-20
-10
0
10
20
30

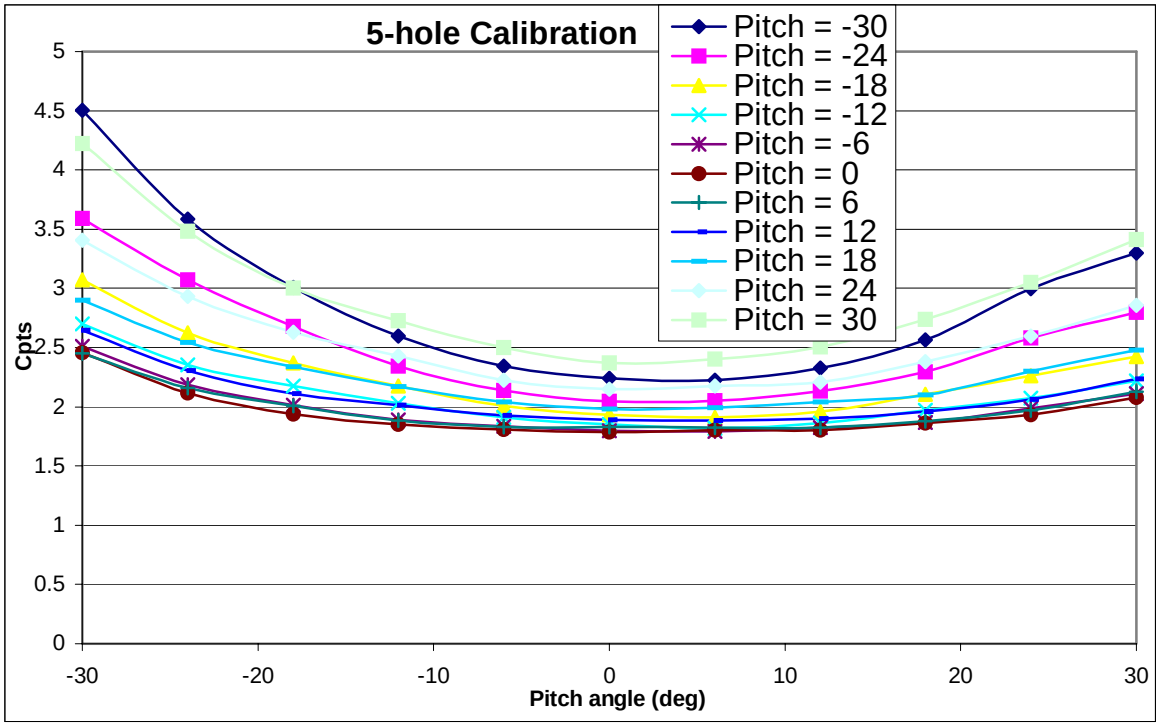
5-hole Calibration
Pitch = -30
Pitch = -24
Pitch = -18
Pitch = -12
Pitch = -6
Pitch = 0
Pitch = 6
Pitch = 12
Pitch = 18
Pitch = 24
Pitch = 30
Cpts
5
4.5
4
3.5
3
2.5
2
1.5
1
0.5
0
-30
-20
-10
0
10
20
30
Pitch angle (deg)

Appendix D: Thermocouple Probe Calibration Curve

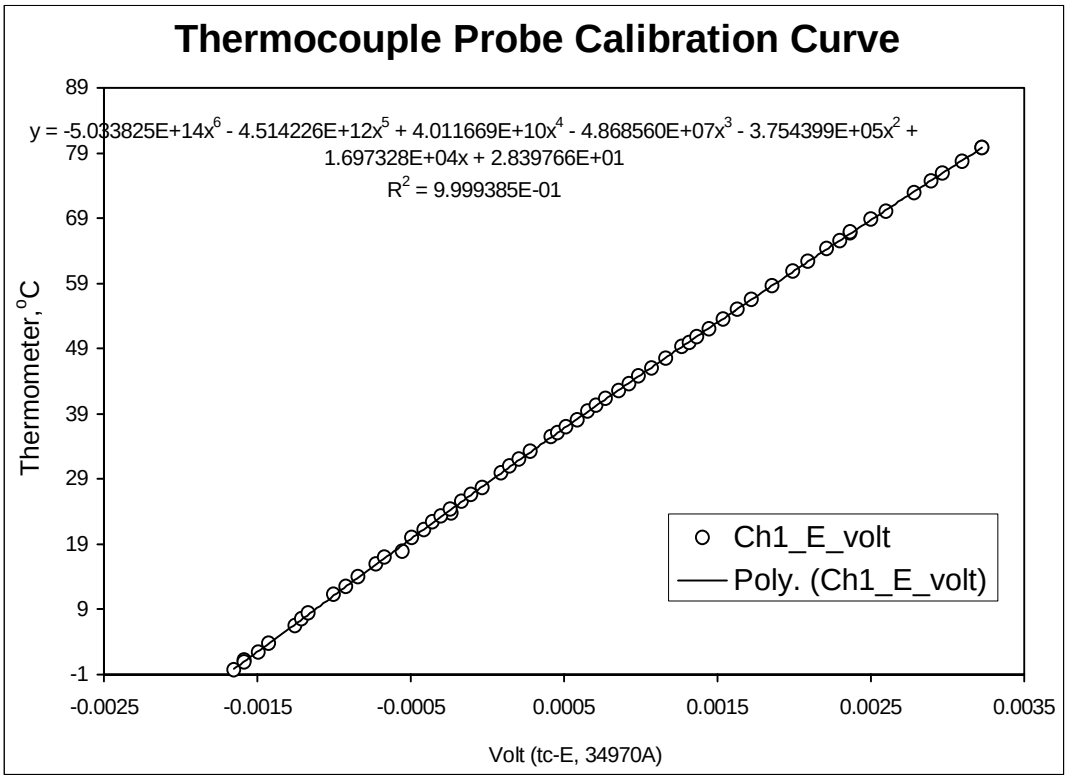

Vita

Ross James Gustafson was born in the city of New Iberia in the state of Louisiana. His parents are James Wesley Gustafson and Anna Ma Gustafson. Ryan Chaney Gustafson is his older brother. He graduated from New Iberia Senior High School in spring of 1998 with honors in the top 3% of his class. Following, he attended Louisiana State University and obtained his bachelor's degree in mechanical engineering in the fall of 2002 with a GPA of 3.5. While in college he was a member of the Delta Sigma Phi fraternity and held several officer positions. He next attended graduate school at Louisiana State University pursuing his master's degree in mechanical engineering under a graduate assistantship provided by Dr. Sumanta Acharya. While attending graduate school he was awarded the University Turbine Systems Research intern Fellowship during the summer of 2003. The internship lasted for three months and was with General Electric Power Systems in Greenville, South Carolina, where gas turbine power plants are designed and manufactured. He obtained his Master of Science in Mechanical Engineering degree from Louisiana State University in May of 2005.